Masters Theses

Graduate School

8-2018

SAND DEPOSIT MAPPING AND AEOLIAN MORPHOLOGIES AS CLUES FOR IDENTIFYING ORIGINS OF DARK SAND IN AEOLIS DORSA, MARS

Ariana Sterling Boyd
University of Tennessee, aboyd21@vols.utk.edu

To the Graduate Council:

I am submitting herewith a thesis written by Ariana Sterling Boyd entitled "SAND DEPOSIT MAPPING AND AEOLIAN MORPHOLOGIES AS CLUES FOR IDENTIFYING ORIGINS OF DARK SAND IN AEOLIS DORSA, MARS." I have examined the final electronic copy of this thesis for form and content and recommend that it be accepted in partial fulfillment of the requirements for the degree of Master of Science, with a major in Geology.

<div align="right">Devon M. Burr, Major Professor</div>

We have read this thesis and recommend its acceptance:

Christopher M. Fedo, Liem Thanh Tran

<div align="right">Accepted for the Council:

<u>Dixie L. Thompson</u>

Vice Provost and Dean of the Graduate School</div>

(Original signatures are on file with official student records.)

SAND DEPOSIT MAPPING AND AEOLIAN MORPHOLOGIES AS CLUES FOR IDENTIFYING ORIGINS OF DARK SAND IN AEOLIS DORSA, MARS

A Thesis presented for the
Master of Science
Degree
The University of Tennessee, Knoxville

Ariana Sterling Boyd
August 2018

DEDICATION

To my parents and my role models, Wes and Theonia.

To my siblings, Naomi, Anaïs, and Emerson.

To my grandmother, Frida.

ACKNOWLEDGMENTS

ABSTRACT

Dark sand deposits occur at all latitudes on the Martian surface. Sand sources in some regions have been inferred via paleo-wind indicator analyses, sand and source mineralogy comparisons, and climate modeling. However, all known sources are sedimentary, leaving outstanding the question of primary igneous origin(s) of these dark sand deposits. One hypothesis addressing this question is that volcaniclastic deposits are a primary origin of Martian sand. Terrestrial analogs of volcaniclastic units sourcing sand support this hypothesis. However, sand generation has yet to be observed or inferred from any such Martian deposit. This thesis tests this hypothesis via a case study in Aeolis Dorsa, Mars, a locality where sand overlies bedrock consisting of a hypothesized volcaniclastic deposit, the Medusae Fossae Formation (MFF). In addition to the MFF, additional potential external sand sources exist: Elysium Mons, the Cerberus Plains lavas, and the Southern Highlands.

To identify likely sand source(s) in Aeolis Dorsa, sand deposits were mapped to address geospatial sand distribution, scour mark orientations were mapped and analyzed to reveal dominant paleo-wind directions, and instances of apparent erosion of bedrock to dark sediment were recorded. Hierarchical clustering analysis of sand distribution revealed preferential sand deposition on the peripheries of the MFF and in the southern depression (where bedrock may be remnant southern highlands material). Hierarchical cluster analysis of scour mark distribution revealed spatial groups of scour marks with consistent paleo-wind directions within groups. Such paleo-wind directions provide no evidence for long-distance sand transport from potential external source regions, but instead provide support for paleo-winds controlled by local topography. Apparent erosion of bedrock to dark sediments occurs in both the MFF (in ~20 localities) and in the southern depression (in over 100 localities), suggesting that both the MFF and bedrock in the southern depression have the potential to generate dark sand. The implication that the MFF has the potential to produce dark sand raises two important possibilities: first, that elsewhere along

the Martian equator the MFF may have produced dark sand, and second, that other friable layered

deposits (of which the MFF is one) may also serve as sources of Martian sand.

TABLE OF CONTENTS

LIST OF TABLES

LIST OF FIGURES

1. INTRODUCTION

The geologic origin and temporal persistence of sand on Mars remains a salient question in Martian geology. On this dry planet, multiple ongoing landscape modification agents continue to shape Mars' surface (e.g., Hansen et al., 2010; McEwen et al., 2010). One of these agents is aeolian activity (e.g., Bridges et al., 2007, 2012). Sand covers less than 0.01% of the Martian surface (e.g., Hayward et al., 2007), yet sand deposits occur at all latitudes on the Martian globe (Hayward et al., 2007, 2014). Present-day sand movement is a wind-driven process, and understanding the origins and movement of sand on the Martian surface is fundamental to our knowledge and understanding the current Martian sediment cycle.

Sand sources are difficult to definitively constrain in cases where no obvious local source (defined by Fenton et al., 2005, as within one sand deposit width of the deposit) exists, but with a cache of clues that address sand and source characteristics, sand sources may become illuminated. These clues include sand deposit distribution, aeolian morphologies that serve as paleo-wind indicators, mineralogy of sand and of possible sources, and climate modeling. Indeed, these clues provided the necessary information to constrain sand sources in a number of localities on Mars (see Section 2.4). However, because Martian sand commonly occurs without an apparent local source, the sources of most Martian sand deposits remain unknown. Each identification of a Martian sand source aids in illuminating Martian sediment pathways and transport characteristics. By connecting Martian sand deposits to their source(s), patterns of sand origination and movement on Mars will become clearer. Determining sediment pathways and sand sources helps provide small pieces of the Martian sediment cycle puzzle.

Also requiring consideration are the primary igneous units that provide the original material of (overwhelmingly likely sedimentary) rocks from which Martian sand is generated. Martian sand, like terrestrial sand, originates from rocks that, in some point prior to sediment liberation (e.g., recycled or not), were igneous in origin (e.g., Edgett and Lancaster, 1993; Burr et al., 2012).

Volcaniclastic units—friable deposits at the surface—may be one of these direct sources of sand, but this hypothesis is not yet well-tested on Mars.

One method by which the possibility of volcaniclastic deposits generating Martian sand can be addressed is via case studies in localities where sand occurs overlying or adjacent to volcaniclastic deposits. In these localities, observational methods, such as those previously mentioned, can be employed to address the likelihood of such a deposit generating overlying sand. This work addresses the volcaniclastic-origin hypothesis by testing multiple working hypotheses, including local (*in situ*) and regional (external) possible sources, for sand sources in the Aeolis Dorsa region of Mars (Fig. 1.1), a locality where dark sand overlies a hypothesized volcaniclastic deposit (Mandt et al. 2008, 2009).

This study tests multiple working hypotheses for sand sources using (a) the geospatial distribution of sand, (b) wind emplacement directions inferred from sand deposit morphologies, and (c) observations of potential sand sources via orbital images. In this paper, I first cover important aspects of Martian sand deposits, along with previous studies that have identified sand sources. I describe characteristics of the Medusae Fossae Formation, the hypothesized volcaniclastic unit in the Aeolis Dorsa region, and the reasoning for its hypothesized volcaniclastic origin. I also describe the geography surrounding Aeolis Dorsa, which provides the basis for the working hypotheses I then explain. Next, I summarize the methods and datasets used to test these working hypotheses. I then discuss the results of these methods, and the extent to which working hypotheses are supported, tying my results to implications for sand movement and deposition on the Martian surface.

2. BACKGROUND

2.1. Sand generation and transport mechanisms on Mars

A myriad of processes, including impact cratering, fluvial and aeolian erosion and transport, and volcanism, have contributed to the generation and transport of sand on Mars (e.g., Hartmann and Neukum, 2001; McGlynn et al., 2011, 2012). Sediments on Mars are commonly sorted and/or weathered such that their sources are difficult to discern texturally (e.g., McGlynn et al., 2011). Early in Mars' history, bolide impacts or 'impact gardening' played an appreciable role in sediment generation (e.g., Hartmann and Neukum, 2001; Knauth et al., 2005; McGlynn et al., 2011), and continue to play a minor role in surface gardening at present, although reworking of sediment produced by bolide impacts may still occur today.

Volcanoes generate sand via explosive eruptions, such as those from Arsia and Tharsis Montes (e.g., Edgett, 1997; Mouginis-Mark, 2002). Dark dunes occur at Arsia Mons and have been inferred to form from volcaniclastic deposits originating from Arsia Mons (Mouginis-Mark, 2002). Supporting evidence for explosive volcanism generating Martian sand exists in the Tharsis region, where dune fields occur for which the most likely source of sand is hypothesized volcaniclastic material (Edgett, 1997).

Impact cratering generates large volumes of loose sediment on Mars (e.g., Hartmann and Neukum, 2001; McGlynn et al., 2011, 2012) that, over time, are sorted and comminuted via aeolian, fluvial, and/or secondary impact processes (e.g., McGlynn et al., 2011). Basaltic soil in Gusev crater, for example, occurs as distinct grain-size and mineralogical populations representative of selective sorting and variation in transport modes (McGlynn et al., 2011, 2012).

Sand-sized grains are most easily entrained by the wind (e.g., Greeley and Iversen, 1985). Due to Mars' thin atmosphere, threshold wind speed—the lowest wind speed sufficient to entrain sediment of any size—is higher for grains of any size than are threshold speeds on Earth (e.g., Greeley and Iversen, 1985). Once entrained at such high wind speeds, sand grains impact the Martian surface with intensity expected to cause rapid comminution of grains to smaller particle

sizes (e.g., Sagan, 1973; Greeley and Iversen, 1985; Greeley and Kraft, 2001). Thus, aeolian physics predicts relatively short transport distances for Martian sand before sand is no longer sand-sized. Known sand sources, identified to date, lie near to sand deposits, providing evidence only for relatively short transport pathways (e.g., Fishbaugh et al., 2007; Tirsch et al., 2011; Chojnacki et al., 2014c). Where longer transport pathways may exist on Mars, like on Earth, such pathways are difficult to identify if that pathway is inactive and/or obscured by dust cover or other disruption of the pathway (e.g., Sullivan et al., 2005).

2.2. Sand deposit localities and sources on Mars

Active (loose) sand occurs in varying amounts at all latitudes on Mars (Hayward et al., 2007, 2014), but occurs in the most concentrated amounts in: (1) the mid-latitude regions; (2) in dune-rich sand seas in polar ergs adjacent to the north polar layered deposits (NPLDs); and (3) in the equatorial region of Mars (Hayward et al., 2007, 2014). Sand sources in these three locations have been positively identified via orbital visible-wavelength images, spectroscopic data, and infrared imagery. The most likely sources of sand in these locations are sedimentary units, meaning that those sediment sources are secondary re-worked material, rather than a primary igneous source of sediment, although in Valles Marineris, the wall rock is inferred to be a primary sand source (e.g., Chojnacki et al., 2014c).

Many of the topographic lows in which dark sand concentrates on Mars are crater basins (Bridges et al., 2012). The walls of craters have been hypothesized to produce the sand found in those crater basins (Edgett, 2002; Fenton, 2005; Fenton, 2008). This hypothesis is supported by images showing apparent sediment generation in dark crater wall units and by compositional similarity between the crater walls and the intracrater dunes (Tirsch et al. 2011), based on analysis of data from the Observatoire pour le Mineralogie, l'Eau, les Glaves et l'Activité (OMEGA; Bibring et al., 2004) and Compact Reconnaissance Imaging Spectrometer for Mars (CRISM; Murchie et al., 2004) imaging spectrometers.

Vast gypsum-rich dune fields of the Olympia Undae sand sea near Mars' north poles—to date the only known sulfate-rich dunes on Mars (Fishbaugh et al., 2007)—are concentrated in the north polar region of Mars. First identified as gypsum-rich by Langevin et al. (2005), these sand seas were hypothesized to be exhumed magmatism-related hydrothermal gypsum deposits within the north polar layered deposits (PLDs) (e.g., Tanaka, 2006; Horgan and Bell, 2012). Geospatial constraints of gypsum-rich units in this region, determined via OMEGA data, identified gypsum only in the sand sea itself and in isolated dune patches, not in any other part of the region (including PLD layers). The confinement of gypsum to the Olympia Undae sand sea and isolated nearby dunes led Fishbaugh et al. (2007) to conclude the most likely source of gypsum in these deposits as water percolating through the basal unit of the north polar layered deposits and forming gypsum in pore spaces of the calcium-rich sand (Fishbaugh et al., 2007).

Sources of sand dunes in Valles Marineris, Mars, were investigated using visible-wavelength images, digital elevation models (DEMs), and thermal inertia data of dunes and the surrounding surface. Multiple working hypotheses were tested, and orbital images indicated that the most likely source(s) were valley walls, which recorded evidence of mass-wasting in the form of boulder tracks and boulders on the floor of the rift, and the interior layered deposits (Chojnacki et al., 2014c). These three regions—impact basins in the mid-latitudes, the north polar erg, and Valles Marineris—constitute all known sources of Martian sand. Although sand sources have been inferred for these three regions, sources for the other sand deposits among the global distribution of sand on Mars have not been inferred. Although sand sources in these cases identify a single primary source of sand for each dune field, sand sources are likely commonly cosmopolitan, an overwhelmingly common feature of terrestrial dune fields (e.g., Kocurek and Lancaster, 1999).

In addition to sand sources mentioned here, volcanic units may be additional sources of Martian sand. The commonality of volcanism on Mars led to the hypothesis over sixty years ago that non-reworked volcanic materials could be a primary source of Martian sand (McLaughlin, 1954, 1956a, 1956b; Edgett and Lancaster, 1993). More recent research has led to the hypothesis

that widespread friable layered deposits (FLDs; Kerber et al., 2011, 2012), some of which are proposed to be volcaniclastic in origin (see Section 2.3), may serve as one of a number of sources of globally distributed sand.

2.3. The Medusae Fossae Formation

The Medusae Fossae Formation (MFF) is an extensive, layered deposit that extends along the Martian equator from approximately 130° to 240° E, and from 15° S to 15° N (Fig. 2.1; Scott and Tanaka, 1986; Greeley and Guest, 1987; Zimbelman et al., 1996; Bradley et al., 2002). The MFF consists of discontinuous layers (Sakimoto et al., 1999) of friable material (Scott and Tanaka, 1982). The MFF outcrops as five lobes running along the Martian equator (Figure 2.1). The oldest, and stratigraphically lowest, layers of the MFF comprise its westernmost two lobes, whereas the youngest, and stratigraphically highest, layers of the MFF are on the easternmost extent. In addition to decreasing in age, from west to east the MFF thickens (Edgett et al., 1997; Bradley et al., 2002). Whereas the upper MFF can reach 800 m in thickness (Bradley et al., 2000, 2002), in some localities the western MFF is so thin that basement rocks appear to be partially exposed (Bradley et al., 2000, 2002). At footprint scales of 100-200 m, the average surface roughness of the western MFF is 2-3 times the surface roughness of the eastern MFF (Sakimoto et al., 1999). The MFF is characterized by pervasive fields of yardangs (wind-scoured hills; Ward, 1979) indicative of easily friable material (Fig. 2.2; Kerber and Head, 2010; Kerber et al., 2012).

The impressive extent and variable surficial properties across the MFF contribute to the continued uncertainty of its geologic history and origin. The MFF has been proposed to be: 1) a polar layered terrain due to some similarities (at the global scale) with rocks in Mars' polar regions (e.g., Schultz and Lutz, 1988); 2) the accumulation of 'rafted' pumice on the banks of an ancient northern ocean (e.g., Mouginis-Mark, 1993); 3) a carbonate platform (e.g. Parker, 1991); and 4) volcaniclastic in origin, as either an ash-fall tuff (e.g., Hynek et al., 2003) or an ignimbrite (ash flow) deposit (e.g., Mandt et al. 2008, 2009). Thus far, four lines of evidence provide support for the hypothesis that the MFF is indeed a series of volcaniclastic deposits. First, layer thickness in

the MFF varies substantially both between different layers and, in some cases, within the same layer (Bradley et al., 2002, and references therein). Second, layers comprising the MFF appear to blanket regional topography, rather than showing preferential deposition in topographic lows (Mandt et al., 2008). Third, yardang directions and morphologies vary in close geographic proximity to one another, indicating possible small-scale variable induration of the MFF (Fig. 2.3; Bradley et al., 2002; de Silva et al., 2010). Fourth, density estimates and the dielectric constant of the MFF both suggest a highly porous unit absent of ice, consistent with an explosive volcanic unit (Ohja and Karunstillake, 2017; Ohja et al., 2017). The friable nature of the MFF, along with support for its origin as a volcaniclastic deposit, raises the possibility of its potential as a source of nearby sand deposits (e.g., Kerber et al., 2010). Its potential as a source of Martian sand is highlighted in places where sand overlies the MFF, which would allow for *in situ* erosion of bedrock to sand without any requirement of sand transport (and thus potential comminution). One such location is the Aeolis Dorsa region of Mars, where dark sand overlies outcrops of the lower MFF.

2.4. Martian aeolian bedforms within the Aeolis Dorsa study area

Sand deposits occur on Mars with and without distinctive aeolian features like dunes or ripples (Fig. 2.4; Hayward et al., 2007). Sand deposits in Aeolis Dorsa occur either as elongate sediment deposits located within narrow bedrock troughs, or as sand sheets, defined as broad deposits with smooth surfaces, found on relatively flat or smooth terrain (Fig. 2.5; Table 1; e.g., McKee, 1979). Sand sheets may appear dark, if not dust-covered, or bright, in which cases light hues likely indicate a partial to complete dust cover (e.g., Fenton et al., 2003). Both dark and bright sand sheets are present in Aeolis Dorsa. Bright sand sheets can be identified as dust-covered sand if features indicative of sand, e.g., scour marks or dunes, are observed on the sheet.

Morphological features present in any given sand deposit depend on a) the abundance of sand and b) the wind directions that transported the sediment. Consequently, many aeolian features may be used as wind-direction indicators (e.g., McKee, 1979; Greeley and Iversen, 1985). In the

Aeolis Dorsa deposits, a small number of directional morphologies are present, including scour marks and various dune forms (Table 1).

2.4.1. Scour marks

Scour marks—also known as aeolian scours or current crescents (Peabody, 1947)—were first identified on Mars during the MER Spirit rover's travels in Gusev Crater (e.g., Bell et al., 2004; Thomson et al., 2007; Greeley at al., 2008). Scour marks in dark sand deposits on Mars were identified in orbital images by Bishop (2011) via High Resolution Imaging Science Experiment (HiRISE) camera images (McEwen et al., 2007). Scour marks are formed via wind flow around an obstacle, where enhanced flows are deflected down and around the obstacle on the upwind side (Fig. 2.6). The accelerated wind velocities entrain more sediment than average on the upwind side of the obstacle. This sediment entrainment and movement downwind effectively removes material in the area of accelerated flow, forming a crescentic negative-relief moat around the upwind side of that obstacle (Fig. 2.7; Greeley and Iversen, 1985; Bishop, 2011). For largely unidirectional flows, the resulting moat is a singular crescent. Reversing wind regimes produce pairs of crescents on opposite sides of obstacles whereas variable or multidirectional winds will produce moats around much, or all, of the sides of an obstacle (Allen, 1984). In Aeolis Dorsa, all three morphologies occur, although single crescentic scour marks are the most common morphology.

2.4.2. Common dune forms

The Martian surface showcases many dune forms (Fig. 2.4). Dunes present in Aeolis Dorsa include transverse, climbing, falling, and echo dunes (Table 1). Transverse dunes, straight or slightly sinuous ridges oriented normal to the average transport direction (Reffet et al., 2010), form in wind regimes with an abundant sand supply (McKee, 1979) or in bidirectional regimes with either small (~45 to 70°) or ~180° divergence angles (determined in flume experiments by Rubin and Ikeda, 1990). Climbing and falling dunes (e.g., Tsoar, 1983; Chojnacki et al., 2010) are dune forms located on slopes. Climbing dunes advance up slopes, whereas falling dunes advance

downslope. Climbing and falling dunes are commonly found in tandem, such as when sediment breaches a crest and transitions from a climbing to falling dune, or when falling dunes reach a topographic low and advance to adjacent slopes as climbing dunes (Tsoar, 2001). Echo dunes are dunes that are anchored to a surface and have slipfaces parallel with bedrock cliffs. Scour marks in sand commonly feature echo dunes directly upwind. Echo dunes and scour marks commonly occur in tandem as within the Aeolis Dorsa region.

2.5. The Aeolis Dorsa region, Mars

2.5.1. Aeolis Dorsa regional geology

Aeolis Dorsa (Fig. 1.1) is one of many regions on Mars that exhibits sand deposits without an obvious source. Aeolis Dorsa lies along the Martian equator just north of the highland-lowland boundary (HLB; Lenardic et al., 2004; Irwin and Watters, 2010) and south of Elysium Mons. Bedrock in Aeolis Dorsa consists predominantly of the MFF, which is exposed here as the twin plateaus Aeolis and Zephyria Plana (Fig. 1.1; Scott and Tanaka, 1986; Greeley and Guest, 1987). In between the two plana lies a lower-elevation region, hereafter referred to as the Aeolis-Zephyria Plana (AZP) medial basin (Fig. 1.1). The bedrock in the AZP medial basin consists of neither MFF nor southern highlands materials, but of hypothesized complex sedimentary deposits rife with inverted fluvial channels (e.g., Burr et al., 2009, 2010; Lefort et al., 2012; Williams et al., 2013; Jacobsen and Burr, 2017). Sand deposits overlie topographic lows within bedrock units throughout much of Aeolis Dorsa.

Sand deposits may have either low- or high- albedo signatures in the visible wavelength depending on the extent of dust cover (see Section 2.4; Mellon et al., 2000; Putzig and Mellon, 2007). However, sand on Mars is typically dark-toned (e.g., Bridges et al., 2007), and many sand deposits in Aeolis Dorsa share this characteristic. Sand deposits in Aeolis Dorsa are characterized by infrared signatures that are brighter than the surroundings in both the daytime and nighttime data (Burr et al., 2011).

2.5.2 Geologic context: ages and stratigraphic relationships

In Aeolis Dorsa, bedrock unit age is loosely constrained via crater counts and stratigraphic relationships. The southern highlands, confined to the southernmost portion of the map, date to the Noachian (Hartmann and Neukum, 2001, and references therein). In Aeolis Dorsa, however, southern highlands materials (Fig. 1.1) exhibit fretted valleys and polygonal high-standing blocks, features that have been inferred to be associated with the Noachian/Hesperian transition (e.g., Irwin and Watters, 2010). Thus, although the bedrock itself is Noachian, surface modification of the highlands in this area dates possibly as far back as the Noachian/Hesperian transition. In addition to these constraints on the southern highlands, the relative age of the MFF and of bedrock within the AZP medial basin is loosely constrained.

The AZP medial basin is composed of Noachian- to Hesperian-aged deposits of fluvial sedimentary origins (e.g., Kite et al., 2013; Jacobsen and Burr, 2016). Crater ejecta blankets surround some craters in Aeolis Dorsa (Fig. 1.1). The MFF, once thought to be Amazonian in age based on crater counts (Tanaka, 1986), is inferred to have formed during the mid-Hesperian to early Amazonian and subsequently extensively reworked (Kerber and Head, 2010; Zimbelman and Scheidt, 2012). The MFF ages stratigraphically, with younger layers superposed on older layers. Thus, lower-elevation layers of the MFF are inferred to be older than adjacent higher-elevation layers.

The MFF is known for pervasive, overlapping yardang fields (Fig. 2.2; e.g., Bradley et al., 2002; Mandt et al., 2009; Zimbelman and Griffin, 2010), and the MFF in Aeolis Dorsa is no exception. In Aeolis Dorsa, separate yardang fields (defined by parallel yardangs; see Fig. 2.8 for example) are separated by elevation (Fig. 2.8). Many yardang fields have either a broadly E-W orientation or a broadly N-S orientation (NW-SE in Fig. 2.8). The E-W-oriented yardangs occur at a slightly lower elevation than N-S-oriented yardang fields, suggesting that E-W yardangs are comprised of older rocks than those with a N-S orientation. In some localities, N-S-trending features cut E-W yardangs, providing additional support for the inference that N-S yardangs are younger than

their E-W-trending counterparts. By extension, N-S trending yardangs may represent a more recent wind regime than the winds that formed the E-W trending yardangs.

2.5.3. Potential sources of sand in Aeolis Dorsa

Multiple local and regional potential sources exist for sand in Aeolis Dorsa. Regional sources, defined by Fenton (2005) as removed by several times the sand deposit width from the deposit(s) in question, include any region around Aeolis Dorsa that is either known to produce sand-sized particles or has the potential to do so. Three such regions surround Aeolis Dorsa: the Elysium Mons edifice to the north, the Cerberus Plains lava flows to the northeast, and the southern highlands to the south (Fig. 2.9). These regions have the potential to generate sand-sized particles (Elysium Mons, Cerberus Plains lavas) or are known to produce or at least contain dark sand (the southern highlands).

Elysium Mons is a large volcanic edifice located ~1500 km north of Aeolis Dorsa. On Elysium Mons, variability in impact crater appearance and lobate flow features suggests the past presence of volatiles within the edifice (Mouginis-Mark et al., 1984). The inferred past volatile content suggests the potential for explosive volcanic activity from the edifice (Mouginis-Mark, 1985), which would deposit volcaniclastic materials on and around the edifice. Deposition could occur in a more widely dispersed fashion, given the suggestion by numerical modeling of eruptions on Mars as more explosive, with eruptive material more widely dispersed, than eruptions on Earth (Wilson and Head, 1994; Fagents and Wilson, 1996). Moreover, the presence of dunes inferred to form from volcaniclastic deposits of other volcanic edifices like Arsia Mons (Mouginis-Mark, 2002) and Tharsis Montes (Edgett, 1997) suggests the possibility of volcaniclastic deposits on Elysium Mons as a source of dark sand.

The Cerberus Plains consist of an extensive series of lava flows northeast of Aeolis Dorsa (e.g., Plescia, 1990) that have produced an estimated volume of over 130,000 km^2 of lavas with estimated episodic activity as recently as ~2 Ma (Vaucher et al., 2009). These vast mafic to possibly ultramafic (e.g., Jaeger et al., 2010) lavas record evidence of erosion in the form of loose

boulders (Roberts et al., 2012) and dark sand in craters and/or vents, e.g., near the Cerberus Fossae (formerly Rupes; Edgett and Rice, 1995) fractures. Fissures occur throughout the Cerberus lavas, in certain localities co-located with loose sediment (e.g., Roberts et al., 2007). Impact cratering and "Marsquakes" (Roberts et al., 2012) provide potential mechanisms for the recent, and potentially ongoing, generation of loose sediment observed on the Cerberus Plains.

The ancient Martian southern highlands are heavily cratered plains on which dark sand occurs, both in intracrater plains (Hayward et al., 2007) and in crater basins (e.g., Tirsch et al., 2011). This dark sand is basaltic in composition and contains olivine (Tirsch et al., 2011), indicating little chemical weathering. The source of sand in southern highlands crater basins is interpreted as dark layers in the crater walls themselves (Tirsch et al., 2011), but the source of the intracrater plains sand is unknown. Given the improbability of sand moving out of crater basins and onto the plains (summarized in Bridges et al., 2012), sand in crater basins is an unlikely source for sand in Aeolis Dorsa—although sand moving over the plains could be such a source. Sand on the southern highlands intracrater plains could be transported northward to Aeolis Dorsa, where sand would likely accumulate in the southern depression (Fig. 1.1).

In the Aeolis Dorsa study area, possible local sources include blocks of bedrock in the southern depression and the underlying MFF, which here comprises Aeolis and Zephyria Plana (Fig. 1.1). These bedrock blocks commonly either are thickly layered or massive, similar to bedrock of the southern highlands south of Aeolis Dorsa. This morphology differs from typical MFF morphology (see Section 2.3) and indicates that bedrock in the southern depression is not MFF material. Both the blocks and the southern highlands proper are characterized by thick crude layering (Fig. 2.10). Thus, bedrock blocks in the southern depression may consist of southern highlands remnants.

The geographic region from where sand is sourced is a partial answer to the history of a sand deposit. The rest of the answer lies in the primary igneous unit from which sediment was generated. Three of the potential sources outlined above would indicate primary geologic origins of sand in Aeolis Dorsa: volcanic material from Elysium Mons, the Cerberus plains, or the

underlying MFF. Materials from the ancient southern highlands may provide a source for sand in

Aeolis Dorsa, but because the southern highlands materials may be sedimentary in origin (e.g.,

Tirsch et al., 2011), this region cannot provide a certain primary geologic origin of sand in Aeolis

Dorsa.

3. HYPOTHESES

This study addresses the likelihood of multiple potential regions as sources of sand in Aeolis Dorsa via inferring emplacement wind directions of sand in Aeolis Dorsa, determining the geospatial distribution of sand in the region, and identifying whether any bedrock is eroding, *in situ*, to sand-size particles. The hypotheses for this study are framed via their location with respect to Aeolis Dorsa. Potential external sediment sources lie to the south, north, and east of Aeolis Dorsa. Local sources include bedrock units underlying sand deposits within Aeolis Dorsa. Evidence in support of a local source would include erosion of dark bedrock adjacent to dark sand, and, ideally, direct pathways (i.e., talus slopes) between eroding bedrock and sand deposits. Support for regional sediment sources would include sand distributions consistent with transport from that region (outlined in Fig. 3.1), a potential pathway for sand transport from that region, and no indicator of a more dominant or probable local source. In addition to distinguishing geographic sources, these working hypotheses also, in some cases, provide distinct geologic origins (see Section 2.5.2).

Working hypotheses for Aeolis Dorsa sand sources include:

1. Elysium Mons (Fig. 3.1): The Elysium Mons edifice serves as a potential source of sand in Aeolis Dorsa via: 1) erosion of Elysium Mons lavas to loose sediment that was then transported to Aeolis Dorsa; and/or 2) explosive volcanism from Elyisum Mons and subsequent deposition of volcaniclastic sediment on the Elysium Mons edifice that was subsequently transported to the Aeolis Dorsa region. Transport southward and downslope to Aeolis Dorsa could be facilitated by katabatic winds. Katabatic winds on Mars are inferred to be very strong due to the relative contribution of radiative heat transfer along with very cold nighttime temperatures (Spiga, 2011). Thus, strong katabatic winds could serve as highly effective sediment transport mechanism for sediment from Elysium Mons to Aeolis Dorsa. The low-elevation AZP medial basin (Fig. 1.1) would be the probable end location for such sediment, as winds would funnel sediment into this basin, leaving sand

deposits concentrated in this area (blue shaded area in Fig. 3.1). Such transport would result in the formation of aeolian morphologies indicative of southward wind transport directions (arrows showing wind direction in Fig. 3.1), e.g., barchan dunes with south-pointing horns. Elysium Mons materials, which are largely volcanic in origin mixed with some portion of atmospheric dust, would constitute a primary igneous source of Martian sand. For this hypothesis, the following sequence of events must have occurred: explosive volcanism and/or liberation of sediment on Elysium Mons, followed by transport and subsequent sediment deposition in Aeolis Dorsa.

2. Cerberus Plains lavas (Fig. 3.2): The Cerberus Plains, located to the north and east of Aeolis Dorsa, consist of extensive lava flows (Kesthelyi et al., 2004 and references therein) where recent, and potentially ongoing, liberation of sediment occurs (see Section 2.5.2). The potential for erosion of the plains to sand-size particles via "Marsquakes" (Roberts et al., 2012) or impact cratering (Kesthelyi et al., 2000, 2004) offers a potential extensive source region for sand in Aeolis Dorsa. Sediment would be transported southwest from the Cerberus lavas, likely concentrating on the northeast side of Zephyria Planum, a topographic transport obstacle ('barriers' in Fig. 3.2). Aeolian features indicating northeasterly transport winds would provide additional support for this hypothesis (Fig. 3.2). Sand sourced from eroded Cerberus Plains lavas would provide a primary igneous origin. For this hypothesis, the following sequence of events must have occurred: Liberation of sediment from lava plains following Cerberus Plains volcanism, followed by transport and comminution of sediments from the Cerberus Plains to Aeolis Dorsa, and final sediment deposition on the northeast side of Zephyria Planum, with likely in situ sediment reworking.

3. Southern highlands (Fig. 3.3): Dark-toned material is present in multiple localities in the southern highlands (e.g., Fenton et al., 2003; Christensen et al., 2000), and dark sand occurs on the southern highlands plains (Fenton et al., 2003; Hayward et al., 2007; Tirsch

et al., 2011) to the south of Aeolis Dorsa. This hypothesis posits that sand from the southern highlands plains is transported downslope, across the highland-lowland boundary (HLB) to the lower-elevation Aeolis Dorsa region. The southern depression (Fig. 1.1) sits ~500 m below the elevation of the medial basin, making it a likely sand trap, especially for sand traveling across the HLB. Thus, a higher concentration of sand deposits in the southern depression (shading in Fig. 3.3) would support the southern highlands as a source for sand in Aeolis Dorsa. Aeolian features indicative of northward emplacement wind directions (arrows in Fig. 3.3) would also support this hypothesis, although enhanced vorticity within the depression might result in other wind directions. For this hypothesis, the following sequence of events must have occurred: Generation of loose sediment on the southern highlands likely by impact cratering, followed by aeolian transport of sediment northward, and down- elevation, to Aeolis Dorsa, then final deposition of sediment in southern Aeolis Dorsa, either within or at similar latitudes to the southern depression (Fig. 1.1).

4. *In situ* weathering of the MFF (Fig. 3.4): In this scenario, aeolian abrasion of friable MFF bedrock material in Aeolis Dorsa (Aeolis and Zephyria Plana) physically erodes the bedrock to loose sediment that includes sand-sized particles. This sediment is then transported downslope to adjacent topographic lows. The dust-sized particles are liberated as abrasion occurs, while sand-sized particles are subsequently moved locally via saltation, tending to concentrate in topographic lows. The most direct support for *in situ* production of sand in Aeolis Dorsa would be observations of bedrock eroding to dark sediment directly adjacent to sand deposits. Observations that would indirectly support this hypothesis include (1) concentrations of sand on or directly adjacent to the two plana (shading in Fig. 3.4), and (2) wind-direction indicators that support topographically controlled wind regimes rather than favoring a regional external source (arrows in Fig. 3.4). A finding that the MFF is the source of sand in Aeolis Dorsa would provide a likely

primary igneous origin for Martian sand. For this hypothesis, the following sequence of events must have occurred: Deposition of the western MFF (mid- to late- Hesperian to early Amazonian), followed by later liberation of sediment, likely via aeolian abrasion of friable MFF units. Liberated dust-sized sediments would be deflated and removed in suspension, while sand-sized sediment would likely concentrate in topographic lows of inter-yardang troughs.

4. DATA AND METHODS

4.1. Data

All mapping and scour-mark annotation was conducted on a base map of visible-wavelength images from the Mars Reconnaissance Orbiter (MRO) Context Camera (CTX; Malin et al., 2007), with an average image resolution of ~6 meters per pixel. In addition to the ArcMap CTX base map, the High-Resolution Imaging Science Experiment (HiRISE; McEwen et al., 2007) images provided high-resolution images for improved discernment of geologic relationships and dune morphologies. The resolution of 0.25 m/pixel for HiRISE images allowed analysis of individual feature morphologies in high dark-bedform-density regions. The CTX-mosaic global map on Google Earth (for which some CTX images of the study area are different images than those comprising the ArcMap CTX base map mosaic) was used to supplement the ArcMap CTX base map. In Google Earth, the CTX images was used with some caution because CTX images comprising the Google Earth CTX global map are mosaicked to equalize apparent brightness, resulting in contrast loss for some images. This contrast loss results in potential lightening, and subsequently missing, of dark sand.

Mapping of sand deposits was conducted at a ~1: 100,000 scale, whereas scour mark annotation was conducted at 1: 24,000. This smaller scale is appropriate for annotating scour marks in sand deposits, because sand deposits cover a relatively small overall area of the base map. Sand deposits were mapped as polygons (see Section 4.2.1 for details) and, for sand deposits under 1 km in any length, as location features in ArcMap. Scour marks were notated as linear features (see Section 4.2.2 for detailed methods).

4.2. Mapping criteria

4.2.1. Sand deposit mapping

The geospatial distribution of sand is dependent, in part, upon the geographic location of its source region and surrounding topographic obstacles or sand traps. Sand is located downwind of its source and upwind of obstacles high enough to block further transport via saltation. In the

Aeolis Dorsa region, sand deposits would be constrained by the highstanding plateaus Aeolis and Zephyria Plana and by the southern highlands. Sand would be expected to concentrate in lowstanding regions as gravity moves sediments downslope, including but not limited to small-scale sediment traps like yardang troughs and large-scale sediment traps like the southern depression. Thus, the distribution of sand—a result of wind and gravity—should provide insight on the relative geographic location of the source region, and was mapped in this study to shed insight on relative geographic source region(s).

Sand deposit polygons were mapped as one of four categories: 1) dark-toned sand found in bedrock troughs (Fig. 4.1a); 2) light-toned sand found in bedrock troughs (Fig. 4.1b); 3) dark-toned sand sheets (Fig. 4.1c); 4) light-toned sand sheets (Fig. 4.1c). Table 2 lists criteria for each category that were used to map all sand deposits. Sand deposits in troughs were consolidated into a single polygon in cases where very small dark sand deposits are located very close (<500 m) to one another.

4.2.2. Scour mark mapping

The goal of scour mark mapping is to identify inferred sand transport wind directions. Scour mark measurement was confined to scour marks located within loose sediment deposits. Features resembling scour marks that occur in lithified bedrock were not measured because these features are either representative of longer-lived wind regimes than would be necessary to form aeolian features in loose sediment, or they are representative of past wind regimes. The distinction between scours in loose sediment and in lithified sediment is made based on: 1) the appearance of sediment buildup in front of moats for loose sediment deposits vs. the common lack thereof in front of lithified moats; and 2) the smooth surface of material in front of moats for loose sediment vs. the commonly-rough surfaces surrounding moats in lithified material (Fig. 4.2).

The entire study area was scanned in a gridlike pattern for all scour marks within sand deposits, and all scour marks in sand deposits were recorded. Scour mark orientations were annotated as linear features, with the ends of each line located at the ends of each moat (Fig. 4.3). Moats cast

shadows on sand, so the endpoints of shadows were used as linear segment endpoints, unless a scour mark was obviously visible beyond the extent of crescentic shadows.

To analyze scour mark orientations (and inferred transport winds), azimuthal orientations of scour mark linear features were calculated. All scour mark linear features mapped in ArcMap are included in an attribute table with details of each linear feature, including a unique object ID and the shape length. The feature latitude and longitude and the azimuthal orientation of features were then manually added to the table. The latitude and longitude of the scour mark midpoints were derived via the 'Calculate Geometry' tool in ArcMap, and linear feature orientations were calculated via the 'Field Calculator' tool in ArcMap. See Appendix I for code used in 'Field Calculator' to determine orientation.

Linear features denoting scour marks only indicate the orientation of the scour, which empirically could mark one of two possible—and opposite—wind directions. For example, a measured scour mark orientation of 45° could, depending on which side of an obstacle the scour is located, indicate either northwesterly or southeasterly winds (both normal to the measured orientation). The correct directions *from* which the winds were blowing were entered manually in MS Excel using azimuthal orientations and the manually-entered hemisphere of inferred transport winds.

4.2.3. Potential sites of *in situ* sand generation: HiRISE

External regional sources are evaluated via geospatial sand distribution and inferred transport wind directions, whereas local sources may be additionally supported by visual evidence of bedrock erosion. Visual clues include features like visual evidence of bedrock erosion via rock slide or slump tracks, or continuous sediment trains (Bateman et al., 2012; Chojnacki et al., 2014c). Material eroding from bedrock must also be of equal or larger sediment size to that of the sediment in question (e.g., Jakosky, 1986). For Aeolis Dorsa, bedrock erosion would be implied by bedrock layers that are visibly breaking up to sediment that is larger in size than sand deposits. This eroded material would then fall downslope in visible trails, possibly into areas where sand is

present. In my methodology, these criteria constitute identification of bedrock as a source of sand. Support for various potential sand sources is evaluated according to criteria listed under the hypotheses (section 3) and the sand distribution and inferred paleowind directions that would support each hypothesis are shown in Fig. 3.1.

In situ sand generation is typically evidenced by a site of origination in bedrock that is connected to subsequent sand deposits by a visible corridor (e.g., Tirsch et al., 2011; Chojnacki et al., 2014b, 2014c). In AD, map-projected HiRISE images covering dark sand deposits were uploaded to ArcMap and subsequently studied at a scale of ~1:4,000 (see Appendix II for HiRISE stamps used out of all stamps in study area), during which talus slopes (e.g., potential origination sites) and talus slopes extending to dark sand deposits (e.g., likely origination sites) were marked as point features in ArcMap. This map of potential sand generation sites is useful because it visually illuminates talus slope hotspots, which are potentially generating sand. This method, although useful for identifying these sand generation sites, is limited to the extent of HiRISE coverage over the study area and thus an incomplete map of talus slopes across Aeolis Dorsa. In this study, the resulting map is used only to describe bedrock that is potentially generating some sand in Aeolis Dorsa.

4.3. Hierarchical clustering analyses

The term 'clustering analysis' encompasses a number of approaches to grouping data based on similarities and/or dissimilarities. Clustering analyses include methods such as hierarchical clustering (wherein data points are grouped stepwise, with each 'step' grouping two data points with the most similarity), *k*-means clustering (in which data are grouped into *k* clusters according to similarity), or density-based clustering (in which data are grouped by data cloud, with remaining data points generally considered outliers). Different needs require different methods; for example, *k*-means clustering is useful for analyses requiring a specific number of clusters with no need for a stepwise function, whereas hierarchical clustering is useful for studies requiring successive

grouping of data points, or for working dynamically with datasets (where the aims of data analysis may change; e.g., Tran, 2016).

In addition to these clustering methods, additional spatial analyses may be used for certain studies. Such analytic methods include multi-distance spatial analysis algorithms (a method that calculates clustering at various distance intervals, e.g., Ripley's K function in ArcGIS), spatial autocorrelation techniques (which identify clusters of adjacent or overlapping features, such as Anselin Local Moran's i in ArcGIS), and hot spot analyses (which identies regions with high and low data point values, such as the Hot Spot analysis tool in ArcGIS).

I chose to perform a clustering analysis on sand deposits because identifying clusters provides objective support for certain hypotheses based on spatial location of clusters. In addition to parsing sand deposits into discrete clusters, hierarchical clustering is a versatile analytic method that can be applied to various types of data—such as shape, size, and orientation of features. Thus, by using hierarchical clustering to analyze spatial trends of sand deposits, researchers can use the same technique in future work. For this study, I performed a hierarchical analysis on sand deposit locations, using sand deposit polygon latitude and longitude as input for the hierarchical cluster algorithm (Appendix III shows example input dialog).

This study also required an approach for identifying spatial groups of scour marks to identify local paleo-wind directions as they may relate to a larger paleo-wind regime within Aeolis Dorsa. I chose a hierarchical clustering approach for this task because hierarchical clustering algorithms group data into clusters stepwise, the steps of which can be seen in the accompanying dendrogram (a hierarchical tree that enables visual analysis of spatial relationships between groups of data points; example shown in Appendix IV). Additionally, separating scours into clusters allows for straightforward comparison of scour orientatinons within each cluster to predicted outcomes for each hypothesis. Hierarchical clustering is determined either by an agglomerative procedure, beginning with individual data points and working up to a single supercluster, or by a divisive approach, beginning with a single supercluster and separating data

into successively smaller clusters, ending with individual data points. I ran the Hierarchical Cluster tool using both methods, both of which created the same dendrogram. In hierarchical clustering, distance can be evaluated by different criteria. These criteria include, e.g., nearest neighbor, average between-groups linkage, and furthest neighbor methods. I chose to use between-groups linkage distance criteria because of its utility in comparing first-order clusters (clusters made of individual data points). The between-groups linkage method first measures distances against individual data points to create smallest-order clusters, then compares the average location of all points within each cluster to form an additional tier of clusters, then repeats the latter process.

Scour marks are indicative of past wind regimes—one of the criteria in this study for evaluating hypotheses for sand sources (see section 3). Working hypotheses 1-3 postulate regional wind regimes with (according to hypotheses 1-3) northerly, easterly, or southerly winds blowing through AD. Working hypothesis 4 (*in situ* sand generation from MFF) postulates local, topographically-controlled winds, where dominant wind directions are variable across AD and broadly follow topographic trends (see Section 3 and Fig. 3.1). Clusters of scour marks within AD provide insight on where winds blew that were strong enough to move sands, a requirement of expected wind regimes associated with each working hypothesis. This study required an objective method of grouping scour marks, scattered throughout AD, into spatial clusters, and used hierarchical clustering because I could examine cluster tiers in addition to the first-order clusters. Hierarchical clustering is especially useful for large datasets in which groups may otherwise be difficult to identify. Here, I imported the latitude and longitude of scour marks (see section 4.2.2 for scour mark mapping) as variables for the 'Hierarchical Cluster' tool within the IBM program SPSS Statistics 25 (hereafter called SPSS).

4.4. Scour mapping error analysis

The Lambert albedo of pixels within CTX images is estimated to have a 10-20% error (Bell et al., 2013). The albedo of scour marks in CTX images is distinctly darker than that of the surrounding pixels (e.g., Fig. 4.3), but the albedo at each end of scour marks typically fades to a

lighter tone. Both the 10-20% error margin for CTX albedo and the fact that scours fade into the surrounding surface raise the potential for error in scour mark measurements. To evaluate human error considering also the preexisting uncertainty in albedo, a second partial mapping effort was conducted.

Error analyses for scour mark orientations were conducted via third-party mapping based on the methods of this study. The third party is knowledgeable of Aeolis Dorsa and familiar with ArcMap mapping techniques using orbital images for feature identification, but unfamiliar with the methods in this work or with mapping of scour marks. The third party created linear features indicating scour orientation on a random set of 62 scour marks (10% of total scours mapped by me). The person was given two items: (1) an ArcMap file containing a layer file with point features marking 62 random scour marks, along with the CTX base map of the study area; and (2) a copy of section 4.2.2 of this work, which outlines the methodology for mapping scours and provides visual examples for scour delineation. This person then mapped scour mark orientations on each of the 62 random scour marks.

The results of the error analyses are reported based on average inferred transport directions for each spatial grouping of scours and standard deviation between each mapping effort. The average difference between the orientations of each mapped scour and the standard deviation of the differences will be reported. These errors will be considered when discussing results of scour mark orientations and their implications for sand transport wind directions. Absolute error reporting—i.e., a percentage difference of orientation for each scour—is not feasible for this study, because the error of 10-20% for albedo measurements will vary by CTX image. CTX images are not calibrated relative to one another, and furthermore have a vignette effect on their sides, making absolute albedo uncertainty calculations unreliable.

4.5. Geologic and stratigraphic relationships

Sand deposits mapped in ArcMap were overlaid, also in ArcMap, on a complete but unpublished geologic map of the Aeolis Dorsa region (most recent version seen in Jacobsen et

al., 2018) to evaluate relative sand cover over geologic units of varying ages. In ArcMap, a tabulate intersection was conducted to find all areas where sand overlaid different units. Sand deposits are, by necessity, more recently emplaced than the age of the underlying units, so these units place maximum ages on sand deposits.

5. RESULTS AND ANALYSES

5.1. Sand distribution

Sand within Aeolis Dorsa lies largely on the peripheries of Aeolis and Zephyria Plana, and within the southern depression (Fig. 5.1). Sand is tightly clustered on the periphery of Aeolis Planum and in the southern depression. Sand clusters less tightly on the peripheries of Zephyria Planum and in north Aeolis Dorsa (Fig. 5.1). Sand distribution areas of each sand deposit classification (described below) were calculated in MS Excel.

Sand in the southern depression is distributed laterally, beginning just north of the highland-lowland boundary and extending ~32 km north-south and ~160 km east-west (Fig. 5.1). Individual sand deposits lie in low-standing terrain, between yardangs or other bedrock outcrops. No sand deposits were observed on top of high-standing bedrock blocks in this area. More dark sand than light-toned (dust-covered) sand is observed in this area, but light-toned sand sheets occur. In the southern depression, dark-toned sand comprises ~85% of all mapped sand; light-toned sand deposits comprise the remaining ~15%. Dark sand is present mainly as deposits within bedrock troughs, whether between elongate yardangs or bedrock blocks; light-toned sand is present mainly as smooth sand sheets.

On Aeolis Planum, dark sand is found in small isolated patches in southern Aeolis Planum (e.g., Fig. 5.2) and as discontinuous light-toned sand sheets on the eastern side of Aeolis Planum (Fig. 5.1). Sand deposits in southern Aeolis Planum are elongate generally east-west. These sand deposits are located adjacent to small cliffs on the south side of rough eroded cliffs within the MFF. Transverse dunes are visible in some of these deposits, oriented north-south. On Aeolis Planum, sand deposits are elongate northwest-southeast, broadly parallel with surrounding bedrock. Here sand extends roughly 165 km northwest-southeast and 40 km northeast-southwest (Fig. 5.1). Sand deposits occur between high-standing bedrock, and as sand sheets peppered with scour marks and associated echo dunes. The majority (94%) of sand deposits mapped in Aeolis Planum are light-toned; the remaining 6% are dark-toned. Light-toned sand

overwhelmingly occurs as sand sheets: >99% of light-toned sand in this region occurs in sheets; <1% of light-toned sand is limited to narrow troughs. Of dark sand in Aeolis Planum, ~66% occurs as narrow inter-yardang trough deposits and ~33% occurs as dark sand sheets.

Sand deposits in south-central Zephyria Planum are tightly constrained to a northwest orientation, extending ~165 km northwest-southeast and ~3 km northeast-southwest (Fig. 5.1). In this area, relative abundance of light and dark-toned sand is roughly split 50%-50%. In south and central Zephyria Planum, sand deposits are also tightly constrained to yardang troughs. Some dark sand deposits also occur adjacent to high-standing bedrock cliffs. In northern Aeolis Dorsa, sand deposits occur as both dark- and light-toned deposits, with dark sand comprising ~63% of sand in this area and light-tones sand comprising the remaining ~27% (Fig. 5.1). Sand deposits run lengthwise along trough lengths. Seventy percent of all sand in northern Aeolis Dorsa lies within troughs. The remaining ~30% lies to the north of N-S-oriented yardangs.

Fewer than 10 small sand deposits occur in the AZP medial basin. These deposits occur either in yardang troughs in crater basins or surrounding small impacts as dark ejecta. The morphology of yardangs in these craters is consistent with yardang morphology of those on Aeolis and Zephyria Planum.

5.2 Hierarchical clustering results

Within the Hierarchical Cluster procedure in SPSS, I set no maximum number of clusters for sand deposits or scour marks, instead allowing the algorithm to identify clusters without a maximum limit. The Hierarchical Cluster procedure produced a dendrogram of 18 clusters of sand deposits (Fig. 5.3) ranging in size from a single sand deposit (cluster 18, located in north center of AD) to 52 sand deposit polygons (cluster 8, located on Aeolis Planum). Clusters 2, 8, 10, and 15 show denser deposits with some polygons scattered around cluster edges, but other clusters show more scattered deposits. These clusters were then overlaid on predicted sand distribution patterns for each of the four working hypotheses (Fig. 3.1; Table). One cluster, 17, overlaps with predicted sand distribution for Elysium Mons as an external source. Two clusters, 11 and 16,

overlap with predicted sand distribution for sand sourced from the Cerberus plains. Three clusters, 1, 2, and 3, are located within the predicted distribution range for sand sourced from the southern highlands. Eleven clusters—4, 6, 7-9, 12-13, and 15-18—all lie within predicted sand distribution ranges for sand produced *in situ* from erosion of the MFF.

The Hierarchical Cluster procedure identified only five clusters of scour marks in its first-order agglomeration procedure (colored boxes of the simplified dendrogram in Fig. 5.4; complete dendrogram in Appendix IV). These five clusters are located in different regions within AD, satisfying the goals of the clustering analysis; namely, that clustering analysis defines clusters of scour marks within AD (see Section 4.3) that I can use for further analyses. These five clusters are as follows: a 22-scour cluster in north Aeolis Dorsa; a 69-scour cluster in northeast Zephyria Planum; a four-scour cluster in central Zephyria Planum; a 513-scour cluster in Aeolis Planum; and a 13-scour cluster in the Southern Depression (Fig. 5.4).

Each scour mark mapped in this study has a unique ID number that was automatically generated by ArcMap while mapping. These unique IDs were imported into SPSS as labels for each data point and were listed on the dendrogram created by the Hierarchical Clustering tool (Appendix IV). Returning to ArcMap, I used these unique ID numbers to separate scours into each of the five clusters. I created a new layer for each cluster of scours and gave each cluster a different color (see map accompanying dendrogram in Fig. 5.4). This process of re-mapping scour clusters in ArcMap highlighted the spatial separation of these clusters. With scour marks successfully clustered by location, I then performed inferred paleo-wind analyses on each of these clusters, the results of which are described in Section 5.3 below.

5.3. Scour mark orientations and paleo-winds

Scour marks in Aeolis Dorsa, numbering 621 in total, occur in five groups determined via hierarchical clustering: (1) in the southern depression; (2) on the eastern side of Aeolis Planum; (3) north of the AZP medial basin; (4) in central Zephyria Planum; and (5) on northeast Zephyria Planum (Fig. 5.4). To display scour mark variance and average directions, rose diagrams were

created for scour mark orientations within each of these five groups of scour marks in the program GeoRose (Fig. 5.5). In addition to the >600 scour marks, there are also a few wind streaks, which also indicate sand transport direction. However, because fewer than five dark streaks are present in Aeolis Dorsa and all five streaks occur in the southern depression, they are hereafter dismissed.

The overwhelming majority of scour marks occur within sand deposits on the eastern side of Aeolis Planum (82% of all scours in Aeolis Dorsa). The average transport wind direction inferred by Aeolis Planum scours is northwesterly (318°), with a mode of 321° and a standard deviation of 30° (Fig. 5.5). In the southern depression (2% of all scours), scour mark orientations are more northerly, with inferred average cardinal wind direction of 325°, a median of 324° and standard deviation of 93° (Fig. 5.5). In central Zephyria Planum (0.6% of all scours), orientations returned the same average northwesterly inferred wind direction of 341° with an identical mode (341º) and a smaller standard deviation of 11° (Fig. 5.5). On the northeast side of Zephyria Planum (11.1% of all scours), scour mark orientations average a southeasterly direction of 123°, a mode of 117°, and a standard deviation of 75° (Fig. 5.5). In northern Aeolis Dorsa (3.5% of all scours), scour marks imply westerly winds with an average inferred wind direction of 246°, a mode of 246° and a standard deviation of 34° (Fig. 5.5).

For every locality except northern Aeolis Dorsa, the inferred wind directions for sand transport broadly follow the orientations of yardang fields. In the southern depression, inferred paleo-wind directions are variable but broadly northwesterly. Inferred wind directions via scours in the southern depression broadly follow high-standing bedrock outcrop orientations, which are similarly variable but also oriented broadly N-S. On Aeolis Planum, scours also follow a northwesterly wind direction, consistent with bedrock orientation surrounding sand deposits, although with distinctly less variability than scours in the southern depression. In northeast Zephyria Planum, where scour marks suggest southeasterly transport winds, yardangs are also oriented SE-NW. Northern Aeolis Dorsa is the only locality where inferred wind direction via scour marks do not correlate with bedrock orientations. In northern Aeolis Dorsa, the average inferred

paleo-wind direction is toward the east-northeast, but these scour marks are located between yardangs oriented N-S (Fig. 5.6). Paleo-wind directions, inferred via scour marks, broadly match the orientation of NE-SW-oriented yardangs located just north of the scour marks (Fig. 5.6). No scour marks are present in any of the abundant sand deposits in south-central Zephyria Planum.

To evaluate potential variation in scour mark orientations, data collected by the third party (see section 4.4) was compared with data collected by A. Boyd. A box-and-whisker plot composed of all scour marks in AD was created (Fig. 5.7), onto which average values from third-party mapping efforts were overlain. For two of the three areas in which the third party mapped scours, Northeast Zephyria Plaum and Aeolis Planum, third party averages fell within 25% deviation from mapping by A. Boyd. Third party mapping efforts in North Aeolis Dorsa returned an average outside of the second and third quartile values (Fig. 5.7) but still in broadly the same direction as mapping by A. Boyd. Because the purpose of scour mark annotation in this study is to qualitatively evaluate support for various potential sources, I consider this disparity to be acceptable for the purposes of this study. However, any future study of this area that would use scour mark orientations for quantitative analyses would need to revisit scours in this region.

5.4. Bedrock erosion in Aeolis Dorsa

Erosion of bedrock to dark sediment, observed in HiRISE images available for the region, was most prevalent in the southern depression and Aeolis planum (Figs. 5.8 and 5.9). Throughout the southern depression, thick layers of dark sediments are eroding via talus slopes. In many cases dark sediments abruptly end where lighter-toned slopes begin. Figure 5.8 shows erosional patterns that are nearly ubiquitous throughout the southern depression, including talus slopes and coarse boulders falling. Figure 5.9 shows a map detailing instances of potential *in situ* sand generation in HiRISE images available for Aeolis Dorsa. These localities are those that exhibit dark talus slopes originating from layers in bedrock and, in some cases, extending to dark sand deposits. Mapping efforts are limited by HiRISE cover, so additional sites of potential sand

generation are likely present in Aeolis Dorsa, especially near stamps shown in map in Appendix II..

In Aeolis Dorsa, the MFF in some localities shows apparent erosion of coarse aggregates of MFF material (Fig. 2.2a), but most of this coarse material appears to be light-toned and inferred to be covered with variable amounts of dust. Dark sand occurs in yardang troughs (e.g., Fig. 4.1a), surrounded by light-toned material in all but one locality covered by HiRISE images (Fig. 5.10). In this locality, one occurrence of bedrock erosion to dark sediments leads to a dark sand deposit. Talus slopes are visible in this locality. Mapping instances of apparent erosion in Aeolis and Zephyria Plana was unsuccessful due to the highly limited HiRISE coverage and the relative scarcity of such instances, but the few instances noted showed the same features as those seen in Fig. 5.10.

5.5. Geologic context

Out of the 377 sand deposits mapped as polygons in the Aeolis Dorsa study area, the majority (91%) are evenly areally distributed across Hesperian-Amazonian MFF units (as Aeolis and Zephyria Plana) and Noachian-Hesperian highland transitional units of the southern depression. Out of all sand deposits in the study area, 8% are located on basinal units ('Aeolis Dorsa units'; Jacobsen et al., 2018a) and less than 1% of sand is located on southern highlands terrain (Table 5).

6. DISCUSSION

Each of the scour mark clusters defined via the SPSS Hierarchical Cluster tool records a dominant sand transport direction (Fig. 5.7). These sand transport directions point away from potential sources of sand (arrows in Figs. 3.1-3.4). Inferred transport winds may provide partial support for possible sources of sand, but the feasibility of sand transport from such sources is dependent also upon elevation changes, surface roughness, and obvious obstacles. Thus, potential sources (Figs. 3.1-3.4) must be evaluated with consideration for feasible sand transport distances and pathways.

6.1. Limits to sediment transport distances

Surface roughness affects the distance sand-sized sediment can be transported both directly and indirectly. Rough surfaces directly affect the distance sand can be transported due to sand being stopped by the physical barrier of high-standing obstacles (barriers indicated in Figs 3.1-3.4; Greeley and Iversen, 1985). According to the Prandlt-von Karman equation, 'the Law of the Wall' (Lorenz and Zimbelman, 2014), surface roughness is inversely correlated with wind velocity: the higher the surface roughness relative to the wind velocity at a given height, the lower the wind velocity. Thus, wind velocity will be low across rough and uneven surfaces, and would be unlikely to remain consistently strong across any significant distance (Lorenz and Zimbelman, 2014, and references therein). Evidence of topography-limited sand transport exists where sediment appears trapped by topography. One excellent example of topography-limited transport is shown in Figure 6.1. in this figure, sand appears to have been transported across a yardang only up to a certain yardang height, suggesting that sand transport across the yardang was height-limited.

6.2. Evaluation of support for working hypotheses

6.2.1. Elysium Mons as a source of sand in Aeolis Dorsa

Sand is distributed throughout Aeolis Dorsa, but relatively little sand is seen in northern AD. One single cluster, 17, lies within the predicted sand distribution for sand sourced from Elysium

Mons (predicted area is shaded blue in Fig. 3.1). Other sand deposits occur towards the north of the study area (e.g., cluster 18, Fig. 5.3), but these are located south of rough topography. These other clusters do not agree with predicted sand deposit locations, which thereby reduces the likelihood that these sand deposits were emplaced from a northern source. One other possibility exists in addityion to predicted north AD sand distribution: sand transported southward within the AZP medial basin.

Sand deposit mapping shows that sand within the AZP medial basin is limited to small intracrater deposits (Fig. 5.1). In the event that wind transported sediment southward within the medial basin, sediment would be concentrated on, and potentially wrapping around, the northern side of bedrock obstacles (shaded area in Fig. 3.1). However, sand is distributed on all sides of bedrock blocks and yardangs throughout Aeolis Dorsa. In northern Aeolis Dorsa, sand is concentrated on the north side of north-south-oriented yardangs (Fig. 5.1), but sand coming from Elysium Mons would still have to bypass northern yardang fields with yardangs up to 100 m in relief.

In the second scenario, explosive volcanism and resultant sediment settling in Aeolis Dorsa would produce a distribution of sand-sized sediment found both in topographic lows and highs. Such sediment would initially blanket the entire region before being moved. Sediment settling sourced from explosive Elysium Mons volcanism would still likely settle in the northern half of the study area. Sand deposit mapping shows comparatively little dark sand in the northern half of the study area. This distribution of sand does not explicitly disprove this explosive volcanism hypothesis, but at the same time provides little support for explosive Elysium Mons volcanism as a preferred source of sand in Aeolis Dorsa.

6.2.2. Cerberus Plains lavas as a source of sand

Predicted sand distribution for this hypothesis is along the northeast side of Aeolis Dorsa (predicted sand deposit locations shaded green in Fig. 3.2). Two clusters (16 and 17; Fig. 5.3) lie within the predicted sand distribution according to the Cerberus plains hypothesis. These sand

deposits (Fig. 5.1) are limited to topographic lows between NE-SE-oriented yardangs rather than on the northern sides of of topographic obstacles as would be expected for sands transported from the northeast.

Orientations of scour marks within these sand deposits (NE Zephyria Planum cluster, Fig. 5.4) do not match scour orientations for predicted northeasterly winds, as would be expected for sand sourced from the Cerberus Plains (arrows in Fig. 3.2). The inferred average sediment transport wind direction of 123°, indicating southeasterly winds (Fig. 5.7), is inconsistent with sand transport from the Cerberus Plains lavas relative to the location of sand clusters 16 and 17 (Fig. 3.1), because the Cerberus Plains are located the northeast, not the southeast, of these deposits. This dark sand could have been transported from the Cerberus Plains by northeasterly winds, with more recent southeasterly winds forming the scour marks and echo dunes observed. However, due to the large yardang field—with yardangs tens of meters high—located to the northeast of these sand deposits, sand is unlikely to have reached its current location by transport directly southwestward from the Cerberus Plains.

6.2.3. Southern highlands as a source of sand

Expected observations (Fig. 3.3) that would support the hypothesis that sand is sourced from the southern highlands south of Aeolis Dorsa include a) sand concentrated in the southern depression, a topographic low (pink shading in Fig. 3.3) and b) aeolian features implying southerly transport winds (arrows in Fig. 3.3). Predicted and mapped sand distributions are consistent with one another, with sand clusters 1 through 3 matching predicted sand distribution (predictions in Fig. 3.2; cluster locations shown in Fig. 5.3). Dark sand is concentrated in the southern depression, in between topographic lows surrounding high-standing bedrock blocks (Fig. 5.1). Roughly 54% of all sand mapped in AD falls within one of these three clusters, suggesting that the southern highlands, if in fact a primary source of this sand, supply a majority of sand in Aeolis Dorsa.

However, scour orientations within these sand deposits suggest an average inferred wind direction of 325° (Fig. 5.7), implying northwesterly transport winds. This result is inconsistent with a predicted southerly transport wind direction (arrows in Fig. 3.3) that would support the southern highlands proper as the source for this sand. This inconsistency could be resultant of post-depositional winds forming scours and dark streaks in the pre-existing sediment and thus does not eliminate the possibility of the southern highlands proper as a sand source, but it provides no support for the southern highlands as an external regional source of sand in Aeolis Dorsa.

The second scenario by which southern highlands materials could serve as a source for this dark sand is if bedrock blocks within the southern depression, which are inferred remnant southern highlands materials, are a source of dark sand. Observations that would support this hypothesis include a) apparent erosion of block wall materials and sediment pathways leading to sand deposits, and b) dark sand distributed throughout topographic lows surrounding inferred remnant southern highlands blocks. Many inferred remnant southern highlands blocks have thick layers of dark-toned material that appear freshly eroded or currently eroding, commonly with talus slopes leading to toughs between bedrock (Fig. 5.8). In the southern depression, dark sand deposits are interspersed between bedrock blocks. Observations of the distribution of sand within the southern depression, coupled with the abundant erosion of dark bedrock layers adjacent to sand deposits, strongly support the hypothesis that at least some sand in Aeolis Dorsa—sand in the southern depression—is sourced from these dark bedrock layers. If these bedrock blocks are remnant southern highlands materials, as suggested in Section 2.5, these observations support the southern highlands as a direct source of at least some sand in Aeolis Dorsa. This result is consistent with previous work identifying southern highlands crater walls as a source of dark sand within crater basins (e.g., Tirsch et al., 2011). This result is inconsistent, however, with the inferred transport directions for scour marks occurring in these sand deposits, which infer broadly northwesterly transport. Scour mark orientations in the southern depression infer an average sand transport direction of ~161° (Fig. 5.7; Table 3), implying a possible sand source to the northwest

of these sand deposits. To the northwest of these sand deposits is southernmost Aeolis Planum (Fig. 1.1), an area with a high surface roughness. Sakimoto et al. (1999) measured surface roughness across the MFF, including across Aeolis Dorsa. Surface roughness was measured in traverses longitudinally throughout the global extent of the MFF; one traverse runs through the middle of the southern depression (Pass 29 from Sakimoto et al., 1999). This traverse shows significant variability in surface height and high surface roughness, which would limit near-surface sediment transport across this area (e.g., Sakimoto et al., 1999). Thus, wind directions inferred by scours in the southern depression are unlikely to result from southwestward sediment transport. This high surface roughness does not support the hypothesis that sand in the southern depression has undergone gross sediment transport—rather, wind directions inferred from sand dune morphology are more likely the result of topographic controls.

6.2.4. The Medusae Fossae Formation (MFF) as an *in situ* source of sand in Aeolis Dorsa

The hypothesis that sand in AD is sourced *in situ* from erosion of the MFF would be supported indirectly by sand deposits overlying the MFF and by nonexistent or locally-controlled wind directions (Fig. 3.4; shading shows expected sand deposit locations and arrows show wind directions). Eleven sand clusters overlie the MFF (Fig. 5.3) in agreement with predicted distribution (Fig. 3.4). Because the predicted sand distribution for this hypothesis is extensive, sand deposits and scours on Aeolis Planum, northern Aeolis Dorsa, northeast Zephyria Planum, and central Zephyria Planum will be discussed sequentially.

Bedrock orientation in Aeolis Planum generally aligns with average northwesterly sand transport directions, inferred by co-located scour marks, of 318° (Fig. 5.7; Table 3), indicating that if this sediment were sourced externally, its source would likely be located northwest of this region. Northwest of these sand deposits, however, the surface roughness and high relief of yardangs on Aeolis Planum would likely limit sediment from being transported across Aeolis Planum. The inference that sand is unlikely to be transported across Aeolis Planum leaves Aeolis Planum itself as the only potential source northwest of these sand deposits. Whether sand deposits on eastern

Aeolis Planum are sourced from either *in situ* bedrock erosion or sourced from elsewhere on Aeolis Planum, the sediment source in either case is erosion of the MFF itself. Thus, the sand distribution, inferred transport wind direction, and topography surrounding sand deposits on the east side of Aeolis Planum strongly support the hypothesis that sand in Aeolis Dorsa is sourced from erosion of the underlying MFF.

Inferred transport winds in northeast Zephyria Planum are southeasterly at 123°, inconsistent with any external sand source but parallel with yardang orientations surrounding scour marks (shown by arrows in Fig. 3.4). These observations strongly support a topographic control as the primary reason for scour orientation. The likelihood of topographic controls on winds and the discrete, elongate nature of sand deposits provide indirect, but strong, support for *in situ* erosion of the underlying MFF as the source for this sand.

In northern Aeolis Dorsa, inferred westerly sand transport wind directions of 246° imply a potential source of sand to the west of this area. The fact that sand deposits are located between yardangs of one orientation, but whose inferred transport winds indicate a different dominant direction (see sections 5.1 and 5.2), supports the interpretation that wind is shaping sand deposits around obstacles, but may not be driving extensive mass sand transport. If this sand were transported any distance by southwesterly winds as inferred by scour marks, then sand deposits would be elongated in a SW-NE orientation. Instead, sand deposits are found in between yardangs oriented north-south and run parallel with the N-S-oriented yardangs between which sand outcrops (Fig. 6.2). The agreement of the yardangs oriented SW-NE and the scour mark orientations suggests that this yardang field is younger than yardangs oriented N-S.

The observations of sand deposits located within MFF yardangs, the topographic controls on transport winds, and the mismatch between inferred transport wind direction and sand distribution in northern Aeolis Dorsa all strongly support the hypothesis that sand in Aeolis Dorsa is largely sourced *in situ* from eroded MFF materials. All of the above evidence is indirect evidence in support of the underlying MFF as the source of sand in Aeolis Dorsa. Direct evidence supporting

this sand source also exists in the form of bedrock apparently eroding to dark sediments. This apparent dark sediment production occurs on at least two locations in Aeolis Dorsa: first, in Aeolis Planum. and second, in south-central Zephyria Planum. These two localities show possible erosion of a dark layer in the MFF (Fig. 5.10), evidenced in particular by talus slopes. The interpretation that here the MFF is actively eroding is supported by talus slopes on the deposit—evidence for downslope sediment transport. Although the vast majority of the MFF in Aeolis Dorsa is light-toned, this occurrence presents evidence that the light tone is indeed due to dust cover as has been hypothesized previously (e.g., Edgett et al., 1997)—only this layer is dark, although the layer appears to continue beyond the extent of the blue sediment (Fig. 5.10). Indeed, light-toned terrestrial ignimbrites have also been shown to be sources of dark sand (Fig. 6.3; de Silva et al., 2010).

6.3 Relative timing of sand generation and emplacement

Central to the question of sources of sand is the time at which sand was generated, transported and/or emplaced. Information available to investigate this topic include ages of surrounding geologic units and the relationship of sand deposits to those units. Sand must be, at oldest, the same age as adjacent bedrock (if eroding *in situ*) or younger than the underlying bedrock (if transported from elsewhere). Sand must also be emplaced more recently than the formation of the geographic features on or in which sand is located. Such geographic features include craters, sedimentary basins, mesas, and yardangs.

6.3.1 Sand and geologic unit relationships

Sand is distributed equally across the MFF of Aeolis and Zephyria Plana (~45% of all sand in Aeolis Dorsa; Table 5) and over transition units of the southern depression (also at ~45%). Sand covers Aeolis Dorsa basin units to a limited extent (~9%) and has very limited extent (<1%) over the southern highlands units. Sand in each of these locations was, by necessity, emplaced sometime after rock formation and after landscape modification. This temporal constraint places

maximum age of sand emplacement based solely on geologic context at the Noachian/ Hesperian transition (for sand in the southern depression), the mid-Hesperian (for sand on Aeolis and Zephyria Plana), and the late Hesperian (for sand located on the floor of the AZP medial basin). For sand apparently being generated from the southern highlands materials in the southern depression (e.g., Fig. 5.8), I can infer that sand here formed sometime during or after the Noachian/Hesperian transition and subsequently underwent minimal transport. Although similar constraints cannot be placed on sand in Aeolis and Zephyria Plana, other constraints may be made based on yardang orientations and elevations.

6.3.2 Sand and yardang field relationships

Sand on Aeolis and Zephyria Plana is located mainly in pockets or troughs between yardangs oriented E-W rather than yardangs oriented N-S. This relationship may be due to: 1) sand emplaced at lower elevations that correspond with E-W yardangs; 2) sand transported to inter-yardang troughs during a wind regime that predates the more recent N-S wind regime; or 3) sand generation from layers of the MFF associated with E-W yardang fields. Regardless of which of these three options is/are correct, the association of dark sand with E-W yardang fields may indicate a temporal association with the timing of formation of E-W yardangs.

6.3.3 Present-day and recent state of sand movement

Surface textures of dark sand in Aeolis Dorsa include one or more generations of mesoscale ripples and/or scarce dust devil tracks. No HiRISE image pairs in this region reveal any change in bedform or in extent of dust cover, suggesting that—at least since the beginning of the HiRISE mission—sand deposits in Aeolis Dorsa are static. Dark sand in Aeolis Dorsa is free of impact craters, suggesting that dark sand, though static, is unconsolidated. Sand deposits are variably dust-covered (e.g., Fig. 4.1), offering insight into relative wind speeds in the region. Here, winds are apparently sufficiently forceful to deflate dust from dark sand deposits, but not sufficiently high to move sand. Wind tunnel experiments predict that sand grains are more easily entrained by the wind than dust particles (e.g., Iversen et al., 1976; Greeley et al., 1980; Iversen and White, 1982;

Leach and Greeley, 1989), raising a longstanding conundrum of dune fields that appear static, but dust free, like those observed in Aeolis Dorsa. Global Circulation Model (GCM) experiments by Kahre et al. (2006) provided an explanation for this conundrum: that dust on the Martian surface occurs as coarse aggregates, for which minimum entrainment speeds are predicted to be roughly half those of sand grains. Wind tunnel experiments showing that dust aggregates are readily entrained (e.g., Merrison et al., 2007) and observations of wind lifting of dust via the Spirit lander (e.g., Sullivan et al., 2008) both support this hypothesis. I thus suggest that here, dust cover over these bedforms is likely in the form of roughly sand-sized dust aggregates rather than unconsolidated or weakly bonded dust particles.

6.3.4 Summary of timing constraints

Contextual relationships of dark sand with bedrock units and local topography suggest the likelihood that most sand in Aeolis Dorsa was generated in the Hesperian or Amazonian— possibly billions of years ago. The oldest sand in Aeolis Dorsa is probably sand located in the southern depression, which could porentially be as old as late Noachian but is also likely Hesperian in age (e.g., Jacobsen et al., 2018a, 2018b; map in preparation).

If the MFF is generating sand, then dark sand on Aeolis and Zephyria Plana may be Hesperian in age. The confinement of sand to E-W yardang fields suggests that sand emplacement in these localities predates the more recent N-S wind regime. Sand deposits appear static, suggesting that in the last decade (since HiRISE images were taken of sand in the study area) no appreciable sand movement has occurred.

6.4 Cosmopolitan sand sources: limitations of this study

Geospatial sand distribution, scour marks, and instances of apparent bedrock erosion upslope of dark sand deposits provide the most support for two sand sources: the Medusae Fossae Formation itself and the southern depression. Although these two potential sources are supported

by the results of this study, the possibility of myriad sources of sand in Aeolis Dorsa cannot be ruled out.

Many terrestrial sand deposits are sourced from multiple rock units from different localities. Such sands include basaltic sands in Iceland (e.g., Baratoux et al., 2011), quartzofeldspathic sands of the Mojave Desert (e.g., Zimbelman and Williams, 2002), and the Moses Lake dune field in central Washington (e.g., Bandfield et al., 2002). In each of these cases, mineralogical and geochemical variations in sand deposits are linked to multiple sand sources. The commonality of multiple sources of terrestrial sand deposits—especially Mars-analog sites like the basaltic sands of Iceland—suggest that sand deposits on Mars may likewise sometimes have more than once source. On Mars, sand transport pathways are commonly obscured (e.g., McGlynn et al., 2011, 2012), making provenance identification difficult, especially when mineralogical data are unavailable. On Mars, sand deposits with single sources or provenances are limited to local sources (e.g., Tirsch et al., 2011; Chojnacki et al., 2014c); in other localities, multiple sources have been inferred (e.g., McGlynn et al., 2011, 2012; Lapotre et al., 2017) via ground-truthing and spectral comparisons. Although this study only identifies two sources of sand in Aeolis Dorsa— the southern highlands and the MFF—the possibility of additional sand sources cannot be dismissed. Mineralogical analyses, especially via CRISM data, will aid in identification of possible additional sources and is scheduled as the next step in this study.

7. SUMMARY AND IMPLICATIONS

This study addresses one of the most fascinating questions regarding Martian surficial processes today: the conundrum of globally distributed sand with, in many cases, no obvious local sources. In the case of Aeolis Dorsa, erosion of bedrock adjacent to and underlying dark sand deposits is likely sourcing all dark sand in Aeolis Dorsa. The surface roughness and high-standing topographic obstacles are limiting factors for sediment transport, evidenced by topographic controls on sand deposits. Dark sand is located in between bedrock outcrops. In the southern depression, dark sand commonly co-occurs with erosion of thick, dark bedrock layers that record downslope sediment transport in the form of talus slopes. Elsewhere in Aeolis Dorsa, indirect evidence (sand distribution, apparent minimal sand transport, and inferred wind directions controlled by topography) provide support for the underlying MFF as the primary sand source. Direct evidence that the MFF is a source of sand in one locality within Aeolis Dorsa lies on Zephyria Planum, where apparent erosion of layers in the MFF is producing dark sand that coalesces into a sand deposit. This study thus identifies at least two sources of sand in Aeolis Dorsa: *in situ* sand generation via erosion of southern depression bedrock and of the MFF. Bedrock in the southern depression is morphologically similar to the southern highlands, whose nature is varied and unresolved (e.g., Greeley and Guest, 1987). The MFF, the other known source of sand in Aeolis Dorsa, is hypothesized to be an ignimbrite deposit (Mandt et al., 2008, 2009; Ohja and Karunatillake, 2017; Ohja et al., 2017). If the hypothesis that the MFF is volcaniclastic in origin is confirmed, then this study represents identification of possibly the first known mechanism by which sand-sized sediment is generated from igneous materials on the Martian surface. Future work should entail volume calculations of sand occurring on the MFF relative to observed potential generation sites. Additionally, hierarchical clustering can be applied to variables within the sand deposit attribute table (i.e., shape or size), from which additional inferences may be made.

One of the questions asked by planetary geomorphologists for decades is the question of how sand persists and is globally distributed (Hayward et al., 2007, 2014) on Mars despite no obvious local sources for many deposits and the speed at which sand would be comminuted to smaller particles during transport (e.g., Melosh, 2011). The likelihood of MFF as one of the two primary sand sources in Aeolis Dorsa supports the possibility that friable layered deposits on Mars can supply dark sand. Friable layered deposits are widespread on Mars (e.g., Kerber et al., 2012) and are thus a large potential provenance for sand. Currently, one exciting implication is the possibility that the source of sand in Gale Crater may also be the Medusae Fossae Formation. A hypothesized outcrop of MFF materials is present in Gale Crater (Zimbelman and Scheidt, 2012), and occurs adjacent to dark dunes (e.g., Silvestro et al., 2013). This study provides direct evidence that the MFF can produce dark sand (Fig. 5.9), thus raising the possibility that the source of dark sand dunes in Gale Crater may be local and may in fact be igneous.

REFERENCES

Allen, J. R. L., 1984, Sedimentary Structures: Their Character and Physical Basis:

    Developments in Sedimentology: Elsevier, Amsterdam, The Netherlands, 592 p.

Bandfield, J. L., Edgett, K. S., and Christensen, P. R., 2002, Spectroscopic study of the Moses

    Lake dune field, Washington: Determination of compositional distributions and source

    lithologies: Journal of Geophysical Research, v. 107, E11, doi:10.1029/2000JE001469.

Baratoux, D., Mangold, N., Arnalds, O., Bardintzeff, J.-M., Platevoet, B., Gregoire, M., and

    Pinet, P., 2011, Volcanic sands of Iceland - Diverse origins of aeolian sand deposits

    revealed at Dyngjusandur and Lambahraun: Earth Surface Processes and Landforms, v.

    36, p. 1789-1808.

Bateman, M. D., Bryant, R. G., Foster, I. D. L., Livingstone, I., and Parsons, A. J., 2012, On the

    formation of sand ramps: A case study from the Mojave Desert: Geomorphology, v. 161,

    93–109.

Bell, J. F., III, Malin, M. C., Caplinger, M. A., Fahle, J., Wolff, M. J., Cantor, B. A., James, P. B.,

    Ghaemi, T., Posiolova, L. V., Ravine, M. A., Supulver, K. D., Calvin, W. M., Clancy, R. T.,

    Edgett, K. S., Edwards, L. J., Haberle, R. M., Hale, A., Lee, S. W., Rice, M. S., Thomas,

    P. C., and Williams, R. M. E., 2013, Calibration and Performance of the Mars

    Reconnaissance Orbiter Context Camera (CTX): International Journal of Mars Science

    and Exploration, v. 8, p. 1-14.

Bell, J. F., Squyres, S. W., Arvidson, R. E., Arneson, H. M., Bass, D., Blaney, D., Cabrol, N.,

    Calvin, W., Farmer, J., Farrand, W. H., Goetz, W., Golombek, M., Grant, J. A., Greeley,

    R., Guinness, E., Hayes, A. G., Hubbard, M. Y. H., Herkenhoff, K. E., Johnson, M. J.,

    Johnson, J. R., Joseph, J., Kinch, K. M., Lemmon, M. T., Li, R., Madsen, M. B., Maki, J.

    N., Malin, M., McCartney, E., McLennan, S., McSween, H. Y., Ming, D. W., Moersch, J.

    E., Morris, R. V., Dobrea, E. Z. N., Parker, T. J., Proton, J., Rice, J. W., Seelos, F.,

    Soderblom, J., Soderblom, L. A., Sohl-Dickstein, J. N., Sullivan, R. J., Wolff, M. J., and

Wang, A., 2004, Pancam multispectral imaging results from the Spirit Rover at Gusev crater: Science, v. 305, p. 800-806.

Bibring, J. P., Soufflot, A., Berthé, M., Langevin, Y., Gondet, B., Drossart, P., Bouyé, M., Combes, M., Puget, P., Semery, A., Bellucci, G., Formisano, V., Moroz, V., Kottsov, V., and the OMEGA Co-I team: Bonello, G., Erard, S., Forni, O., Gendrin, A., Manaud, N., Poulet, F., Poulleau, G., Encrenaz, T., Fouchet, T., Melchiori, R., Altieri, F., Ignatiev, N., Titov, D., Zasova, L., Coradini, A., Capacionni, F., Cerroni, P., Fonit, S., Mangold, N., Pinet, P., Schmitt, B., Sotin, C., Hauber, E., Hoffmann, H., Jaumann, R., Keller, U., Arvidson, R., Mustard, J., and Forget, F., 2004, OMEGA: Observatoire pour la Minéralogie, l'Eau, les Glaces et l'Activité, *in*: Mars Express: the scientific payload. Ed. Andrew Wilson. ESA SP-1240, Noordwijk, Netherlands: ESA Publications Division, ISBN 92-9092-556-6, 2004, p. 37-49.

Bishop, M., A., 2011, Aeolian scours as putative signatures of wind erosion and sediment transport direction on Mars. Geomorphology, v. 125, p. 569-574.

Bradley, B. A., Grosfils, E. B., and Sakimoto, S. E. H., 2000, Boundaries and stratigraphy of the Medusae Fossae Formation and Elysium basin materials using Mars Orbiter Laser Altimeter (MOLA) data: 31st Lunar and Planetary Science Conference, Abstract no. 2055.

Bradley, B. A., Sakimoto, S. E. H., Frey, H., and Zimbelman, J. R., 2002, Medusae Fossae Formation: New perspectives from Mars Global Surveyor: Journal of Geophysical Research, v. 108, no. E8, p. doi:10.1029/2001JE001537.

Bridges, N. T., Geissler, P. E., McEwen, A. S., Thomson, B. J., Chuang, F. C., Herkenhoff, K. E., Kesthelyi, L. P., and Martínez-Alonso, S., 2007, Windy Mars: A dynamic planet as seen by the HiRISE camera: Geophysical Research Letters, v. 34, L23205, doi:10.1029/2007GL031445.

Bridges, N. T., Bourke, M. C., Geissler, P. E., Banks, M. E., Colon, C., Diniega, S., Golombek,

M. P., Hansen, C. J., Mattson, S., McEwen, A. S., Mellon, M. T., Stantzos, N., and Thomson, B. J., 2012, Planet-wide sand motion on Mars: Geology, v. 40, p. 31-34.

Burr, D. M., Enga, M.-T., Williams, R. M. E., Zimbelman, J. R., Howard, A. D., and Brennand, T. A., 2009, Pervasive aqueous paleoflow features in the Aeolis/Zephyria Plana Region, Mars: Icarus, v. 200, p. 52-76.

Burr, D. M., de Silva, S. L., Zimbelman, J. R., and Bridges, N. T., 2012, Aeolian dunes from volcaniclastic sediments: the Medusae Fossae Formation, Mars, and Andean ignimbrites, Earth. 43rd Lunar and Planetary Science Conference, Abstract no. 1692.

Burr, D. M., Williams, R. M. E., Wendell, K. D., Chojnacki, M., and Emery, J. P., 2010, Inverted fluvial features in the Aeolis/Zephyria Plana region, Mars: Formation mechanism and initial paleodischarge estimates: Journal of Geophysical Research, v. 115, p. E07011, doi:07010.01029/02009JE003496.

Burr, D. M., Zimbelman, J. R., Qualls, F. B., Chojnacki, M., Murchie, S. L., and Michaels, T. I., 2011, The Western Medusae Fossae Formation, Mars: A Possible Source of Dark Aeolian Sand: 42nd Lunar and Planetary Science Conference, Abstract no. 1582.

Chojnacki, M., 2014a, Echo Dune. *In*: Encyclopedia of Planetary Landforms. Springer, New York, NY.

Chojnacki, M., 2014b, Burr. D. M., and Moersch, J. E., 2014, Valles Marineris dune fields as compared with other martian populations: Diversity of dune compositions, morphologies, and thermophysical properties: Icarus, v. 230, p. 96-42.

Chojnacki, M., Burr, D. M., Moersch, J. E., and Wray, J. J., 2014c, Valles Marineris dune sediment provenance and pathways. Icarus, v. 232, p. 187-219.

Chojnacki, M., Moersch, J. E., and Burr, D. M., 2010, Climbing and falling dunes in Valles Marineris, Mars: Geophysical Research Letters, v. 37, L08201.

Christensen, P. R., Bandfield, J. L., Smith, M. D., Hamilton, V. E., and Clark, R. N., 2000,

Identification of a basaltic component on the Martian surface from Thermal Emission
Spectrometer data: Journal Geophysical Research, v. 105, p. 9609–9621.

de Silva, S. L., Bailey, J. E., Mandt, K. E., and Viramonte, J. M., 2010, Yardangs in terrestrial
ignimbrites: Synergistic remote and field observations on Earth with applications to Mars:
Planetary and Space Science, v. 58, no. 4, p. 459-471,
doi:http://dx.doi.org/10.1016/j.pss.2009.10.002

Edgett, K. S., 1997, Aeolian Dunes as Evidence for Explosive Volcanism in the Tharsis Region
of Mars: Icarus, v. 130, p. 96-114.

Edgett, K. S., Butler, B. J., Zimbelman, J. R., and Hamilton, V. E., 1997, Geologic context of the
Mars radar "Stealth" region in southwestern Tharsis: Journal of Geophysical Research, v.
102, p. 21545-21567.

Edgett, K. S., 2002, Low-albedo surfaces and eolian sediment: Mars orbiter camera views of
western Arabia Terra craters and wind streaks: Journal of Geophysical Research,
v. 107, no. E6, doi:10.1029/2001JE001587.

Edgett, K. S., and Lancaster, N., 1993, Volcaniclastic aeolian dunes: Terrestrial examples
and application to martian sands: Journal of Arid Environments, v. 25, p. 271-297.

Edgett, K. S., and Rice, J. W, 1995, Very Young Volcanic, Lacustrine, and Fluvial Features of
the Cerberus and Elysium Basin Region, Mars: Where to Send the 1999 Mars Surveyor
Lander: Abstracts of the Lunar and Planetary Science Conference, v. 26, p. 357-358.

Fagents, S. A., and Wilson, L., 1996, Numerical Modeling of Ejecta Dispersal from Transient
Volcanic Explosions on Mars: Icarus, v. 123, p. 284-295.

Fenton, L. K., 2005, Potential sand sources for the dune fields in Noachis Terra, Mars: Journal
of Geophysical Research, v. 110, E11004, doi:10.1029/2005JE002436

Fenton, L. K., 2008, Gullies as a source of aeolian sand in the southern midlatitudes: Workshop
on Martian Gullies: Theories and Tests, Abstract no. 8039.

Fenton, L. K., and Bandfield, J. L., 2003, Aeolian processes in Proctor Crater on Mars:

Sedimentary history as analyzed from multiple data sets: Journal of Geophysical Research, v. 108, no. E12, 5129, doi:10.1029/2002JE002015.

Fenton, L. K., Toigo, A. D., and Richardson, M. I., 2005, Aeolian processes in Proctor Crater on Mars: Mesoscale modeling of dune-forming winds: Journal of Geophysical Research, v. 110, E06005, 18 p.

Fishbaugh, K. E., Poulet, F., Chevrier, V., Langevin, Y., Bibring, J.-P., 2007, On the origin of gypsum in the Mars north polar region: Journal of Geophysical Research, v. 112, E07002, doi: 10.1029/2006JE002862.

Greeley, R., Bridges, N. T., Kuzmin, R. O., and Laity, J. E., 2002, Terrestrial analogs to wind-related features at the Viking and Pathfinder landing sites on Mars: Journal of Geophysical Research, v. 107, E1-5005.

Greeley, R., and Guest, J., 1987, Geologic map of the eastern equatorial region of Mars: U.S. Geological Survey, Miscellaneous Investigations Series Map, no. I-1802b, scale 1:5,000,000.

Greeley, R., and Iversen, J. D., 1985, Wind as a Geological Process: on Earth, Mars, Venus and Titan, Cambridge University Press, Cambridge Planetary Science Series, 333 p.

Greeley, R., and Kraft, M. D., 2001, Survivability of Aggregate Sands on Mars: 32nd Lunar and Planetary Science Conference: Houston, Lunar and Planetary Institute, Abstract #1839.

Greeley, R., Leach, R., White, B., Iversen, J., and Pollack, J., 1980, Threshold windspeeds for sand on Mars: Wind tunnel simulations: Geophysical Research Letters, v. 7, p. 121– 124, doi:10.1029/GL007i002p00121.

Greeley, R., Whelley, P. L., Neakrase, L. D. V., Arvidson, R. E., Bridges, N. T., Cabrol, N. A., Christensen, P. R., Di, K., Foley, D. J., Golombek, M. P., Herkenhoff, K., Knudson, A.,

Kuzmin, R. O., Li, R., Michaels, T., Squyres, S. W., Sullivan, R., and Thompson, S. D., 2008, Columbia Hills, Mars: Aeolian features seen from the ground and orbit: Journal of Geophysical Research, v. 113, E6-E06S06.

Hansen, C. J., Thomas, N., Portyankina, G., McEwen, A., Becker, T., Byrne, S., Herkenhoff, K., Kieffer, H., and Mellon, M., 2010, HiRISE observations of gas sublimation-driven activity in Mars' southern polar regions: I. Erosion of the surface: Icarus, v. 205, p. 283-295.

Hartmann, W. K., and Neukum, G., 2001, Cratering chronology and the evolution of Mars: Space Science Reviews, v. 96, p. 165-194.

Hayward, R. K., Fenton, L. K., and Titus, T. N., 2014, Mars Global Digital Dune Database (MGD[3]): Global dune distribution and wind pattern observations. Icarus, v. 230, p 38-46.

Hayward, R. K., Mullins, K. F., Fenton, L. K., Hare, T. M., Titus, T. N., Bourke, M. C., Colaprete, A., and Christensen, P. R., 2007, Mars Global Digital Dune Database and initial science results. Journal of Geophysical Research, v. 112, E11007.

Horgan, B. H. N., and Bell, J. F. III, 2012, Widespread weathered glass on the surface of Mars: Geology, v. 40, p. 391-394.

Hynek, B. M., Phillips, R. J., and Arvidson, R. E., 2003, Explosive volcanism in the Tharsis region: Global evidence in the Martian geologic record: Journal of Geophysical Research, v. 108, doi:10.1029/2003JE002062.

Irwin, R. P. III, and Watters, T. R., 2010, Geology of the Martian crustal dichotomy boundary: Age, modifications, and implications for modeling efforts: Journal of Geophysical Research, v. 115, E11.

Iversen, J. D., and White, B. R., 1982, Saltation threshold on Earth, Mars and Venus: Sedimentology, v. 29, p. 111 – 119, doi:10.1111/j.1365-3091.1982.tb01713.x.

Iversen, J. D., Greeley, R., and Pollack, J. B., 1976, Windblown dust on Earth, Mars and Venus, Journal of Atmospheric Sciences, v. 33, p. 2425–2429, doi:10.1175/15200469(1976)033<2425:WDOEMA>2.0.CO;2.

Jacobsen, R. E., and Burr, D. M., 2017, Dichotomies in the fluvial and alluvial fan deposits of the Aeolis Dorsa, Mars: Implications for weathered sediment and paleoclimate: Geosphere, v. 36, p. 2154-2168.

Jacobsen, R. E., and Burr, D. M., 2018, Synthesizing the history of a diverse inverted landscape: Mapping of the Aeolis Dorsa region, Mars: 49th Lunar and Planetary Science Conference, Abstract no. 2057.

Jacobsen, R. E., Burr, D. M., Peel, S. E., Borden, R. M., and Boyd, A. S., 2018, Understanding the History of a Diverse Inverted Landscape: Summary and Plan for Finishing The 1:500k Geologic Map of Aeolis Dorsa, Mars: 2018 Planetary Geologic Mappers Annual Meeting, Abstract no. 7014.

Jaeger, W. L., Keszthelyi, L. P., Skinner, J. A., Milazzo, M. P., McEwen, A. S., Titus, T. N., Rosiek, M. R., Galuszka, D. M., Howington-Kraus, E., Kirk, R. L., and the HiRISE team, 2010, Emplacement of the youngest flood lava on Mars: A short, turbulent story: Icarus, v. 205, p. 230-243.

Jakosky, B. M., 1986, On the thermal properties of martian fines: Icarus, v. 66, p. 117–124.

Kahre, M. A., Murphy, J. R., and Haberle, R. M., 2006, Modeling the Martian dust cycle and surface dust reservoirs with the NASA Ames general circulation model: Journal of Geophysical Research, v. 111, E06008, doi:10.1029/2005JE002588.

Kerber, L., and Head, J. W., 2010, The age of the Medusae Fossae Formation: Evidence of Hesperian emplacement from crater morphology, stratigraphy, and ancient lava contacts: Icarus, v. 206, p. 669-684, doi:610.1016/j.icarus.2009.1010.1001.

Kerber, L., Head, J. W., Madeleine, J.-B., Forget, F., and Wilson, L., 2011, The dispersal of pyroclasts from Apollinaris Patera, Mars: Implications for the origin of the Medusae Fossae Formation: Icarus, v. 216, no. 1, p. 212-220.

Kerber, L., Head, J. W., Madeleine, J.-B., Forget, F., and Wilson, L., 2012, The dispersal of

pyroclasts from ancient explosive volcanoes on Mars: Implications for the friable layered deposits. Icarus, v. 219, p. 358-381.

Keszthelyi, L., McEwen, A. S., and Thordarson, T., 2000, Terrestrial analogs and thermal models for Martian flood lavas: Journal of Geophysical Research, v. 105, p. 15027-15049.

Keszthelyi, L., Thordarson, T., McEwen, A., Haack, H., Guilbaud, M. N., Self, S., and Rossi, M. J., 2004, Icelandic analogs to Martian flood lavas: Geochemistry, Geophysics, Geosystems, v. 5, doi:10.1029/2004GC000758.

Kite, E. S., Lucas, A., and Fassett, C. I., 2013, Pacing early Mars river activity: Embedded craters in the Aeolis Dorsa region imply river activity spanned $\sim\geq$ (1-20) Myr: Icarus, v. 225, p. 850-855.

Knauth, L. P., Burt, D. M., and Wohletz, K. H., 2005, Impact origin of sediments at the opportunity landing site on Mars: Nature, v. 438, p. 1123–1128, doi:10.1038/nature04383.

Kocurek, G., and Lancaster, N., 1999, Aeolian system sediment state: theory and Mojave Deser Kelso dune field example: Sedimentology, v. 46, p. 505-515.

Langevin, Y., Poulet, F., Bibring, J.-P., and Gondet, B., 2005, Sulfates in the north polar region of Mars detected by OMEGA/Mars Express: Science, v. 307, p. 1584–1586.

Lapotre, M. G. A., Ehlmann, B. L., Minson, S. E., Arvidson, R. E., Ayoub, F., Fraeman, A. A., Ewing, R. C., and Bridges, N. T., 2017, Compositional variations in sands of the Bagnold Dunes, Gale crater, Mars, from visible-shortwave infrared spectroscopy and comparison with ground truth from the Curiosity rover: Journal of Geophysical Research, v. 122, p. 2489-2509.

Leach, R., and Greeley, R., 1989, Saltation thresholds and entrainment of fine particles at Earth and Martian pressures: NASA Technological Memorandum, no. TM-102193, 43 p.

Lefort, A., Burr, D. M., Beyer, R. A., and Howard, A. D., 2012, Inverted fluvial features in the Aeolis-Zephyria Plana, western Medusae Fossae Formation, Mars: Evidence for

postformation modification: Journal of Geophysical Research: Planets, v. 117, no. E3, p. E03007.

Lenardic, A., Nimmo, F., and Moresi, L., 2004, Growth of the hemispheric dichotomy and the cessation of plate tectonics on Mars: Journal of Geophysical Research, v. 109, E02003, doi: 10.1029/2003JE002172.

Lorenz, R. D., and Zimbelman, J. R., 2014, Duneworlds: How Windblown Sand Shapes Planetary Landscapes. Springer-Verlag Berlin Heidelberg: London. 308 p.

Malin, M. C., 1977, Comparison of volcanic features of Elysium (Mars) and Tibesti (Earth): Geological Society of America Bulletin, v. 88, p. 908-919.

Malin, M. C., Calvin, W. M., Clancy, R. T., Edgett, K. S., Edwards, L., Haberle, R. M., James, P. B., Lee, S. W., Ravine, M. A., Thomas, P. C., Wolff, M. J., Bell, I. J. F., Cantor, B. A., and Caplinger, M. A., 2007, Context Camera Investigation on board the Mars Reconnaissance Orbiter: Journal of Geophysical Research E: Planets, v. 112, p. Article Number E05S04.

Mandt, K. E., de Silva, S. L., Zimbelman, J. R., and Crown, D. A., 2008, Origin of the Medusae Fossae Formation, Mars: Insights from a synoptic approach: J. Geophys. Res., v. 113, no. E12, p. E12011, doi:10.1029/2008je003076.

Mandt, K., de Silva, S., Zimbelman, J., and Wyrick, D., 2009, Distinct erosional progressions in the Medusae Fossae Formation, Mars, indicate contrasting environmental conditions: Icarus, v. 204, p. 471-477.

Mangold, N., Poulet, F., Mustard, J. F., Bibring, J.-P., Gondet, B., Langevin, Y., Ansan, V., Masson, Ph., Fassett, C., Head, J. W. III, Hoffmann, H., and Neukum, G., 2007, Mineralogy of the Nili Fossae region with OMEGA/Mars Express data: 2. Aquaous alteration of the crust: Journal of Geophysical Research, v. 112, E08S04, doi:10.1029/2006JE002835.

McEwen, A. S., Hansen, C. J., Delamere, W. A., Grant, J. A., Gulick, V. C., Herkenhoff, K. E.,

Keszthelyi, L., kirk, R. L., Mellon, M. T., Squyres, S. W., Thomas, N., Weitz, C. M., Eliason, E. M., Bergstrom, J. W., and Bridges, N. T., 2007, Mars reconnaissance orbiter's high resolution imaging science experiment (HiRISE): Journal of Geophysical Research E: Planets, v. 112, p. Article Number E05S02.

McEwen, A. S., Banks, M. E., Baugh, N., Becker, K., Boyd, A., Bergstrom, J. W., Beyer, R. A., Bortolini, E., Bridges, N. T., Byrne, S., Castalia, B., Chuang, F. C., Crumpler, L. S., Daubar, I., Davatzes, A. K., Deardorff, D. G., DeJong, A., Delamere, W. A., Dobrea, E. N., Dundas, C. M., Eliason, E. M., Espinoza, Y., Fennema, A., Fishbaugh, K. E., Forrester, T., Geissler, P. E., Grant, J. A., Griffes, J. L., Grotzinger, J. P., Gulick, V. J., Hansen, C. J., Herkenhoff, K. E., Heyd, R., Jaeger, W. L., Jones, D., Kanefsky, B., Keszthelyi, L., King, R., Kirk, R. L., Kolb, K. J., Lasco, J., Lefort, A., Leis, R., Lewis, K. W., Martinez-Alonso, S., Mattson, S., McArthur, G., Mellon, M. T., Metz, J. M., Milazzo, M. P., Milliken, R. E., Motazedian, T., Okubo, C. H., Ortiz, A., Philippoff, A. J., Plassmann, J., Polit, A., Russell, P. S., Schaller, C., Searls, M. L., Spriggs, T., Squyres, S. W., Tarr, S., Thomas, N., Thomson, B. J., Tornabene, L. L., Van Houten, C., Verba, C., Weitz, C. M., and Wray, J. J., 2010, The High Resolution Imaging Science Experiment (HiRISE) during MRO's Primary Science Phase (PSP): Icarus, v. 205, p. 2-37.

McGlynn, I. O., Fedo, C.M., and McSween, H. Y., 2011, Origin of basaltic soils at Gusev crater, Mars, by aeolian modification of impact-generated sediment: Journal of Geophysical Research, v. 116, doi:10.1029/2010JE003712.

McGlynn, I. O., Fedo, C. M., and McSween, H. Y., 2012, Soil mineralogy at the Mars Exploration Rover landing sites: An assessment of the competing roles of physical sorting and chemical weathering: Journal of Geophysical Research, v. 117, E01006, doi:10.1029/2011JE003861.

McKee, E. D., 1979, Introduction to a study of global sand seas, in A Study of Global Sand Seas, ed. E. D. McKee, U.S. Geological Survey Professional Paper, v. 1052, p. 3–17.

McLaughlin, D. B., 1954, Volcanism and aeolian deposition on Mars: Geological Society of

America Bulletin, v. 65, p. 715–718, doi:10.1130/0016-

7606(1954)65[715:VAADOM]2.0.CO;2.

McLaughlin, D. B., 1956a, The volcanic–aeolian hypothesis of martian features: Publications of

the Astronomical Society of the Pacific, v. 68, p. 211–218, doi:10.1086/126917.

McLaughlin, D. B., 1956b, New interpretation of the surface of Mars: Scientific Monthly, v. 83, p.

176–188.

Mellon, M. T., Jakosky, B. M., Kieffer, H. H., and Christensen, P. R., 2000, High-Resolution

Thermal Inertia Mapping from the Mars Global Surveyor Thermal Emission Spectrometer:

Icarus, v. 148, p. 437-455.

Melosh, H. J., 2011, Planetary Surface Processes: Cambridge University Press. 501 p.

Merrison, J. P., Gunnlaugsson, H. P., Nørnberg, P., Jensen, A. E., and Rasmussen, K. R.,

2007, Determination of the wind induced detachment threshold for granular material on

Mars using wind tunnel simulations: Icarus, v. 191, p. 568– 580.

Mouginis-Mark, P., J., 1985, Volcano/Ground Ice Interactions in Elysium Planitia, Mars: Icarus,

v. 64, p. 265-284.

Mouginis-Mark, P. J., 1993, The influence of oceans on Martian volcanism: 24th Lunar and

Planetary Science Conference, p. 1021-1022.

Mouginis-Mark, P.J., 2002, Prodigious ash deposits near the summit of Arsia Mons volcano,

Mars: Geophysical Research Letters, v. 29, no. 16, doi:10.1029/2002GL015296.

Mouginis-Mark, P. J., Wilson L., Head, J. W., Brown, S. H., Hall, J. L., and Sullivan, K. D., 1984,

Elysium Planitia, Mars: Regional geology, volcanology, and evidence for volcano ground-

ice interactions: Earth, Moon, Planets, v. 30, p. 149-173.

Murchie, S. L., Arvidson, R. E., Bedini, P., Beisser, K., Bibring, J. P., Bishop, J., Boldt, J. D.,

Choo, T. H., Clancy, R. T., Darlington, E. H., Dees Marais, D., Espiritu, R., Fasold, M. J.,

Fort, D., Green, R. N., Guinness, E., Hayes, J. R., Hash, C., Heffernan, K. J., Hemmler,

J., Heyler, G. A., Humm, D. C., Hutchison, J., Izenberg, N. R., Lee, R. E., Lees, J. J., Lohr, D. A., Malaret, E. R., Martin, T., Morris, R. V., Mustard, J. F., Rhodes, E. A., Robinson, M. S., Roush, T. L., Schaefer, E. D., Seagrave, G. G., Silverglate, P. R., Slavney, S., Smith, M. F., Strohbehn, K., Taylor, H. W., Thompson, P. L., and Tossman, B. E., 2004, CRISM (Compact Reconnaissance Imaging Spectrometer for Mars) on MRO (Mars Reconnaissance Orbiter): Proceedings of SPIE, v. 5660, doi: 10.1117/12.578976.

Ohja, L., and Karunatillake, S., 2017, Volcanic Origin of Medusae Fossae Formation from Gravity and Topography Data: 48th Lunar and Planetary Science Conference, Abstract no. 2475.

Ohja, L., Lewis, K., and Karunatillake, S., 2017, The Density of the Medusae Fossae Formation: Implications for its Composition, Origin, and Importance in Martian History: Geological Society of America Abstracts with Programs, v. 49, no. 6.

Parker, T. J., 1991, A comparison of the Martian Medusae Fossae Formation with terrestrial carbonate platforms: 22nd Lunar and Planetary Science Conference, p. 1029– 1030.

Peabody, F. E., 1947, Current crescents in the Triassic Moenkopi Formation: Journal of Sedimentary

 Petrology, v. 17, p. 73–76.

Plescia, J., 1990, Recent flood lavas in the Elysium regions of Mars: Icarus, v. 88, p. 465–490. doi:10.1016/0019-1035(90)90095-Q.

Putzig, N. E., and Mellon, M. T., 2007, Apparent thermal inertia and the surface heterogeneity of Mars: Icarus, v. 191, p. 68-94.

Reffet, E., du Pont, S. C., Hersen, P., and Douady, S., 2010, Formation and stability of transverse and longitudinal sand dunes: Geology, v. 38, p. 491-494.

Roberts, G. P., Crawford, I. A., Peacock, D., Vetterlein, J., Parfitt, E., and Bishop, L, 2007,

Possible evidence for on-going volcanism on Mars as suggested by thin, elliptical sheets of low-albedo particulate material around pits and fissures close to Cerberus Fossae: Earth, Moon, Planets, v. 101, p. 1-16.

Roberts, G. P., Matthews, B., Bristow, C., Guerrieri, L., and Vetterlein, J., 2012, Possible evidence of paleomarsquakes from fallen boulder populations, Cerberus Fossae, Mars: Journal of Geophysical Research: Planets, v. 117, no. E2, p. E02009, doi:10.1029/2011je003816.

Rubin, D. M., and Ikeda, H., 1990, Flume experiments on the alignment of transverse, oblique, and longitudinal dunes in directionally varying flows: Sedimentology, v. 37, p. 673-684.

Sagan, C., 1973, Sandstorms and Eolian Erosion on Mars: Journal of Geophysical Research, v. 78, p. 4155-4161.

Sakimoto, S. E. H., Frey, H. V., Garvin, J. B., and Roark, J. H., 1999, Topography, roughness, layering, and slope properties of the Medusae Fossae Formation from Mars Orbiter Laser Altimeter (MOLA) and Mars Orbiter Camera (MOC) data: Journal of Geophysical Research-Planets, v. 104, no. E10, p. 24141-24154.

Schultz, P. H., and Lutz, A. B., 1988, Polar wandering of Mars: Icarus, v. 73, p. 91–141.

Scott, D. H., and Tanaka, K. L., 1982, Ignimbrites of Amazonis Planitia Region, Mars: Journal of Geophysical Research, v. 87, p. 1179-1190.

Scott, D., and Tanaka, K., 1986, Geologic map of the western equatorial region of Mars: U. S. Geological Survey, map I-1802a.

Silvestro, S., Vaz, D. A., Ewing, R. C., Rossi, A. P., Fenton, L. K., Michaels, T. I., Flahaut, J., and Geissler, P. E., 2013, Pervasive aeolian activity along rover Curiosity's traverse in Gale Crater, Mars: Geology, v. 41, p. 483-486.

Spiga, A., 2011, Elements of comparison between Martian and terrestrial mesoscale meteorological phenomena: Katabatic winds and boundary layer convection: Planetary and Space Science, v. 59, p. 915-922.

Sullivan, R., Fike, D., Golombek, M., Greeley, R., Grotzinger, J., Herkenhoff, K., Jerolmack, D., Malin, M., Ming, D., Soderblom, L. A., Squyres, S. W., Thompson, S., Watters, W. A., Weitz, C. M., Yen, A., Banfield, D., Bell, I. J. F., and Calvin, W., 2005, Aeolian processes at the Mars Exploration Rover Meridiani Planum landing site: Nature, v. 436, no. 7047, p. 58-61.

Tanaka, K. L., 1986, The stratigraphy of Mars: Journal Geophysical Research, v. 91, p. E139-E158.

Tanaka, K. L., Skinner, J. A., & Hare, T. M., 2005, Geologic map of the northern plains of Mars: U.S. Geologic Survey Scientifgic Investigations Map 2888.

Tanaka, K. L., 2006, Mars' North Polar Gypsum: Possible Origin Related to Early Amazonian Magmatism at Alba Patera and Aeolian Mining: Fourth International Conference on Mars Polar Science and Exploration, Abstract 8024.

Thomson, B. J., Bridges, N. T., and Greeley, R., 2007, Rock abrasion features in the Columbia Hills, Mars: Journal of Geophysical Research, v. 113, E08010, doi:10.1029/2007JE003018.

Tirsch, D., Jaumann, R., Pacifici, A., and Poulet, F., 2011, Dark aeolian sediments in Martian craters: Composition and sources: Journal of Geophysical Research, v. 116, E03002, doi: 10.1029/2009JE003562.

Tran, L. T., 2016, An interactive method to select a set of sustainable urban development indicators: Ecological Indicators, v. 61, p. 418-427.

Tsoar, H., 1983, Wind tunnel modeling of echo and climbing dunes, *in* Eolian Sediments and Processes, Developments in Sedimentology, edited by M. E. Brookfield and T. S. Ahlbrandt, pp. 247–259, Elsevier, Amsterdam, doi:10.1016/S0070-4571(08)70798-2.

Tsoar, H., 2001, Types of Aeolian Sand Dunes and Their Formation. *In:* Geomorophological Fluid Mechanics, ed. Balmforth, N. J., and Provenzale, A.. Springer-Verlag Verlin Heidelberg. p. 403-429.

Vaucher, J., Baratoux, D., Mangold, N., Pinet, P., Kurita, K., and Grégoire, M., 2009, The

    volcanic history of central Elysium Planitia: Implications for martian magmatism: Icarus, v.

    204, p. 418-442.

Ward, A. W., 1979. Yardangs on Mars: Evidence of Recent Wind Erosion. Journal of

    Geophysical Research, v. 84, p. 8147-8166.

Williams, R. M. E., Irwin, R. P. III, Burr, D. M., Harrison, T., and McClelland, P., 2013, Variability

    in martian sinuous ridge form: Case study of Aeolis Serpens in the Aeolis Dorsa, Mars,

    and insight from the Mirackina paleoriver, South Australia: Icarus, v. 225, p. 308-324.

Wilson, L., and Head, J. W. III, 1994, Mars: Review and analysis of volcanic eruption theory and

    relationships to observed landforms: Reviews of Geophysics, v. 32, p. 221-263.

Zimbelman, J. R., and Griffin, L. J., 2010, HiRISE images of yardangs and sinuous ridges in the

Zimbelman, J. R., Johnston, A. K., and Lovett, C. G., 1996, Geologic map of the Medusae

    Fossae Formation within MTM quadrangle 05142 on Mars: Geological Society of America

    Abstracts with Programs, no. A128.

Zimbelman, J. R., and Scheidt, S. P., 2012, Hesperian Age for Western Medusae Fossae

    Formation, Mars: Science, v. 336, no. 6089, p. 1683, doi:10.1126/science.1221094.

Zimbelman, J. R., and Williams, S. H., 2002, Geochemical indicators of separate sources for

    eolian sands in the eastern Mojave Desert, California, and western Arizona: Geological

    Society of America Bulletin, v. 114, p. 490-496.

APPENDIX

Table 1: Important aeolian features

Terrestrial and Martian examples of aeolian morphologies pertinent to Aeolis Dorsa, Mars. White arrows indicate inferred winds. (a) Transverse dunes in the Caraveli Province, Peru. Image credit Amelia Carolina Sparavigna (URL: http://philica.com/display_article.php?article_id=447). (b) Transverse dunes on Zephyria Planum, Mars. HiRISE image ESP_026897_1755. Image credit NASA/JPL/Univ. of Arizona. (c) Climbing dune in the Mojave Desert, CA, USA. Image: Google Earth. (d) CTX image P12_005570_1650_XN_155057W showing falling dunes in Coprates Chasma, Mars. (e) Echo dunes near Tuba City, Arizona, USA. Image courtesy Google Earth. (f) HiRISE image ESP_017173_1715 showing an echo dune in Ganges Chasma, Mars. Image credit NASA/JPL/Univ. of Arizona. (g) Cars driving over a sand sheet in the Sahara Desert, Mauritania. Image credit Chris Scott (URL: https://sahara-overland.com/author/chrisamh6/). (h) Dunes grading into sand sheet in Ganges Chasma, Mars. MOC image S0501628. Image credit NASA/JPL/Malin Space Science Systems. (i) Scours in Qaidam Desert, China. Image: GoogleEarth_2010_DigitalGlobe _2004—03-01_1010010002C015. From Bishop (2011). (j) HiRISE image ESP_025262_1745 showing scour marks on eastern Aeolis Planum, Mars. Image credit NASA/JPL/Univ. of Arizona.
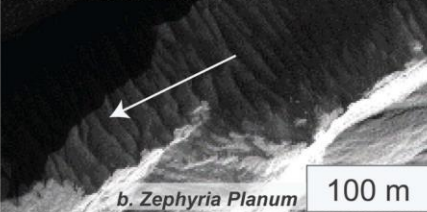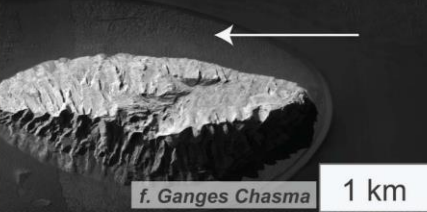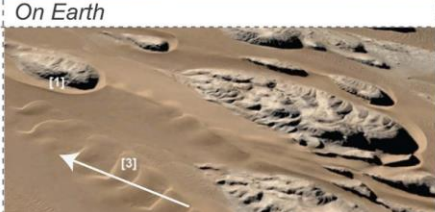
IMPORTANT AEOLIAN FEATURES: TERRESTRIAL AND MARTIAN EXAMPLES

Depositional features	On Earth	On Mars
Transverse dune: Ridge, with asymmetric slopes; longer slope on upwind side of dune	100 m — a. Caraveli Province, Peru	b. Zephyria Planum — 100 m
Climbing and falling dune: Deposits moving up or down >10° slopes. Unanchored, so limited by angle of repose.	60 m — c. Mojave Desert, USA	d. Coprates Chasma — 800 m
Echo dune: Anchored dune with slipface parallel to high-standing bedrock. Often co-occurring with scoured moats.	100 m — e. Tuba City, AZ, USA	f. Ganges Chasma — 1 km
Sand sheet: Smooth, low-relief deposit of loose sediment. Relatively featureless: lacks anchored duneforms, but may have ripples or other transient aeolian features superimposed on surface.	g. Sahara Desert, Mauritania	h. Ganges Chasma — 1.5 km

Erosional features	On Earth	On Mars
Scour mark: Crescent-shaped moat; form on upwind sides of topographic obstacles	200 m — i. Qaidam Desert, China	j. Aeolis Planum — 300 m

Table 2: Textual description of sand deposit characteristics
Table with descriptions of each category of sand deposits mapped in this study. Examples shown in Figure 4.1.

Unit name	General description (1:100k scale)	Additional details (1:24k scale)
Dark-toned sand in yardang troughs	Low-albedo, discontinuous deposits of dark material. Deposit surfaces appear smooth at larger scales (~1:100,000 and above). Deposits are concentrated in narrow bedrock troughs a) on Aeolis Planum, b) on and immediately adjacent to Zephyria Planum, and c) in the southern depression. Deposits lie suprajacent to underlying bedrock.	At smaller scales (~1:24,000 and below), small-scale ripples [5-20 m long with ~3-5 m spacing] or transverse dunes occur on some deposit surfaces. Ripples occur throughout the AD region; dunes appear to be confined to two locations on Zephyria Planum. Ripples and dune forms are oriented normal to long axes of bedrock ridges and troughs. Dark, lower-relief tails extending out from bedrock outcrops are present in the southern depression and on Aeolis Planum. Tails, when present, are parallel- to- subparallel with long axes of bedrock ridges and troughs. On Zephyria Planum, 10- to- 100-m long transverse dunes occur in two locations. Deposits co-occur with locally enhanced thermal signatures in nighttime IR.
Dark-toned sand sheet	Low-albedo, discontinuous, smooth surficial deposits occurring over flat surfaces, mainly on Aeolis and Zephyria Plana, and within the southern depression [other term/description?]. Smooth surfaces, +/- forming scour marks around bedrock obstacles.	Extremely smooth surfaces, sometimes with ~1-10-m-scale scour marks around bedrock obstacles. Deposits co-occur with locally enhanced thermal signatures in nighttime IR.
Light-toned sand in yardang troughs	Relatively high-albedo deposits concentrated in bedrock troughs. Characterized by smooth surfaces, +/- rounded tops. When deposited around a bedrock obstacle, forms moat separating depositional material from bedrock.	Occurring within yardangs and other inter-bedrock troughs, this unit is characterized by smooth surfaces that are sometimes mound-shaped. These deposits sometimes grade into dark-colored mantling material.
Light-toned sand sheet	Relatively high-albedo deposits found on Aeolis and Zephyria plana. Smooth deposit surfaces, with or without 10-40-meter-long wind ripples (with widths of ~2 m or less). Identified by smooth surfaces with the presence of scoured moats around obstacles.	Extremely smooth, high-albedo surfaces. Identified by the presence of scour marks and moats around bedrock obstacles [which provide evidence of a substantive surficial deposit superjacent to bedrock].

Table 3: Scour mark distributions and orientation overview

Table showing measurements of scour mark orientations and inferred directions from which wind was blowing. Top set of measurements from all 621 mapped scour marks in Aeolis Dorsa. Bottom set of measurements (mapped by R. Jacobsen) from 62 randomized scour marks.

A. Boyd [full] measurements:					
	Northeast Zephyria Planum	**Northern Aeolis Dorsa**	**Southern Depression**	**Central Zephyria Planum**	**Aeolis Planum**
Average inferred winds (°):	123°	246°	325°	341°	318°
Standard deviation:	75°	34°	93°	11°	30°
First quartile (25%):	93°	235°	286°	334°	302°
Median orientation:	117°	246°	324°	341°	321°
Third quartile (75%):	140°	296°	343°	342°	336°
R. Jacobsen [error] measurements:					
	Northeast Zephyria Planum	**Northern Aeolis Dorsa**	**Southern Depression**	**Central Zephyria Planum**	**Aeolis Planum**
Average inferred winds (°):	122°	287°	N/A	N/A	329°
Standard deviation:	28°	77°	N/A	N/A	43°
First quartile (25%):	109°	N/A	N/A	N/A	306°
Median orientation:	120°	N/A	N/A	N/A	342°
Third quartile (75%):	134°	N/A	N/A	N/A	353°

Table 4: Relationships between clusters of sand and scours with working hypotheses

Table showing agreement of clusters of sand and scour marks with predicted outcomes for all working hypotheses. Also shown are sand cluster areas and numbers of scour marks in clusters.

Cluster	Elysium Mons Match	Elysium Mons Area (km²)	Cerberus Plains Match	Cerberus Plains Area (km²)	Southern Highlands Match	Southern Highlands Area (km²)	Medusae Fossae Fm. Match	Medusae Fossae Fm. Area (km²)
Sand deposits								
1					x	647,763		
2					x	850,247		
3					x	41,370		
4							x	111,394
5								
6							x	5,681
7								
8							x	804,476
9							x	228,881
10							x	741,298
11			x	61,854				
12							x	4,181
13							x	1,049
14								
15							x	8,567
16			x	166,478			x	166,478
17	x	34,429					x	34,429
18							x	1,161
Totals:	1 match	34,429	2 matches	228,331	3 matches	1,539,381	11 matches	2,118,648

Scour marks	Match	No. scours	Match	No. scours	Match	No. scours	Match	No. scours
N. Aeolis Dorsa								
NE Zeph. Planum			x	69			x	69
C. Zeph. Planum	x	4						
Aeolis Planum	x	513					x	513
S. Depression							x	13
Totals:	2 matches	517 scours	1 match	69 scours	0 matches	0 scours	3 matches	595 scours

Table 5: Sand distribution over geologic units

Table showing dark- and light-toned sand distribution over geologic units of Aeolis Dorsa. Units derived from upcoming map of Aeolis Dorsa (MDAP, PI: Burr, D. M.). Note: only units with overlying sand are listed. For complete list of units in Aeolis Dorsa, see Jacobsen et al. (2018a, 2018b).

Geologic unit*	Dark sand (m^2)	Light-toned sand (m^2)	Total sand (m^2)	Sand in each geologic unit	Percent of all sand in AD
Aeolis Dorsa group					
Had$_1$	10,968.0	534.3	11,502.3	3.8%	0.3%
Had$_2$	334.3	0.0	334.3	0.1%	0.0%
Had$_u$	76,666.8	218,214.8	294,881.6	96.1%	8.4%
Combined…..	87,969.1	218,749.1	306,718.2	1.0	0.1
Medusae Fossae Fm.					
Hp$_1$	133,020.7	231,320.5	364,341.2	23.0%	10.4%
Ap$_2$	541,082.6	3,450.6	544,533.3	34.4%	15.6%
AHp$_u$	115,560.3	559,077.7	674,638.0	42.6%	19.3%
Combined…..	789,663.7	793,848.9	1,583,512.5		45.4%
Transition units					
td	1,251,633.5	226,904.0	1,478,537.5	93.2%	42.4%
tt	14,097.3	0.0	14,097.3	0.9%	0.4%
tu	63,868.9	29,887.0	93,755.9	5.9%	2.7%
Combined…..	1,329,599.7	256,791.0	1,586,390.8		45.4%
Southern highlands					
HNhm	4,525.5	6,843.4	11,369.0	81.0%	0.3%
Ahu	2,671.4	0.0	2,671.4	19.0%	0.1%
Combined…..	7,196.9	6,843.4	14,040.3		0.4%
Totals…..	3,628,756.4		3,490,661.8		

* unit distinctions and descriptions via Jacobsen et al., 2018
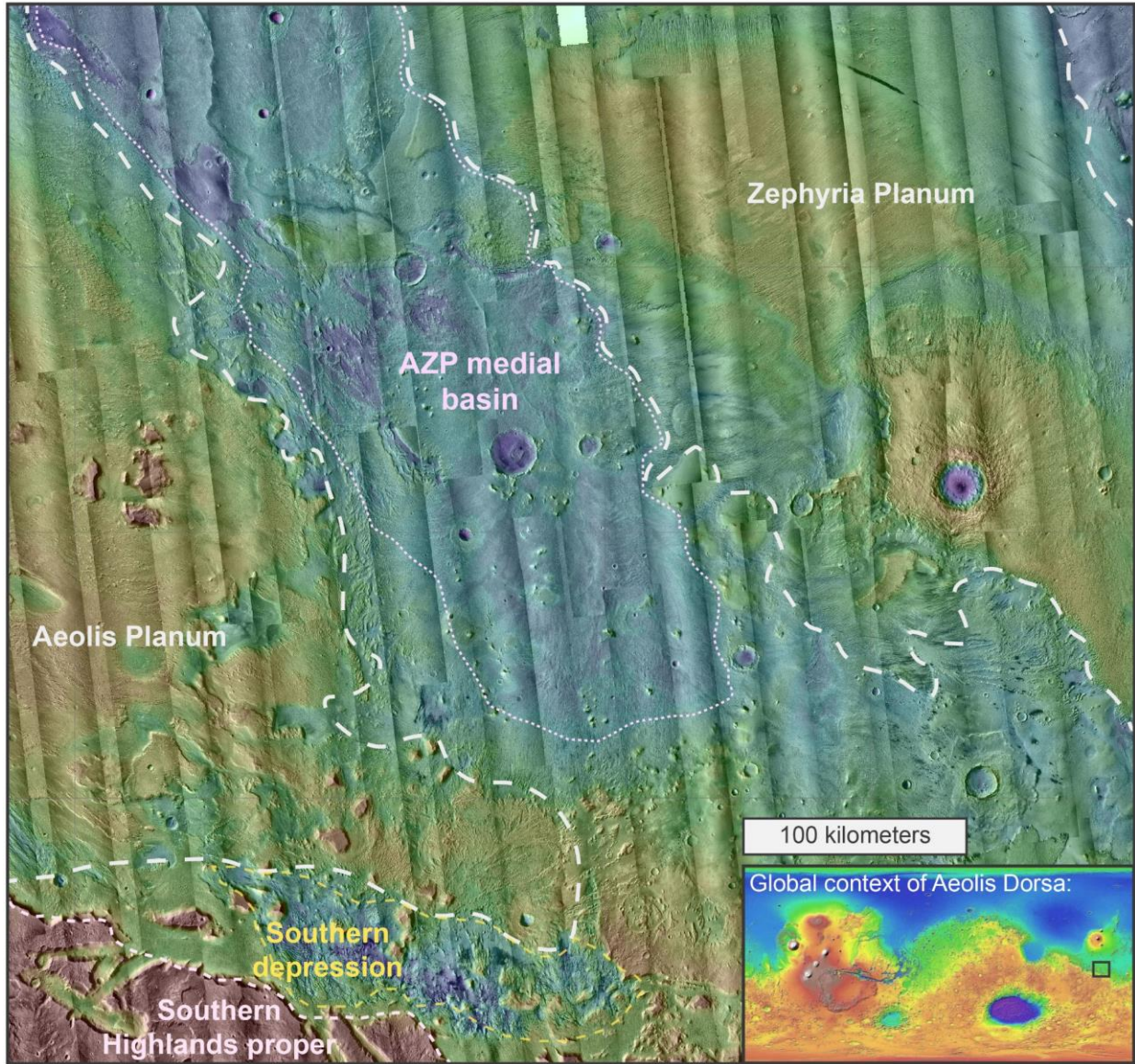
Figure 1.1. Mars Orbiter Laser Altimeter (MOLA) digital elevation map (DEM) overlain on Mars Context Camera (CTX) image mosaic base map of the study area. Aeolis and Zephyria Plana, representing the majority of the MFF bedrock exposure in the region, are outlined in dashed white lines. Global context of the study area is shown in the black box in inset MOLA global DEM. Sources: MOLA team/ CTX team/ USGS.
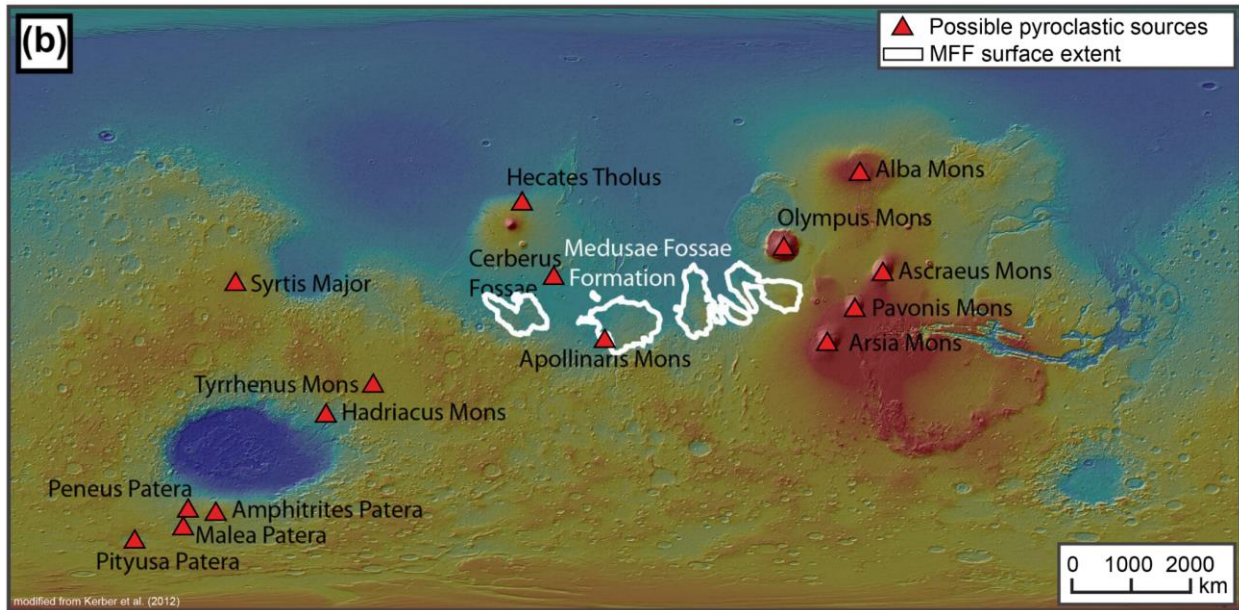
Figure 2.1. Global extent of the Medusae Fossae Formation (MFF), outlined in white. From Kerber et al. (2012).
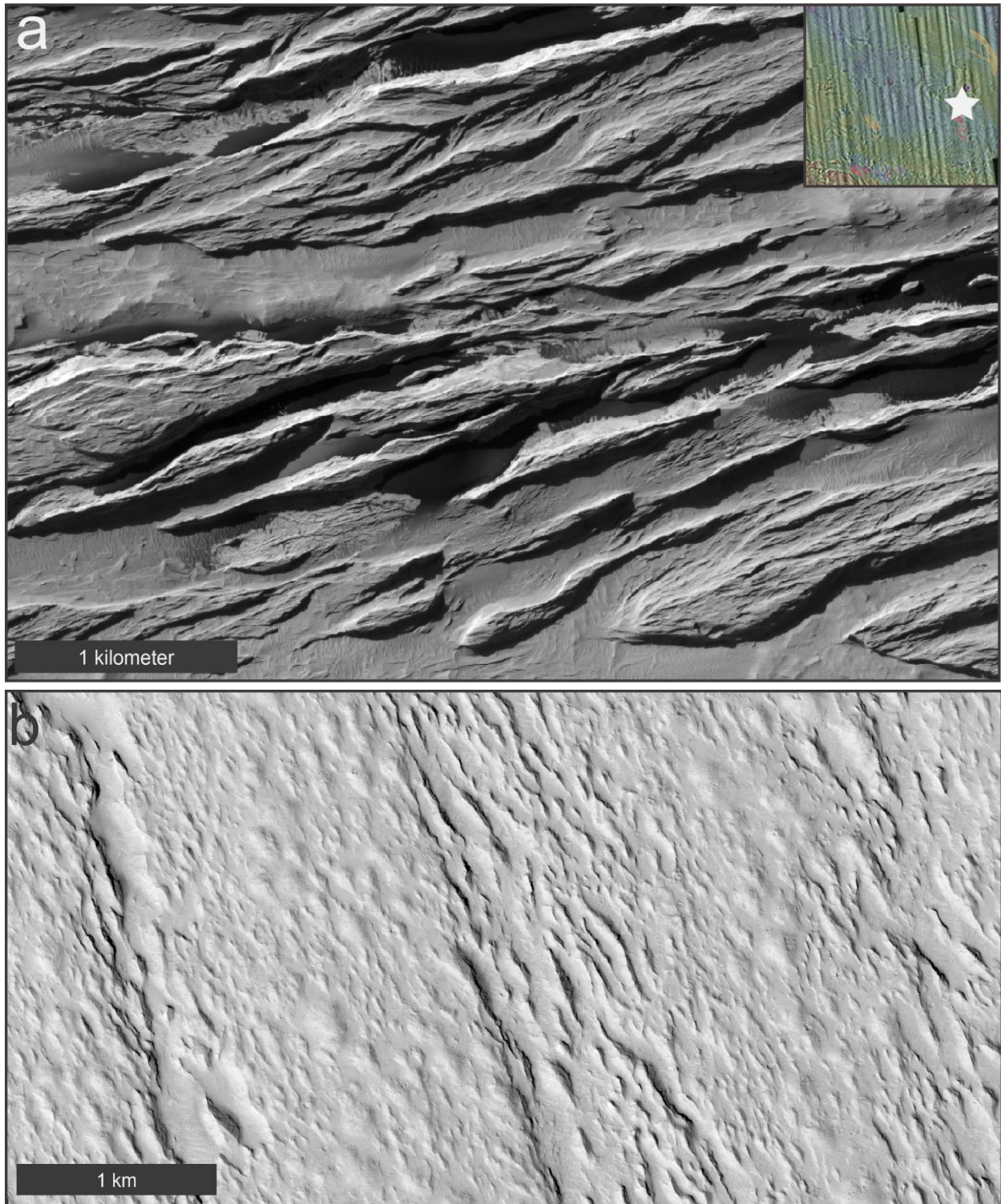
Figure 2.2. Yardangs of the Medusae Fossae Formation (MFF). A) Yardangs within the MFF on Zephyria Planum, punctuated by dark sand, in this study area. B) Yardangs in MFF near Apollinaris Patera, Mars (HiRISE image ESP_016611_1680). Both images courtesy NASA/JPL/University of Arizona.
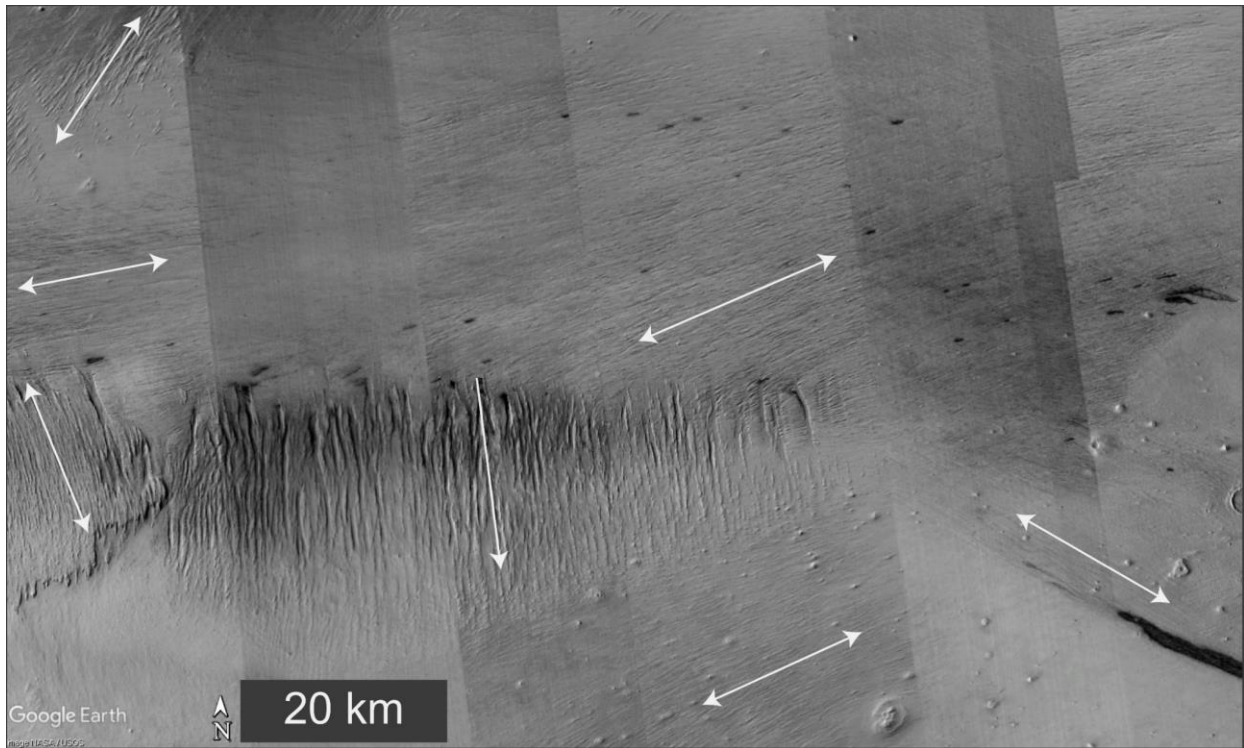
Figure 2.3. Yardang field orientations within the Medusae Fossae Formation in northern Aeolis Dorsa. White arrows represent orientation of yardangs in different fields: unidirectional arrows represent wind directions that formed yardang fields; bidirectional arrows indicative of uncertainty in direction of winds that shaped yardangs. Image courtesy Google Earth/NASA.
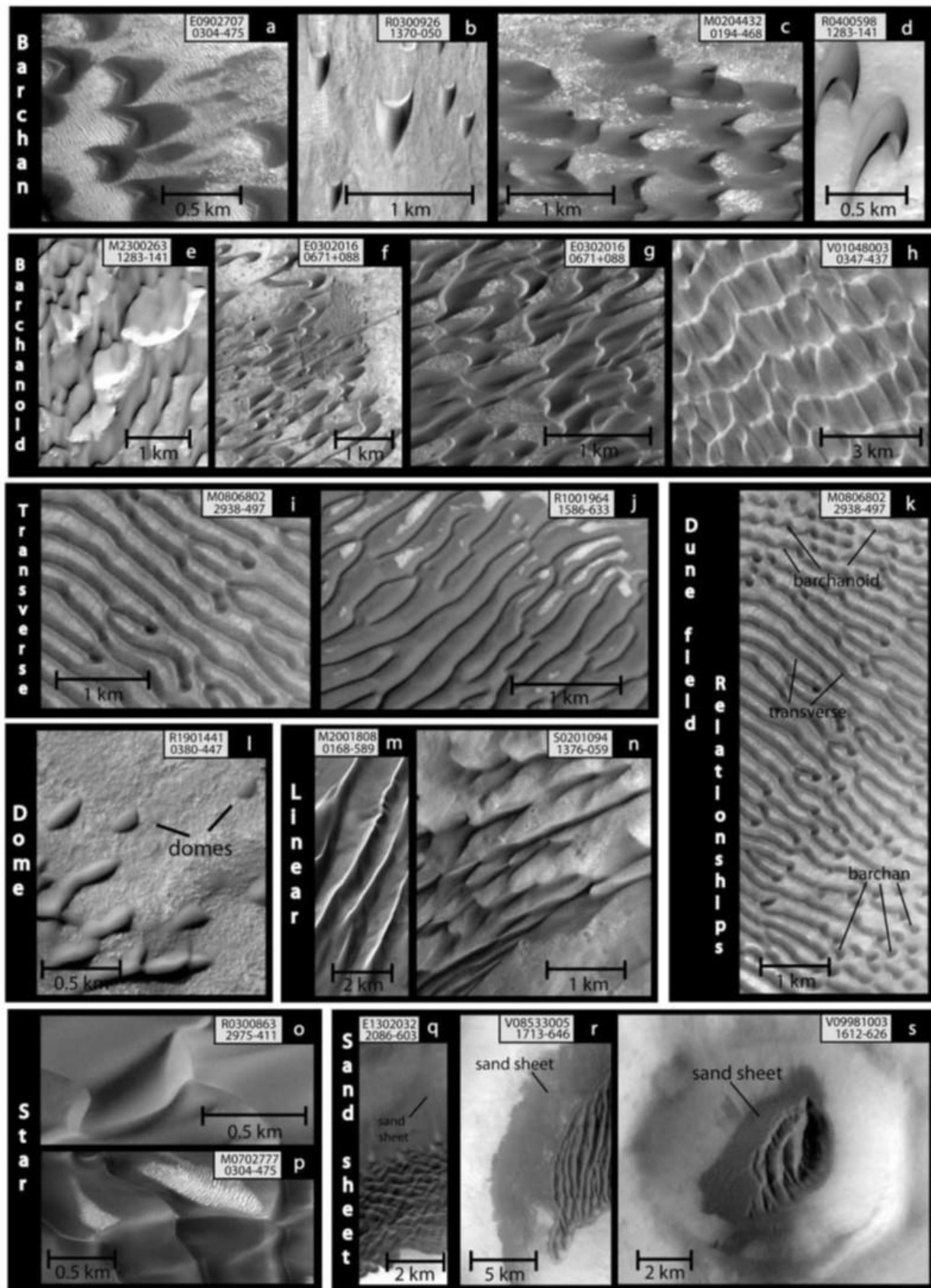
Figure 2.4. Figure from Hayward et al. (2007) showing various dune forms found on Mars. All dune forms notated.
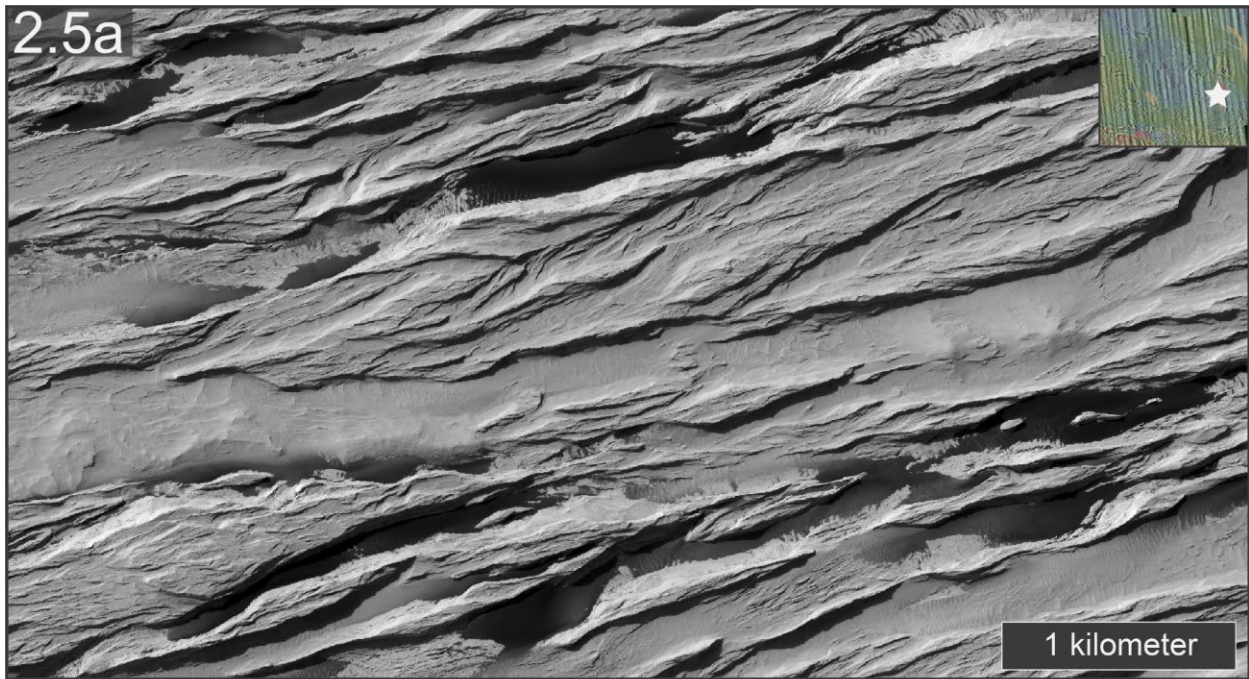
Figure 2.5. Types of dark sand deposits in Aeolis Dorsa. (a) HiRISE image ESP_044000_1750 showing dark sand deposits in inter-yardang troughs. Image credit: NASA/JPL/Univ. of Arizona. (b) Google Earth CTX mosaic showing sand sheet in southern Aeolis Dorsa.
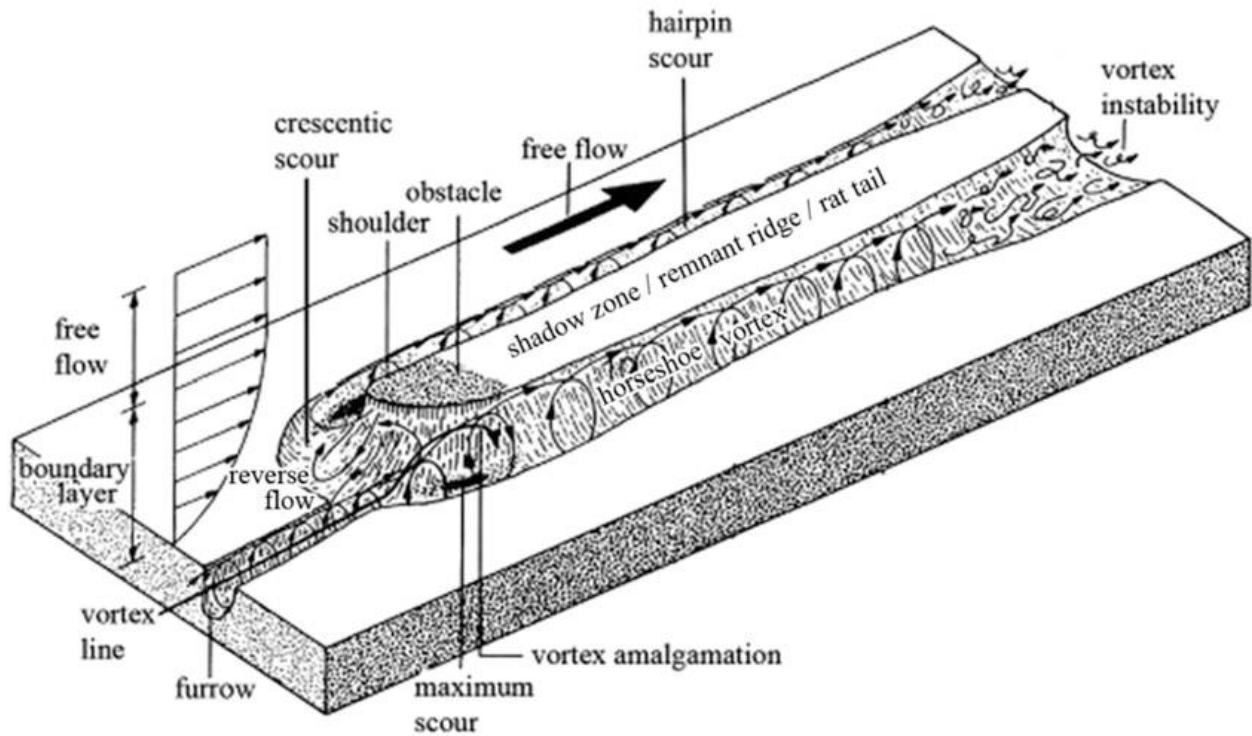
Figure 2.6. Diagram showing wind movement forming non-depositional scour marks (i.e., scours with no echo dune upwind of moat). From Shaw et al., 2008.
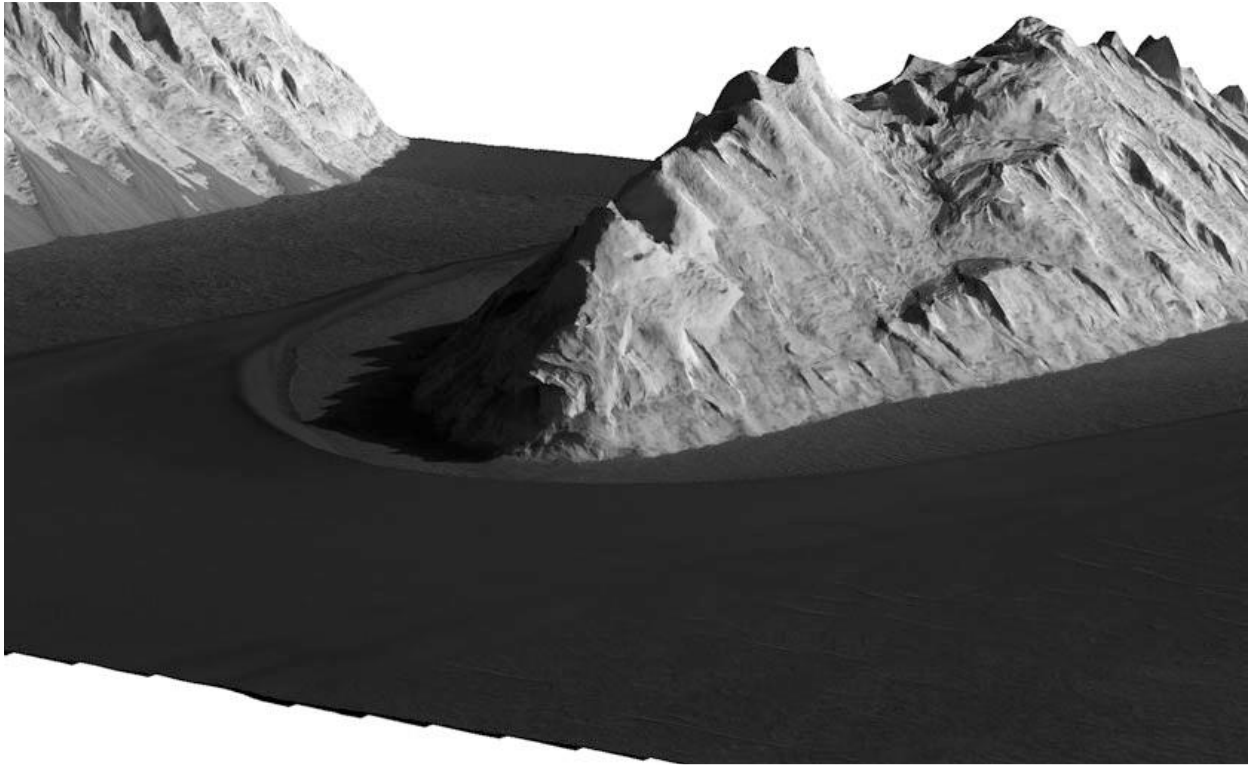
Figure 2.7. Echo dune preceding scour mark moat near Ganges Chasma, Valles Marineris, Mars. From Chojnacki (2014a). Image credit: NASA/JPL/University of Arizona
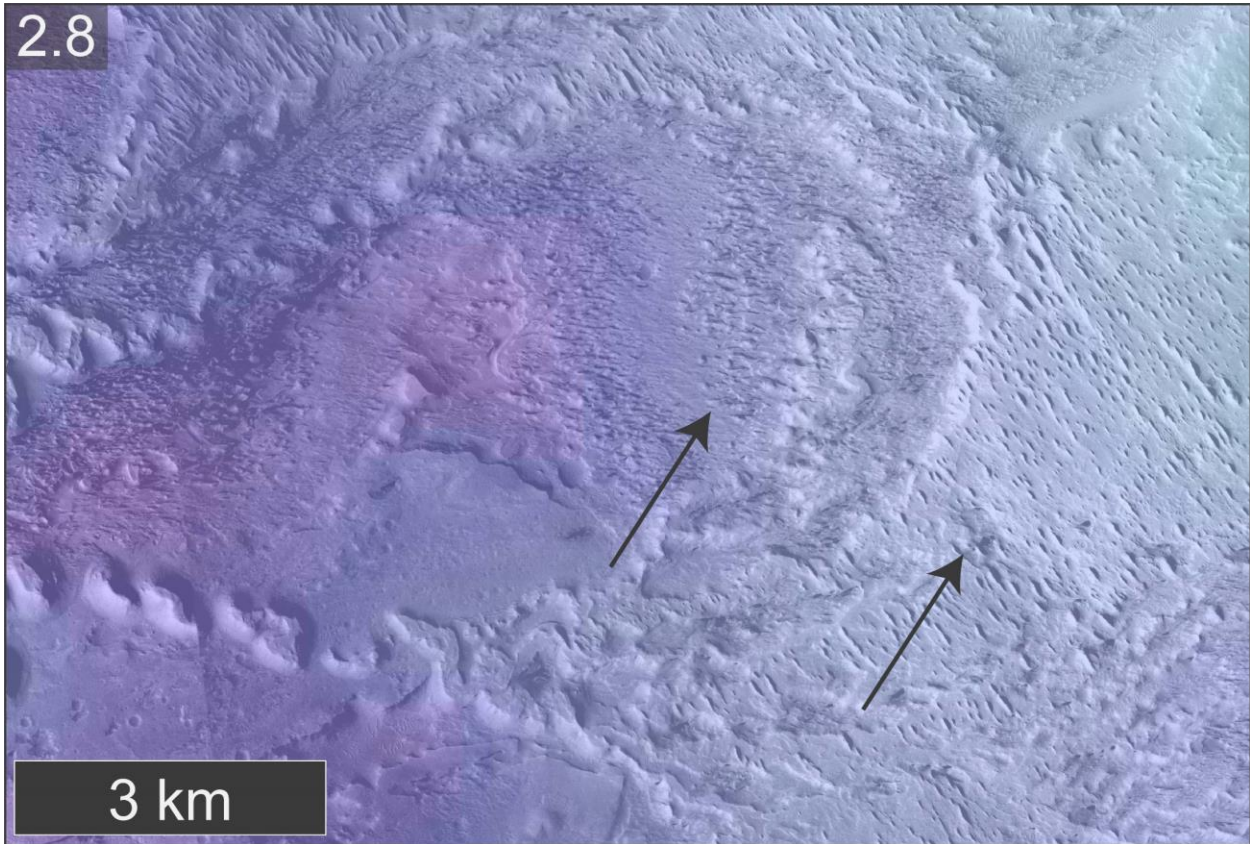
Figure 2.8. MOLA elevation overlaid on HiRISE image PSP_001448_1735, which shows two yardang fields within the Medusae Fossae Formation on Aeolis Planum. Yardangs trending NW-SE are superposed on smaller, poorly-developed yardangs trending E-W. Arrows demarcate example yardangs.
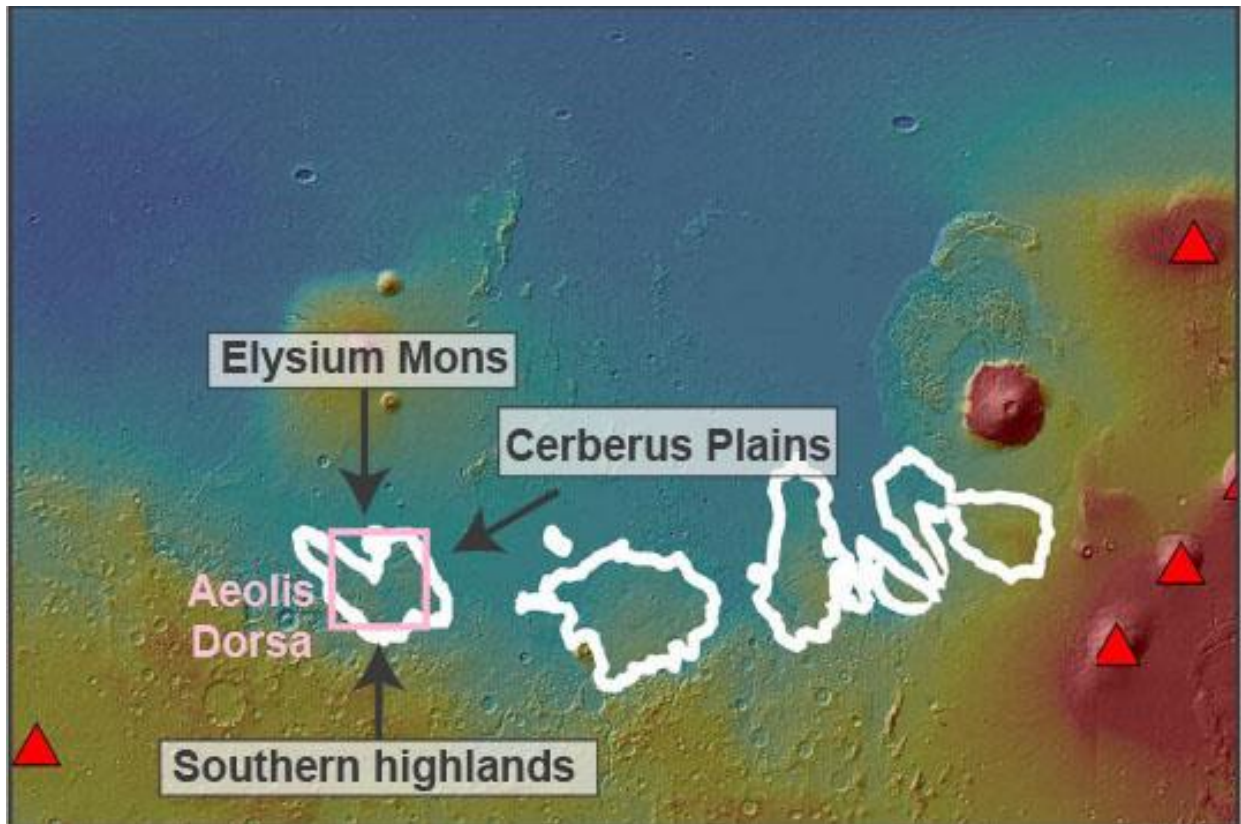
Figure 2.9. Geographic regions surrounding Aeolis Dorsa (AD outlined in pink). These regions constitute potential external sources of sand in Aeolis Dorsa. Numbers correspond to numbered hypotheses in section 3. MFF global extent outlined in white. Modified from Kerber et al. (2012).

Figure 2.10. Images showing similarities between southern highlands materials and bedrock blocks in Aeolis Dorsa inferred to be remnant southern highlands material. a) Regional context showing probable remnant southern highlands blocks (stars) and southern highlands to the south. b) Southern highlands bedrock. Note coarse layering and abundant bright talus slopes. c) Bedrock in the southern depression of the Aeolis Dorsa region inferred to consist of remnant southern highlands material. Similarly coarse layering and abundant bright talus slopes are visible in both images. Image credits: NASA/JPL/Univ. of Arizona.

a inferred Southern Highlands remnants

Southern Highlands proper

b Coarse layering in Southern Highlands

500 meters

c coarse layering in hypothesized Southern Highlands remnants

200 meters
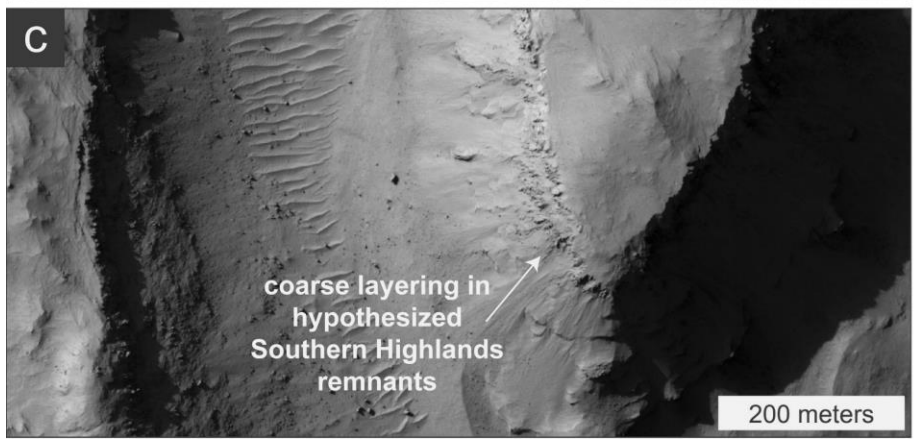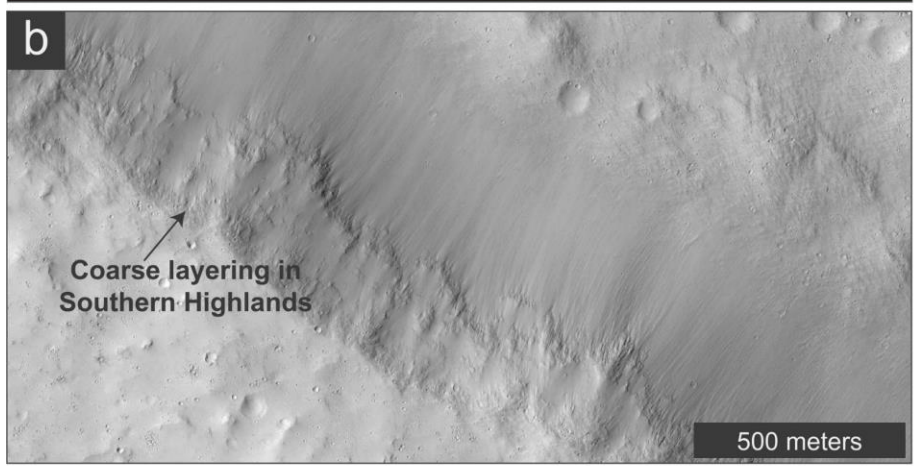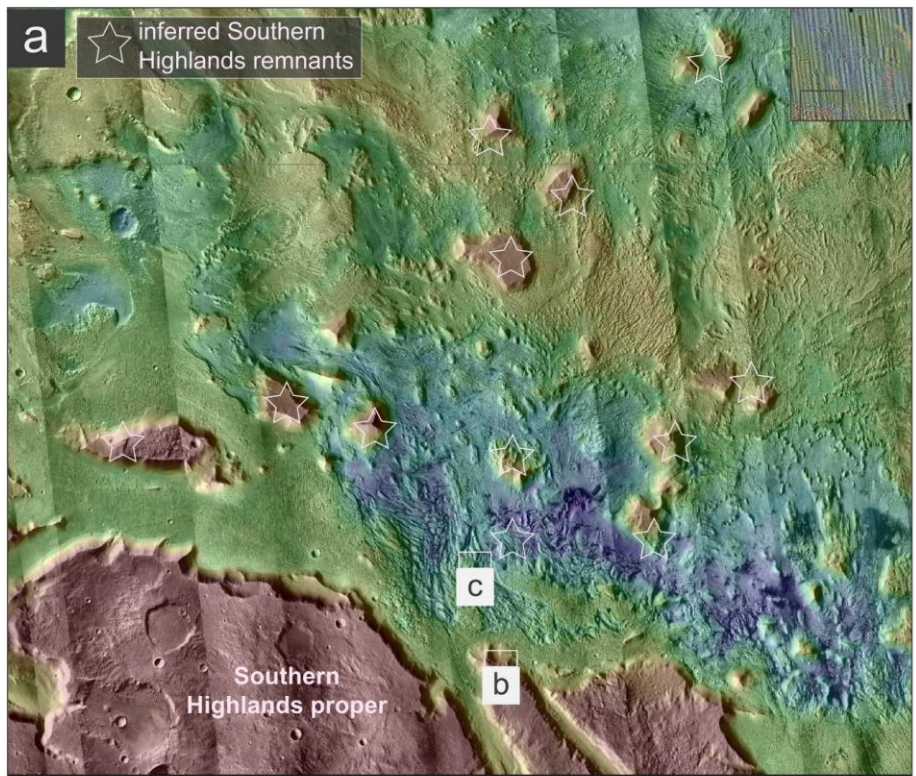
Figure 2.10, continued
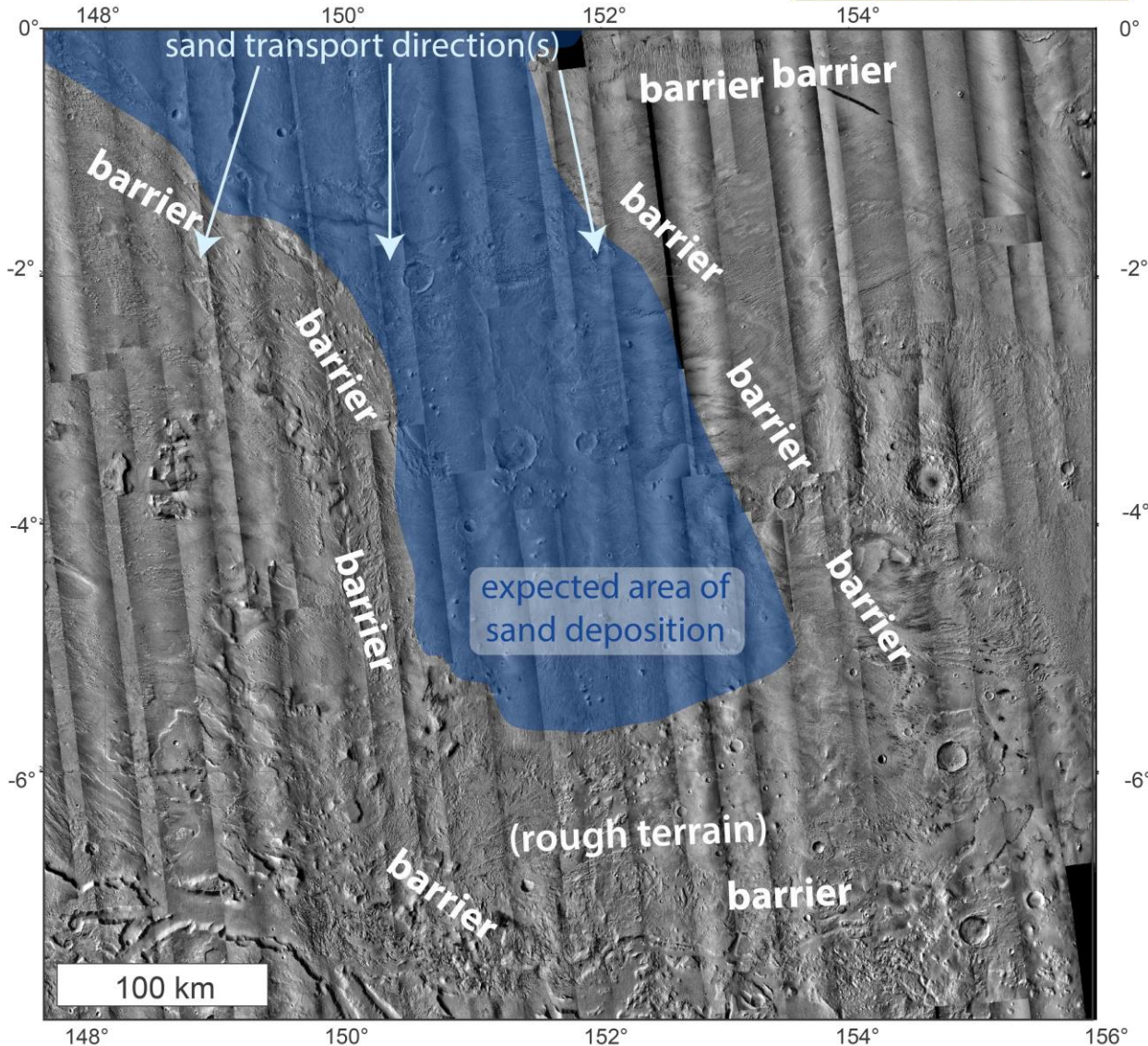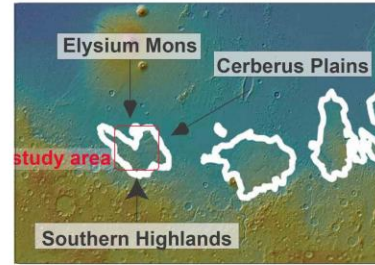
Figure 3.1. Expected sand distribution (color overlays) and inferred transport wind directions, (arrows) for sand sourced from Elysium Mons, located to the north of Aeolis Dorsa (see inset). 'Barrier' denotes highstanding obstacle likely to prevent sand transport.
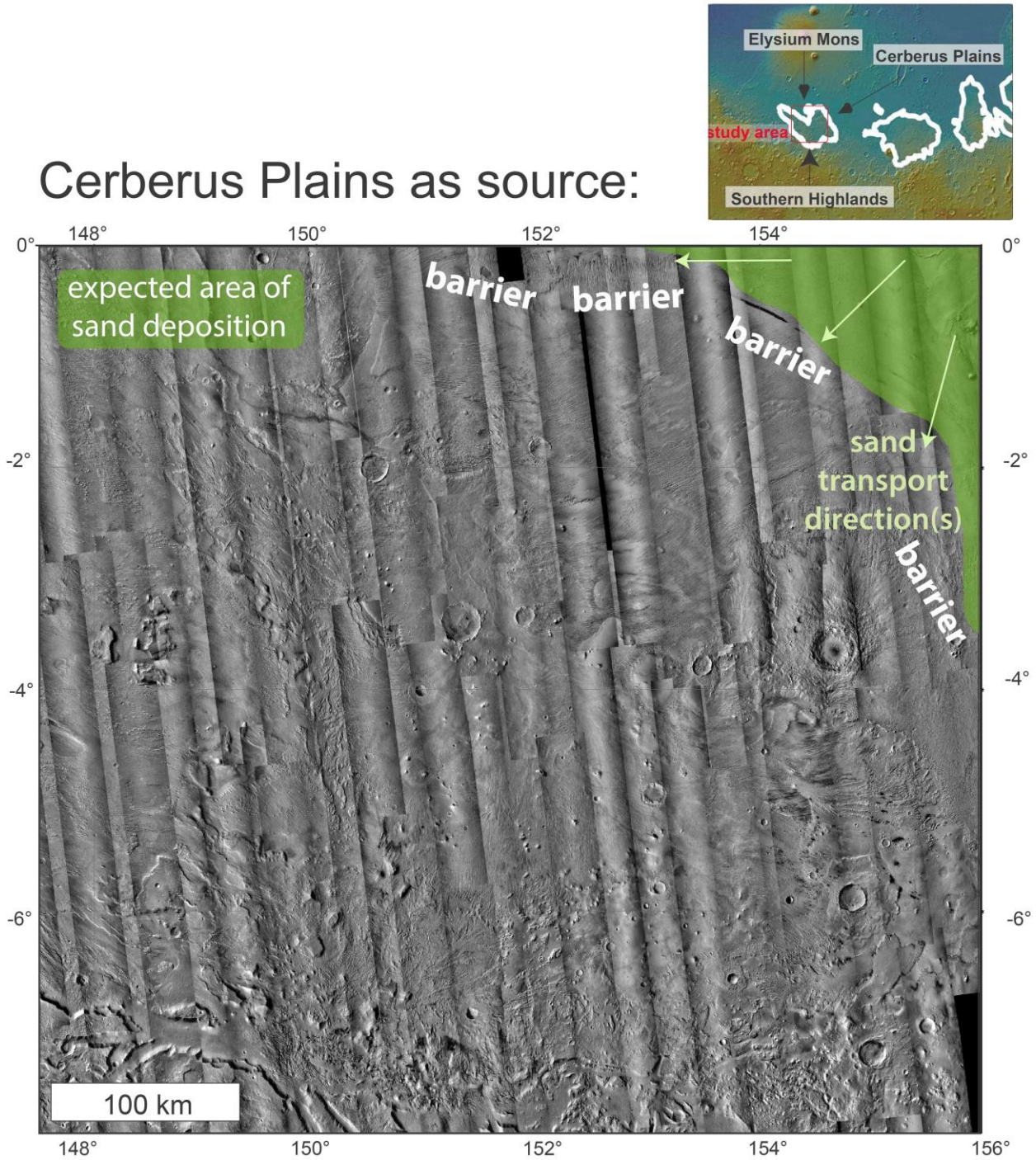
Figure 3.2. Expected sand distribution (color overlays) and inferred transport wind directions, (arrows) for sand sourced from the Cerberus Plains, located to the northeast of Aeolis Dorsa (see inset). 'Barrier' denotes highstanding obstacle likely to prevent sand transport.
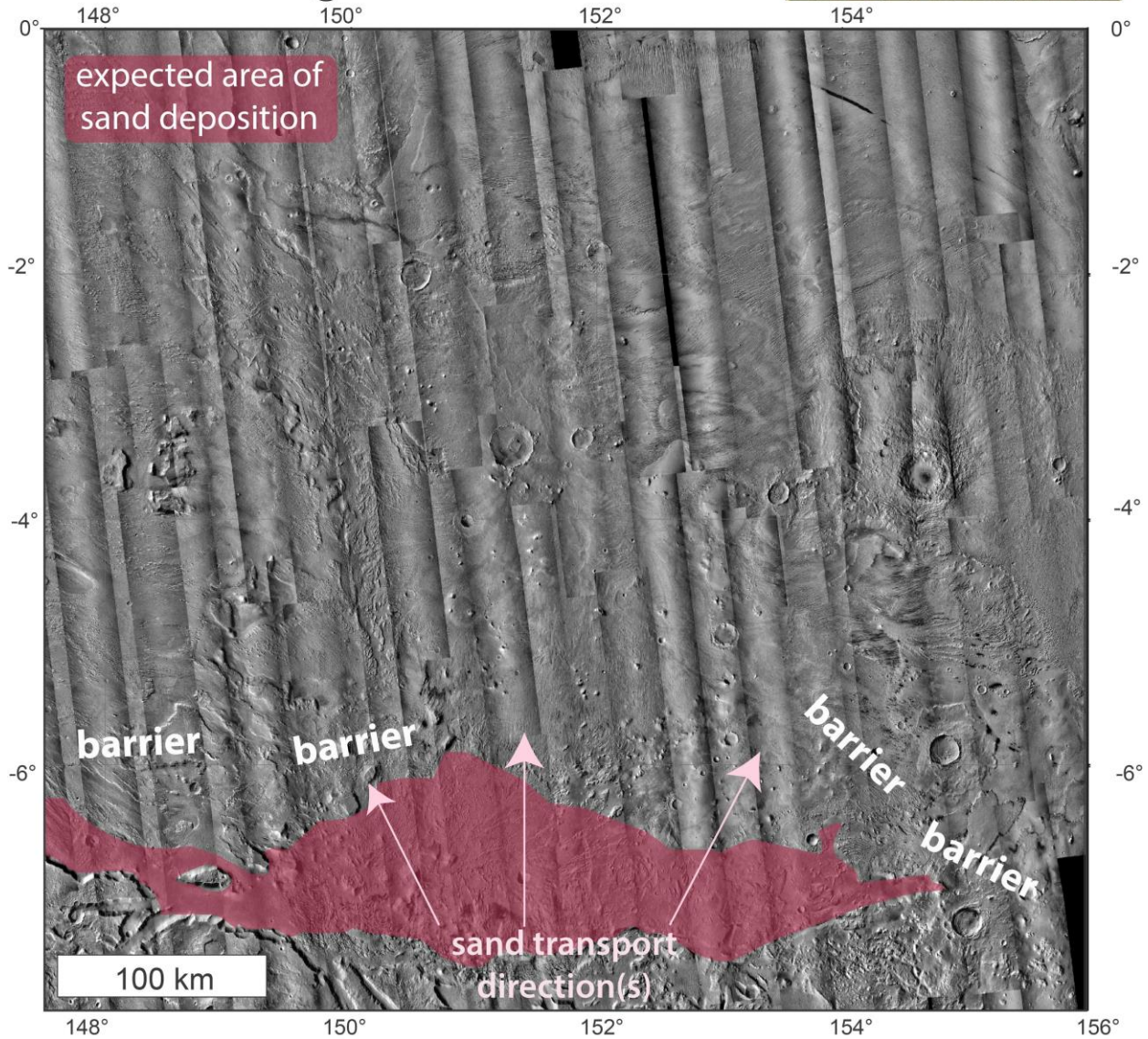
Figure 3.3. Expected sand distribution (color overlays) and inferred transport wind directions, (arrows) for sand sourced from the Southern Highlands, located to the south of Aeolis Dorsa (see inset). 'Barrier' denotes highstanding obstacle likely to prevent sand transport.

Medusae Fossae Fm.
as *in situ* source:
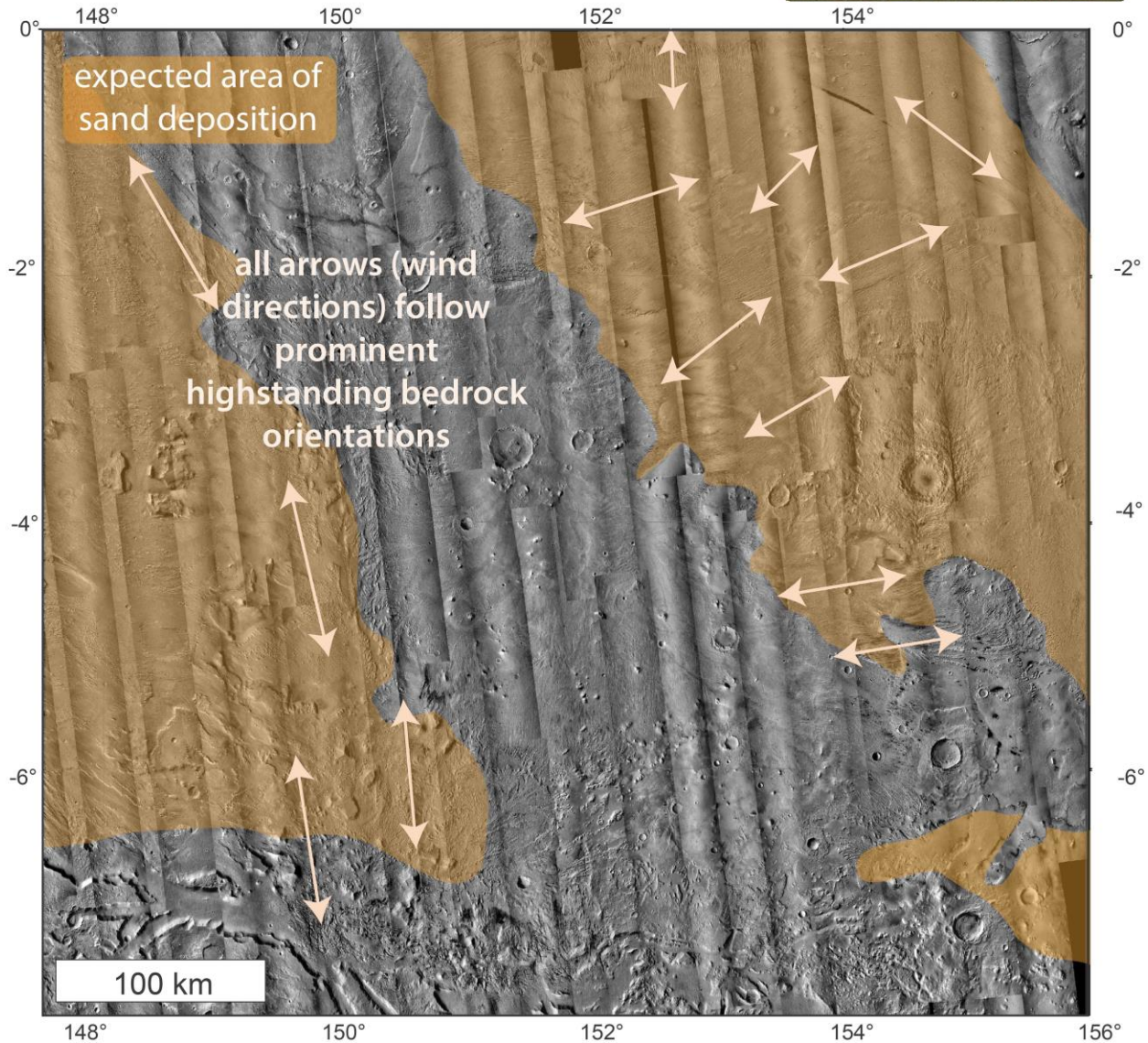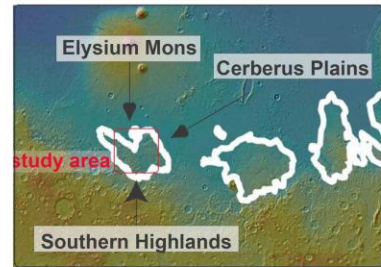
Figure 3.4. Expected sand distribution (color overlays) and inferred transport wind directions, (arrows) for sand sourced from *in situ* erosion of the Medusae Fossae Formation, comprising the two plana (Aeolis and Zephyria Plana) within Aeolis Dorsa (see inset).
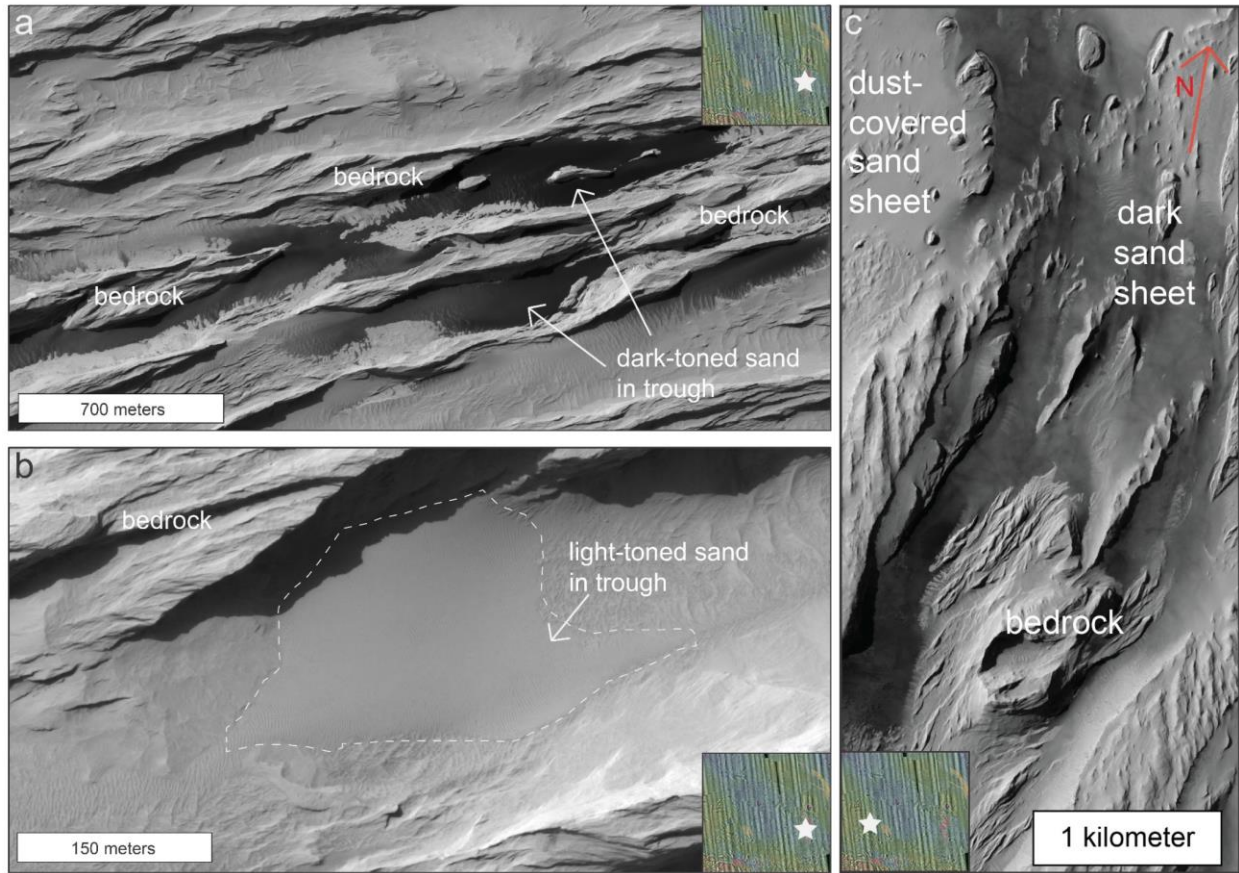
Figure 4.1. Sand deposits mapped in Aeolis Dorsa. a) Dark sand located within bedrock troughs. b) Light-toned sand deposit in bedrock trough. Note lenticular thickness of deposit. c) Sand sheets, both light-toned and dark-toned, in Aeolis Planum. Note smooth surface and abundant scour marks. All images: NASA/JPL/University of Arizona.
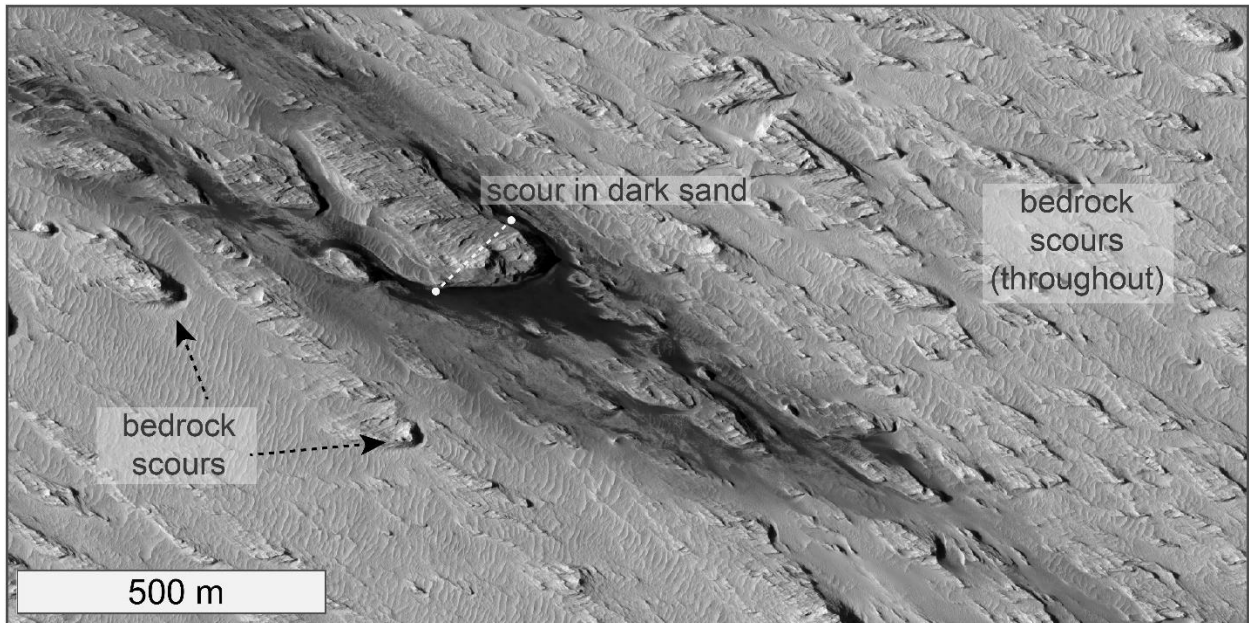
Figure 4.2. Scour in dark sand vs. scours in lithified sediments. Only scours in loose sediment (dark sediment, in this case) were mapped. Image credit: NASA/JPL/University of Arizona.
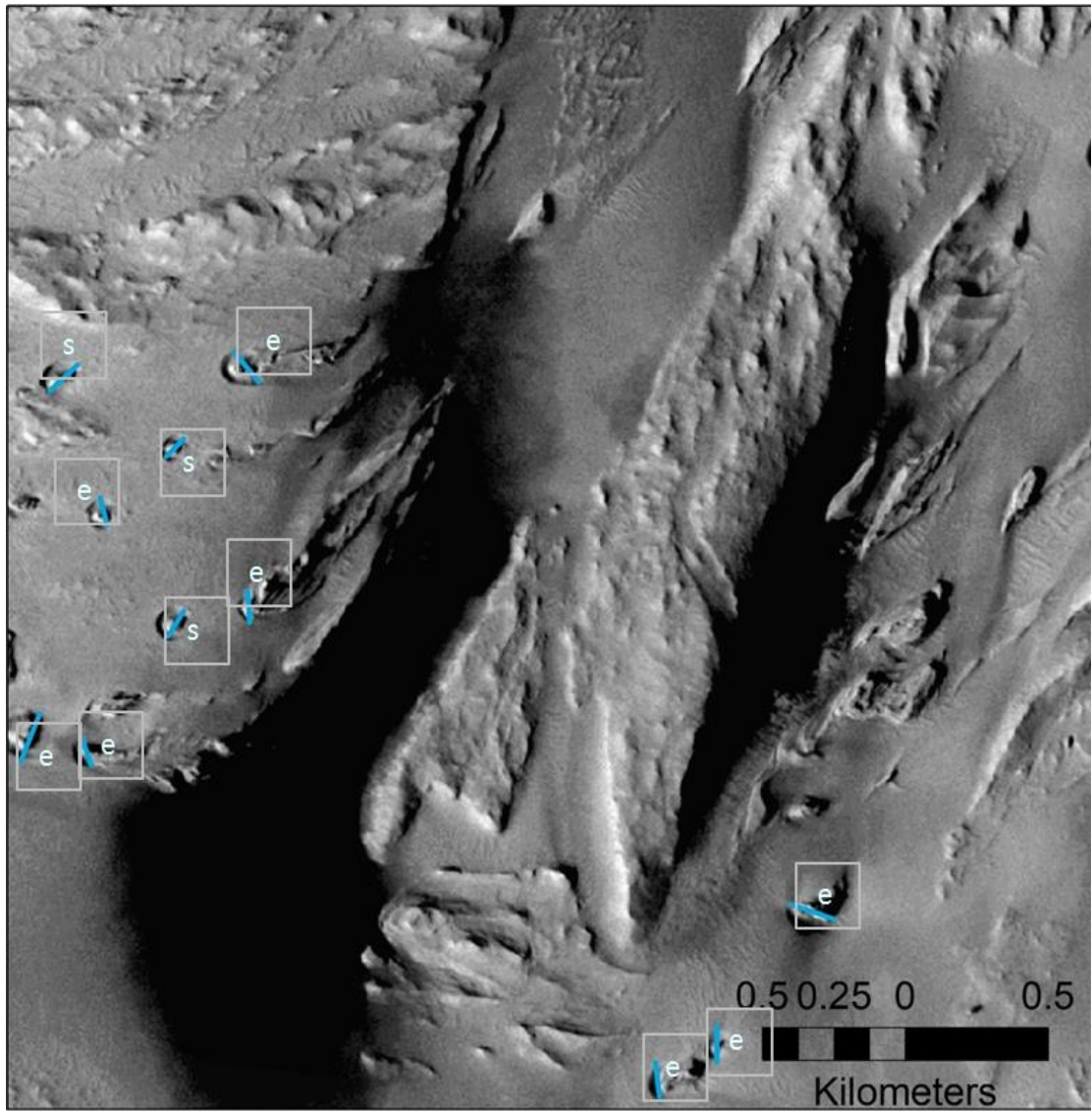
Figure 4.3. Example of denotations for scour marks mapped in ArcMap. Light blue lines indicate around-obstacle extent of each scour. Single letters mark wind directions (i.e., "e" = east-directed winds). This hemisphere is recorded in the ArcMap scour mark attribute table and subsequently used to calculate absolute inferred wind direction in MS Excel (see Section 4.2.2 and Appendix V).
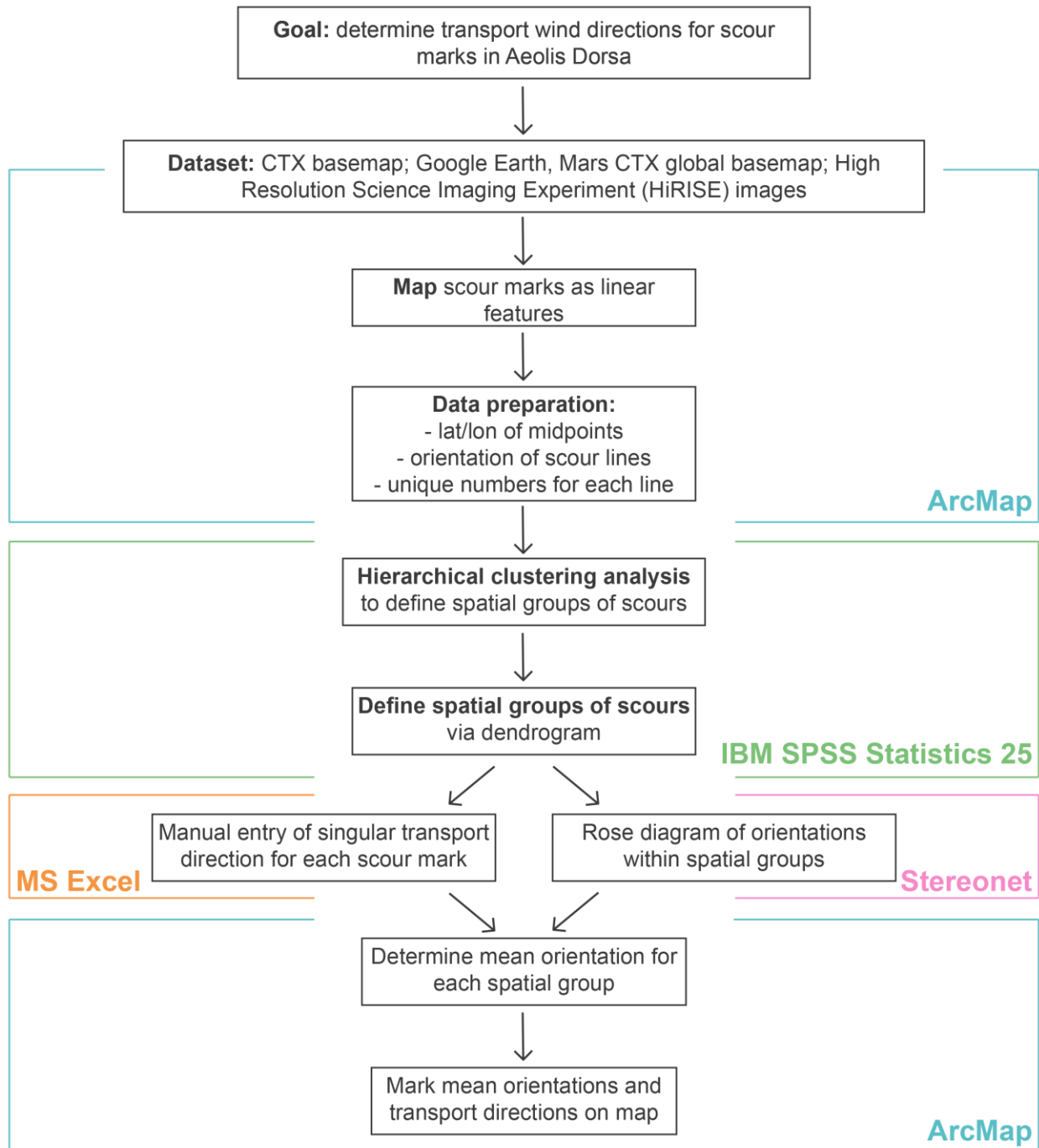
Figure 4.4. Flowchart describing steps taken to analyze spatial distribution of scour marks. Programs used for each step listed in different colors.
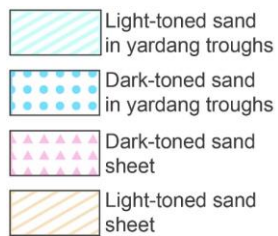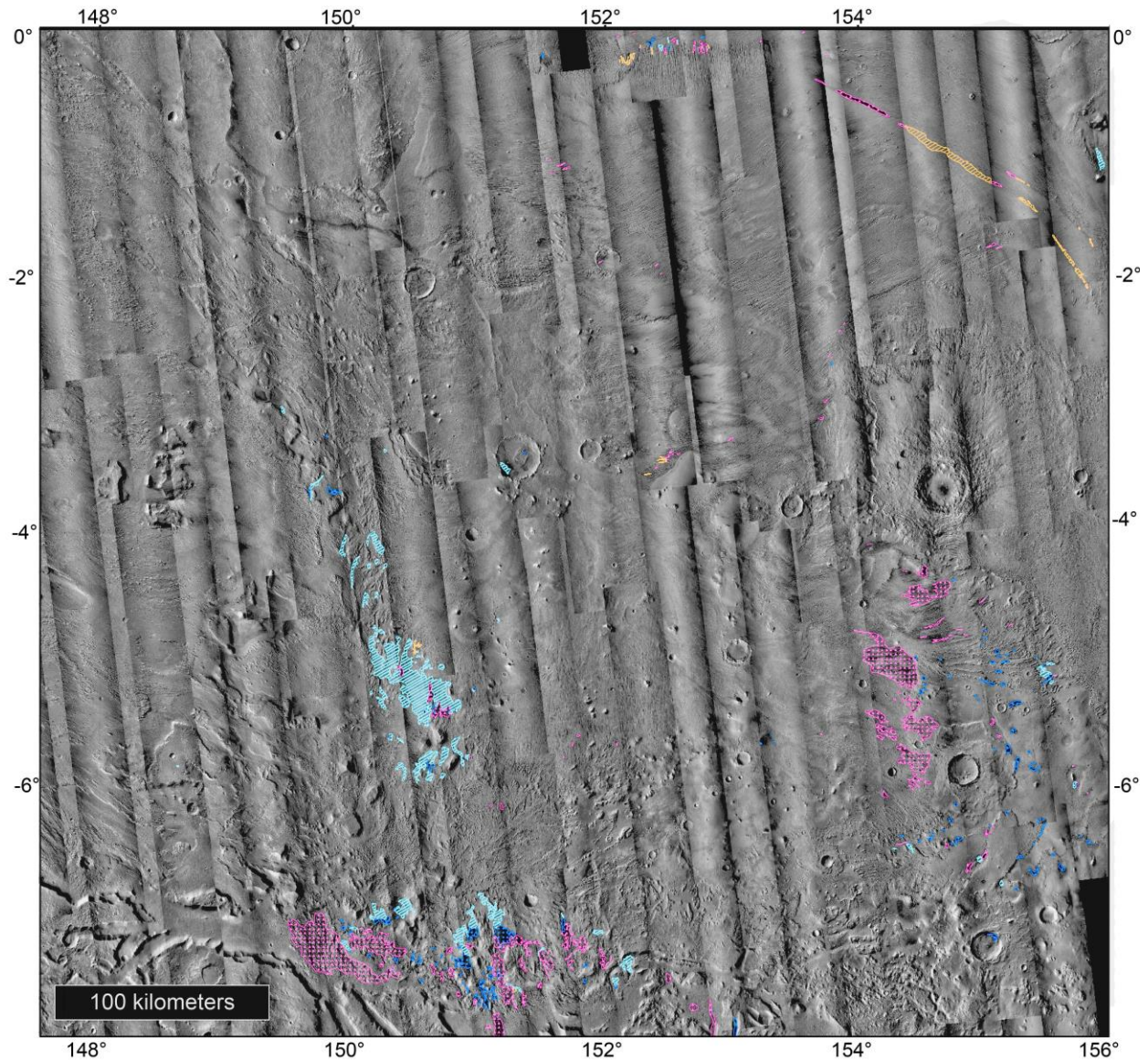
Figure 5.1. Sand deposits in Aeolis Dorsa, mapped according to four categories outlined in section 4.1: 1) dark-toned sand found in bedrock troughs, red (Fig. 4.1a); 2) light-toned sand found in bedrock troughs, med-tan in Zephyria Planum (Fig. 4.1b); 3) dark-toned sand sheets, light blue; esp. in southern depression (Fig. 4.1c); 4) light-toned sand sheets, med-tan (Fig. 4.1c).
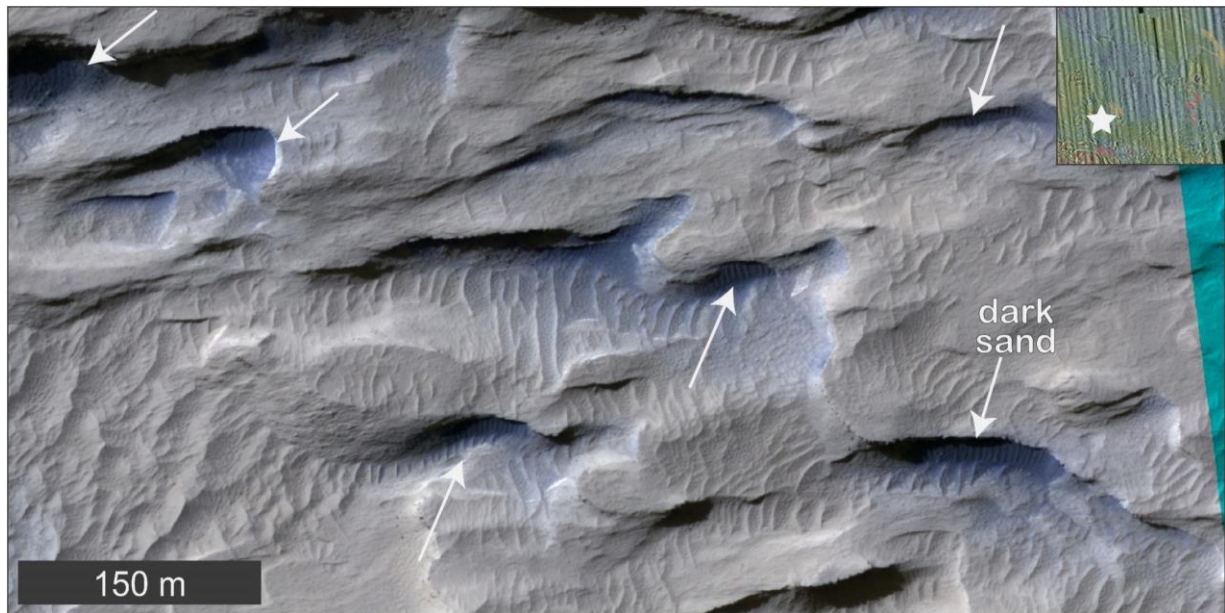
Figure 5.2. Dark sand deposits overlying the Medusae Fossae Formation in southern Aeolis Planum. HiRISE image ESP_035310_1740. Image courtesy of HiRISE/NASA/Univ. of Arizona.
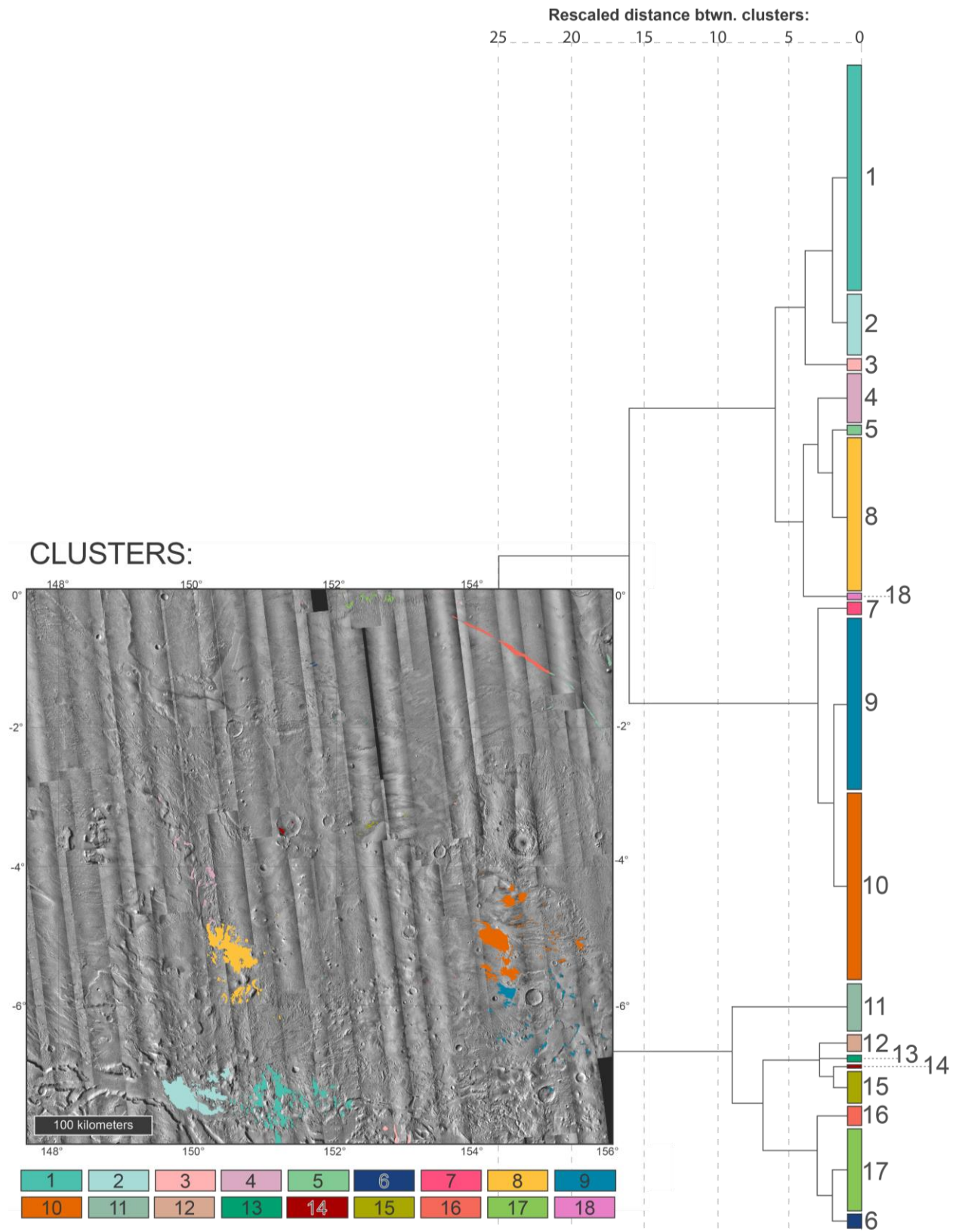
Figure 5.3. Map and dendrogram showing clusters of sand deposits within Aeolis Dorsa. Scours clustered by latitude and longitude.
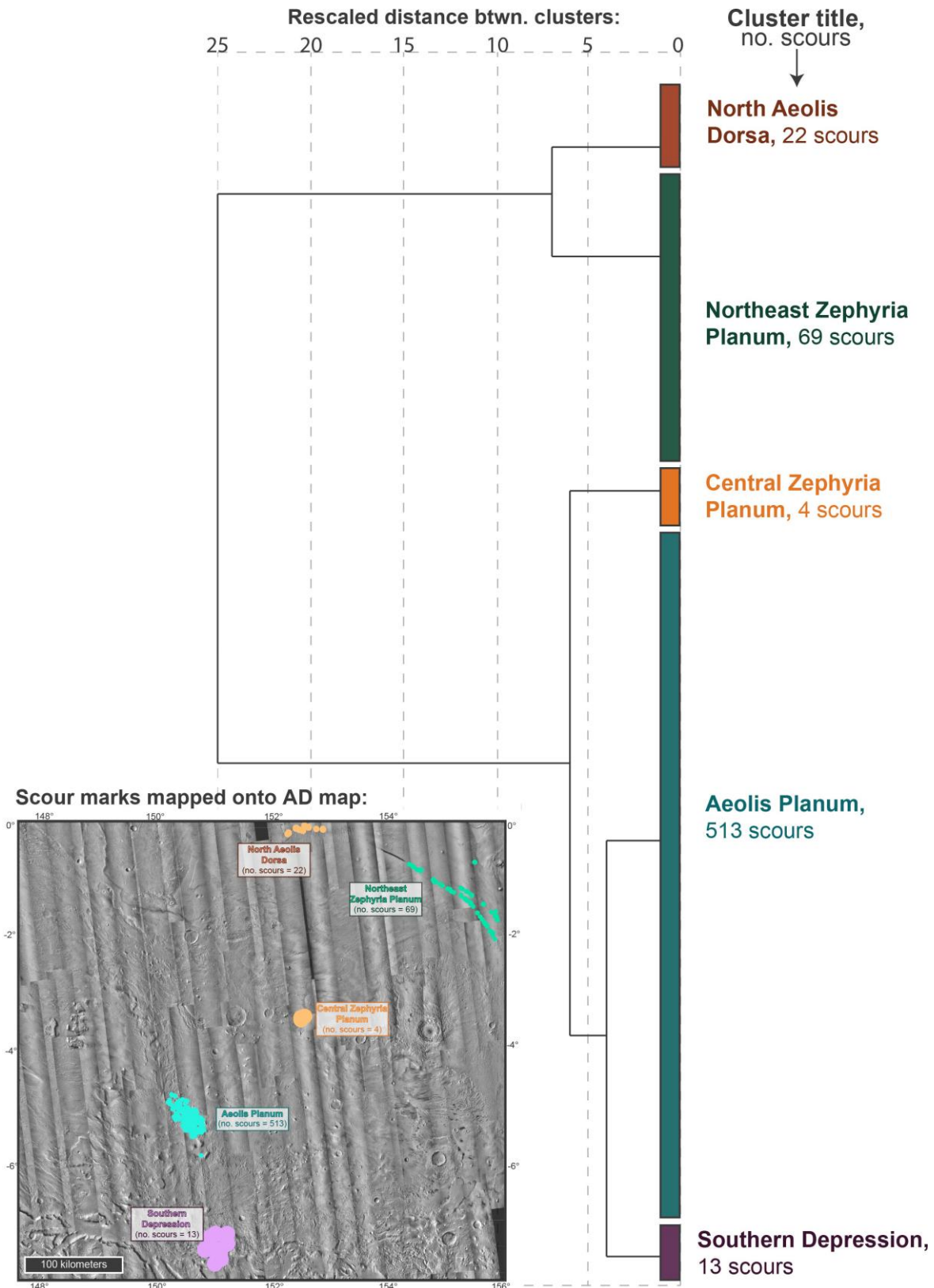
Figure 5.4. Simplified hierarchical clustering dendrogram showing five different clusters of scour marks in AD (extent shown on map). See full dendrogram, including individual scours, in Appendix IV. All 621 scours mapped used in clustering.
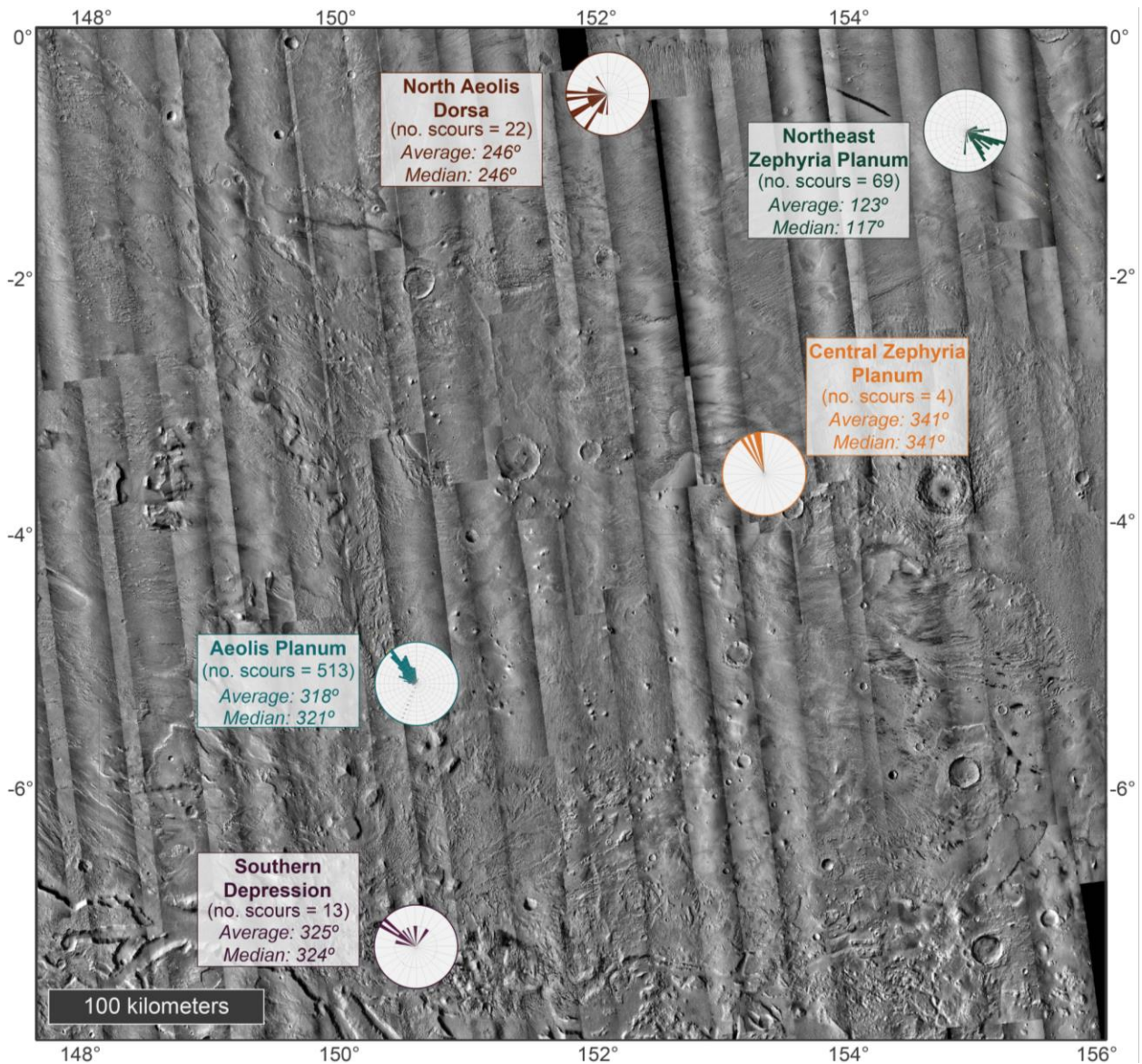
Figure 5.5 . Inferred wind directions for scours in each group determined by SPSS Statistics hierarchical clustering (see Fig. 5.4), presented as rose diagrams generated in GeoRose. See Table 5.2 for details on scour orientation statistics.
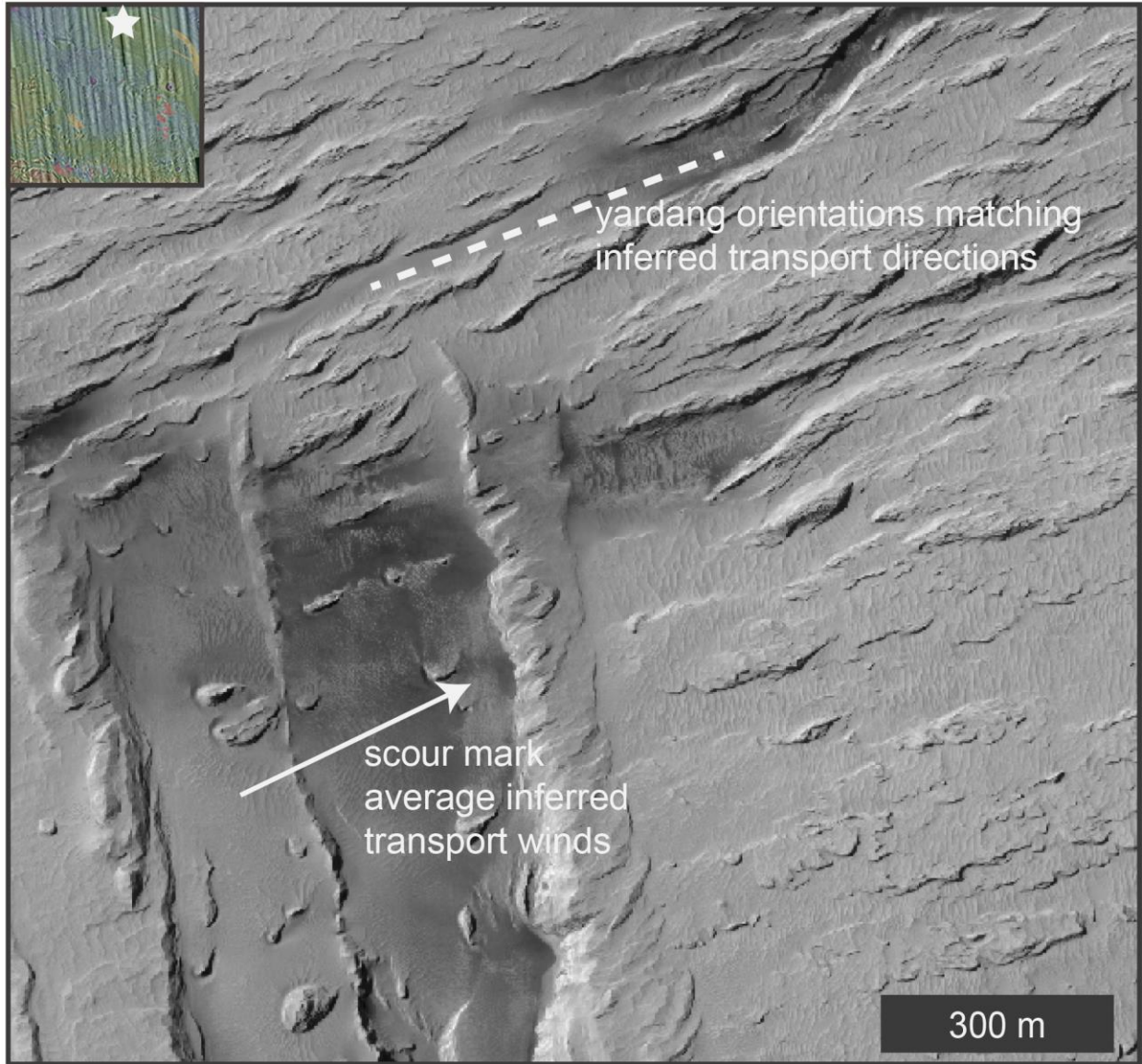
Figure 5.6. North Aeolis Dorsa scour marks and yardang fields. Scours occur within dark sand deposits between N-S yardang field, but inferred transport winds are parallel with NE-SW yardang field to the north of scours. Image: NASA/JPL/University of Arizona.
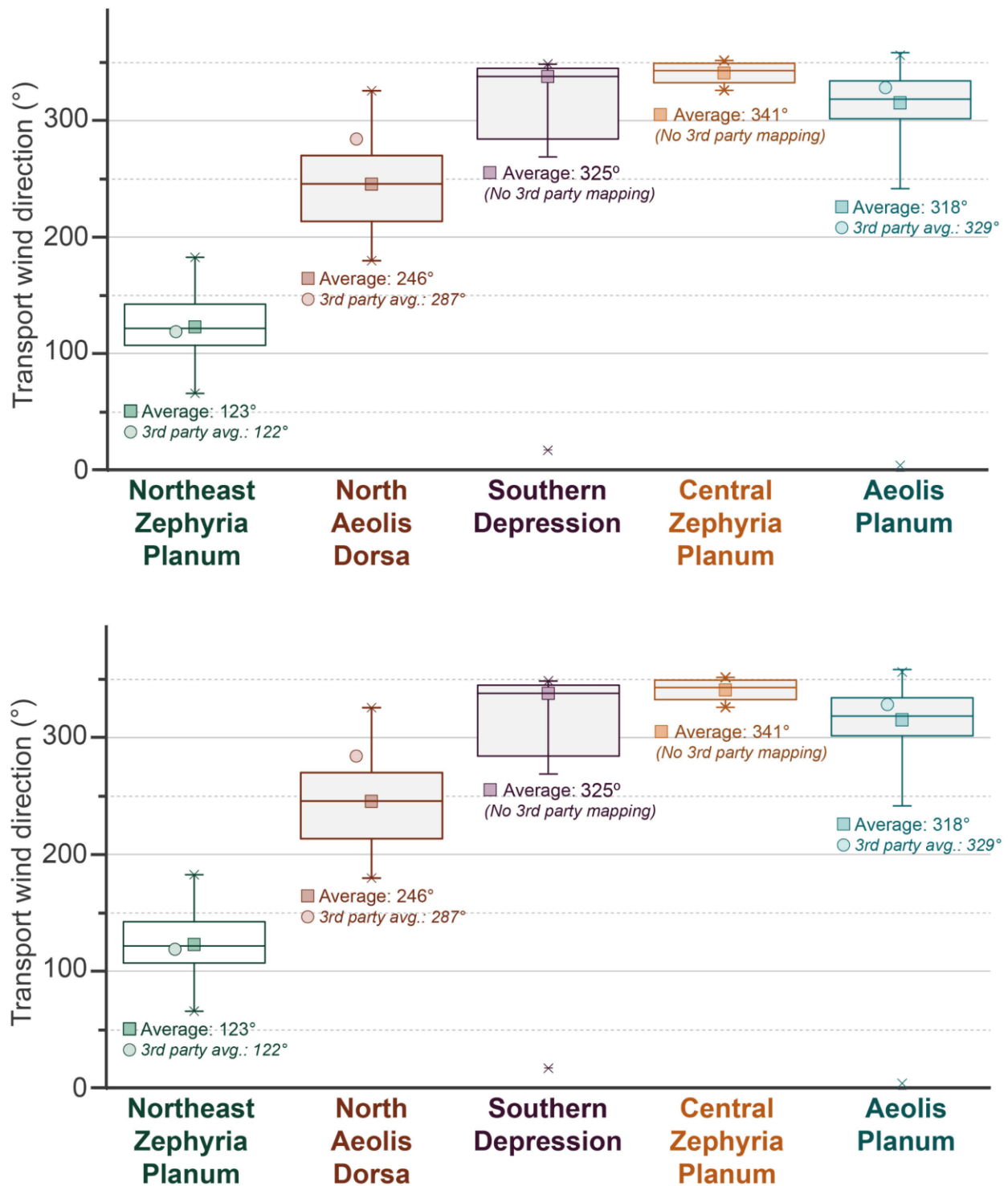
Figure 5.7. Box-and-whisker plot showing average inferred transport winds for all 621 scours within five clusters of scours (see Fig. 5.4). Measurements represent direction *from which* winds blew. Box-and-whisker plots represent all 621 scours that occur within sand deposits in Aeolis Dorsa. Circles represent third party error mapping of 62 scour marks (10% of all scours in AD).
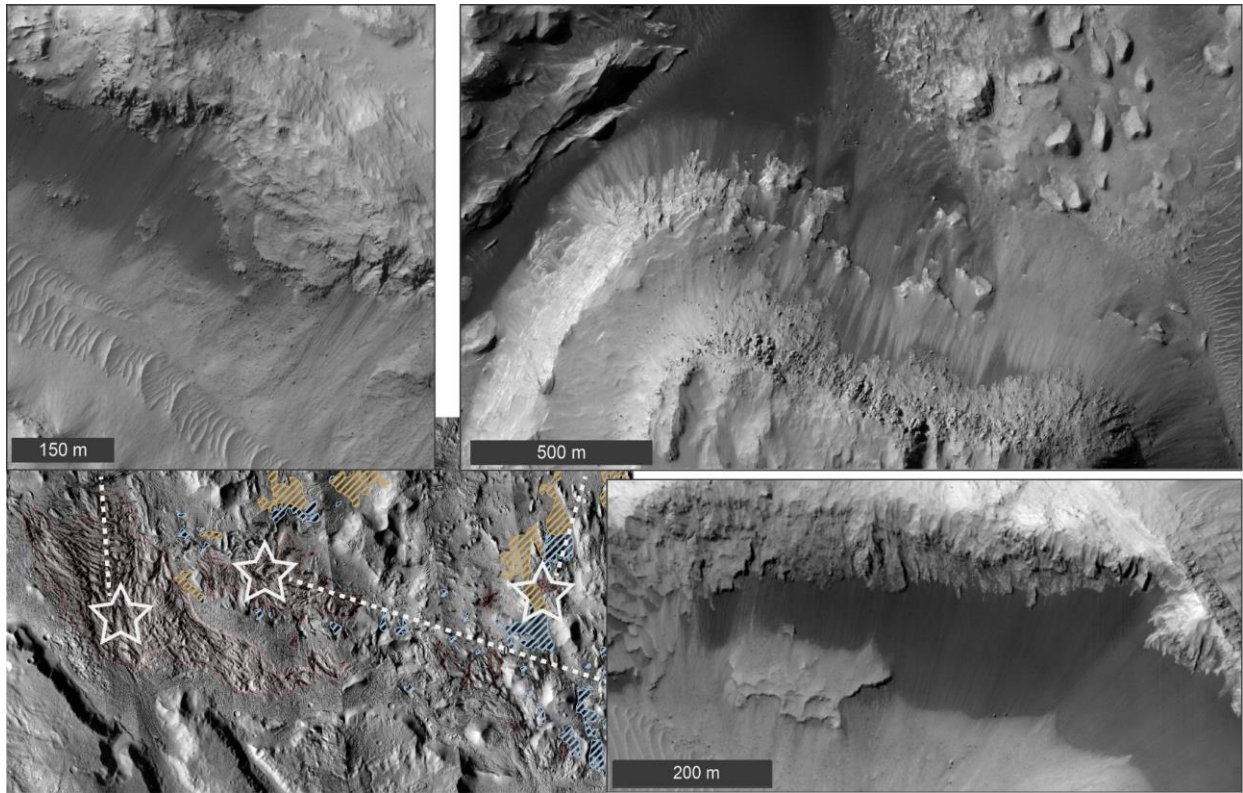
Figure 5.8. Examples of abundant erosion of dark sediments in bedrock within the southern depression. Credit for all three high-resolution images: NASA/JPL/University of Arizona.
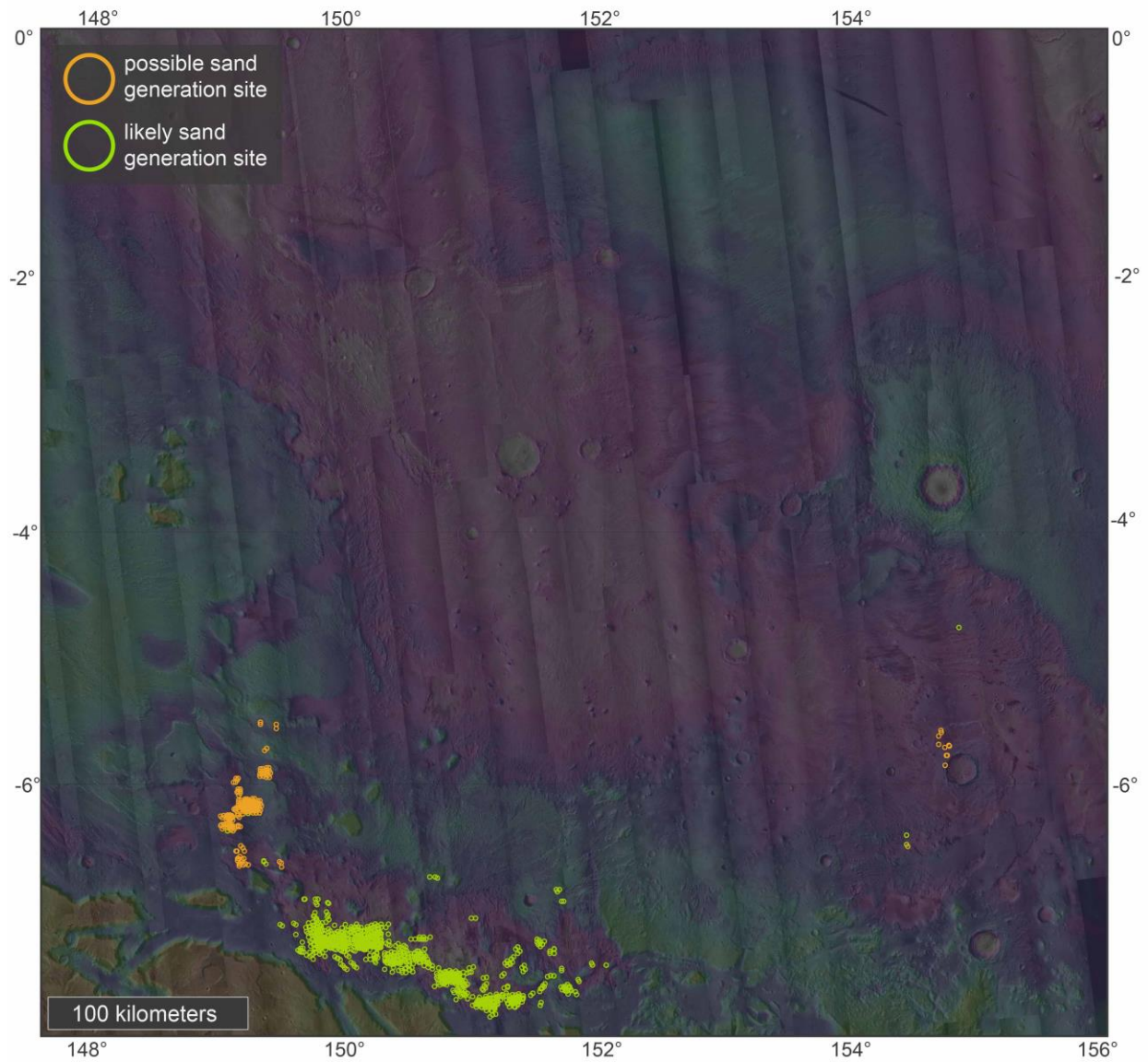
Figure 5.9. Map showing instances of possible and likely *in situ* sand generation in Aeolis Dorsa, concentrated on Aeolis planum, the southern depression, and to a limited extent Zephyria planum. 'Possible' sites are those that contain dark talus slopes emanating from bedrock layers, but do not continue to a dark sand deposit. 'Likely' sites are those that exhibit dark talus slopes extending downslope to dark sand deposits.
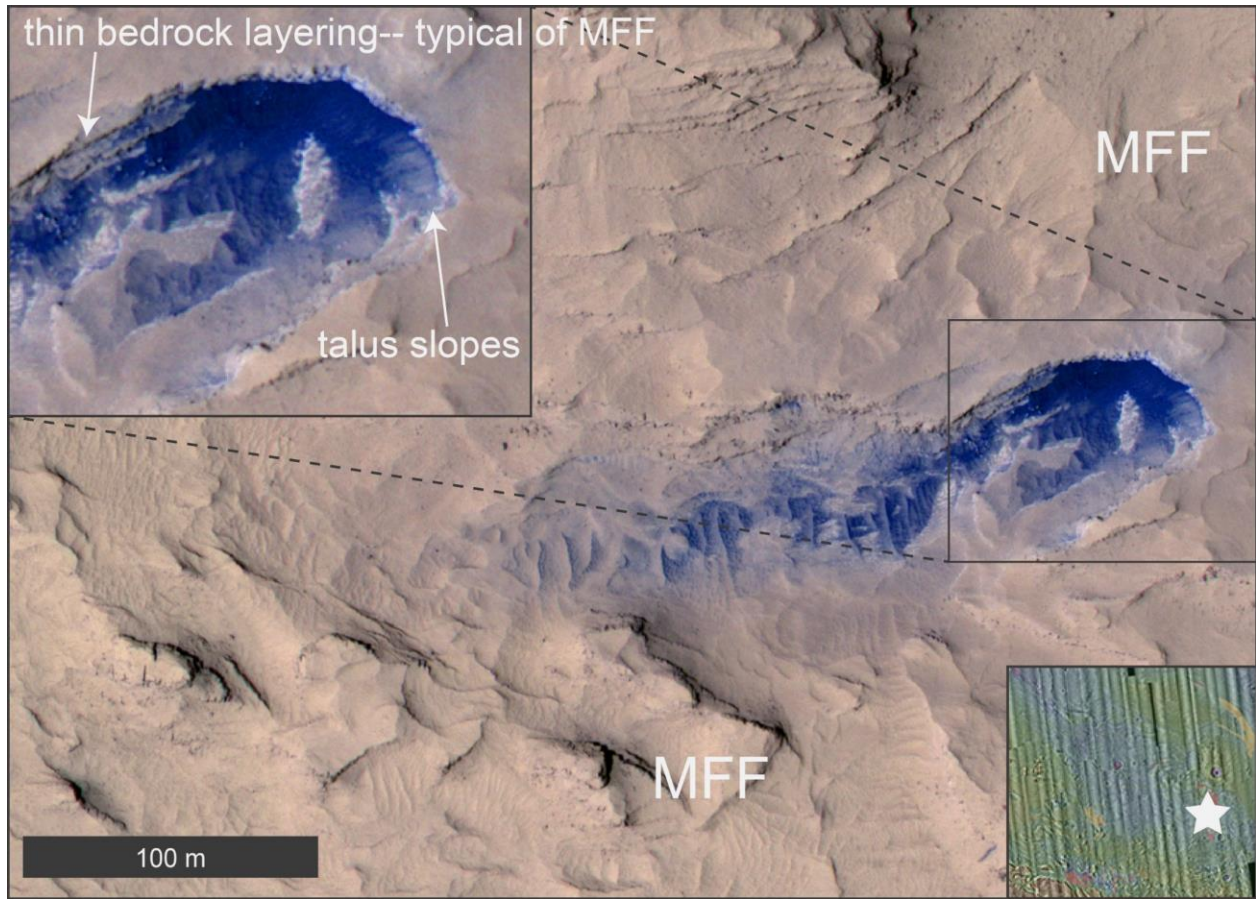
Figure 5.10. Bedrock erosion of yardangs in the MFF. Talus slopes, highlighted in inset, record apparent erosion and downslope transport of MFF sediments. Image: NASA/JPL/University of Arizona.
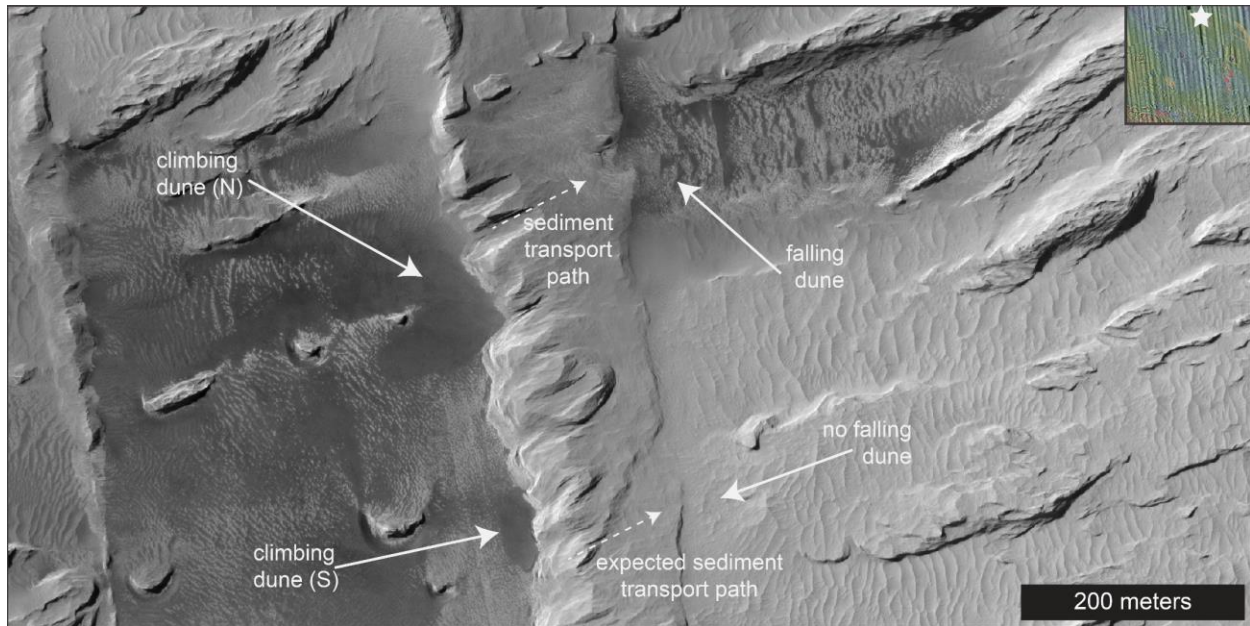
Figure 6.1. Sand transport apparently limited by yardang height in north Aeolis Dorsa. Note chutes on crest of yardang, which are evidence of wind abrasion and sediment pathways across yardang. The location toward the bottom of the image shows no such transport path across the yardang, indicating that yardang relief here prevented sediment from crossing yardang crest. Image: NASA/JPL/University of Arizona.
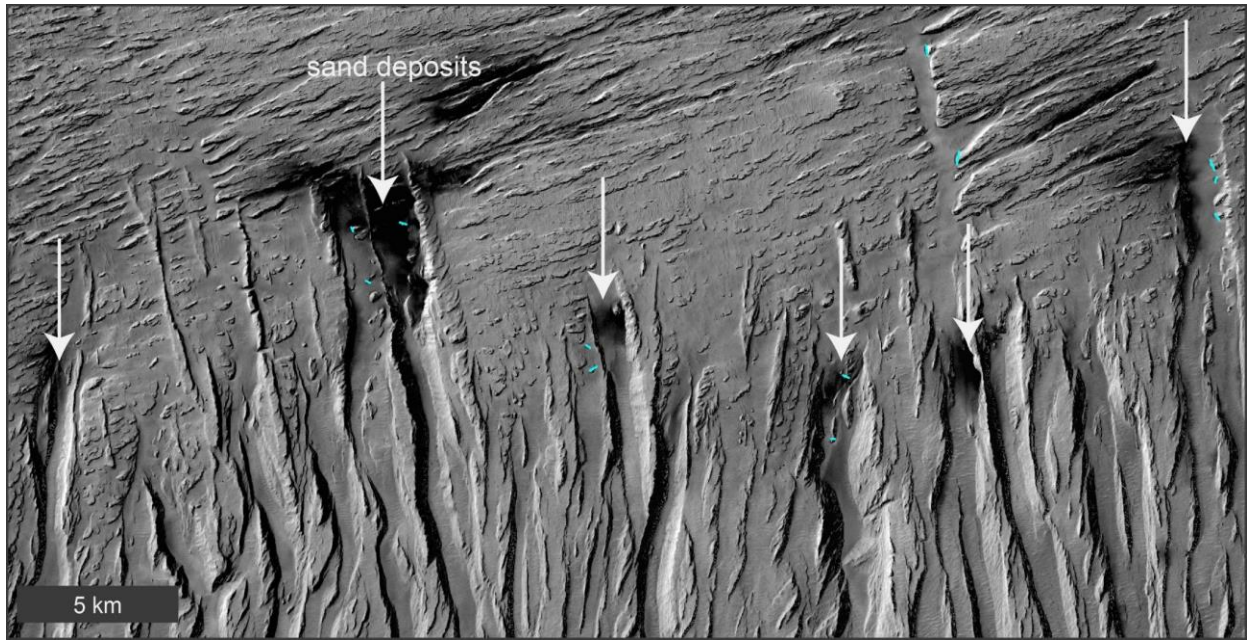
Figure 6.2. Sand deposits in northern Aeolis Dorsa, located on north end of N-S yardang field. Note NE-SW yardang field north of the N-S yardang field.

Figure 6.3. Dark ripples sourced from the Campo Piedra Pomez ignimbrite in Argentina. Photo from de Silva et al. (2010).

Appendix I: Code used to determine linear feature orientation
1) In ArcMap 10.5: within Linear feature attribute table, click "Add Field" and create a double- or float- type field.
2) Type field labeled 'orientation'.
3) Right-click on field header, and click "Field Calculator"
4) Within Field Calculator, click 'Show Codeblock'
5) Enter following text into the two text box prompts:

Pre-Logic Script Code:

```
defNorthAzimuth(Pline):
   degBearing =
math.degrees(math.atan2((Pline.lastPoint.X –
Pline.firstPoint.X),(Pline.lastPoint.Y -
Pline.firstPoint.Y)))
   if (degBearing <0):
      degBearing += 360.0
   return degBearing
```

orientation =

```
180 + math.atan2((!Shape.lastpoint.X! –
!Shape.firstpoint.X!),(!Shape.lastpoint.Y! –
!Shape.firstpoint.Y!)) * (180 / math.pi)
```

Appendix II: HiRISE stamps in study area

List shows all HiRISE stamps located within study area. All stamps were loaded in HiView (all via HiRISE team) and examined for evidence of dark sand generation. Only those that showed such generation are shown in the accompanying map directly below this paragraph (map longitude is in degrees E). These stamps can all be searched on the HiRISE website (https://hirise.lpl.arizona.edu/).

Map of stamps showing apparent dark sediment generation (numbers correspond with numbered stamps in list below):
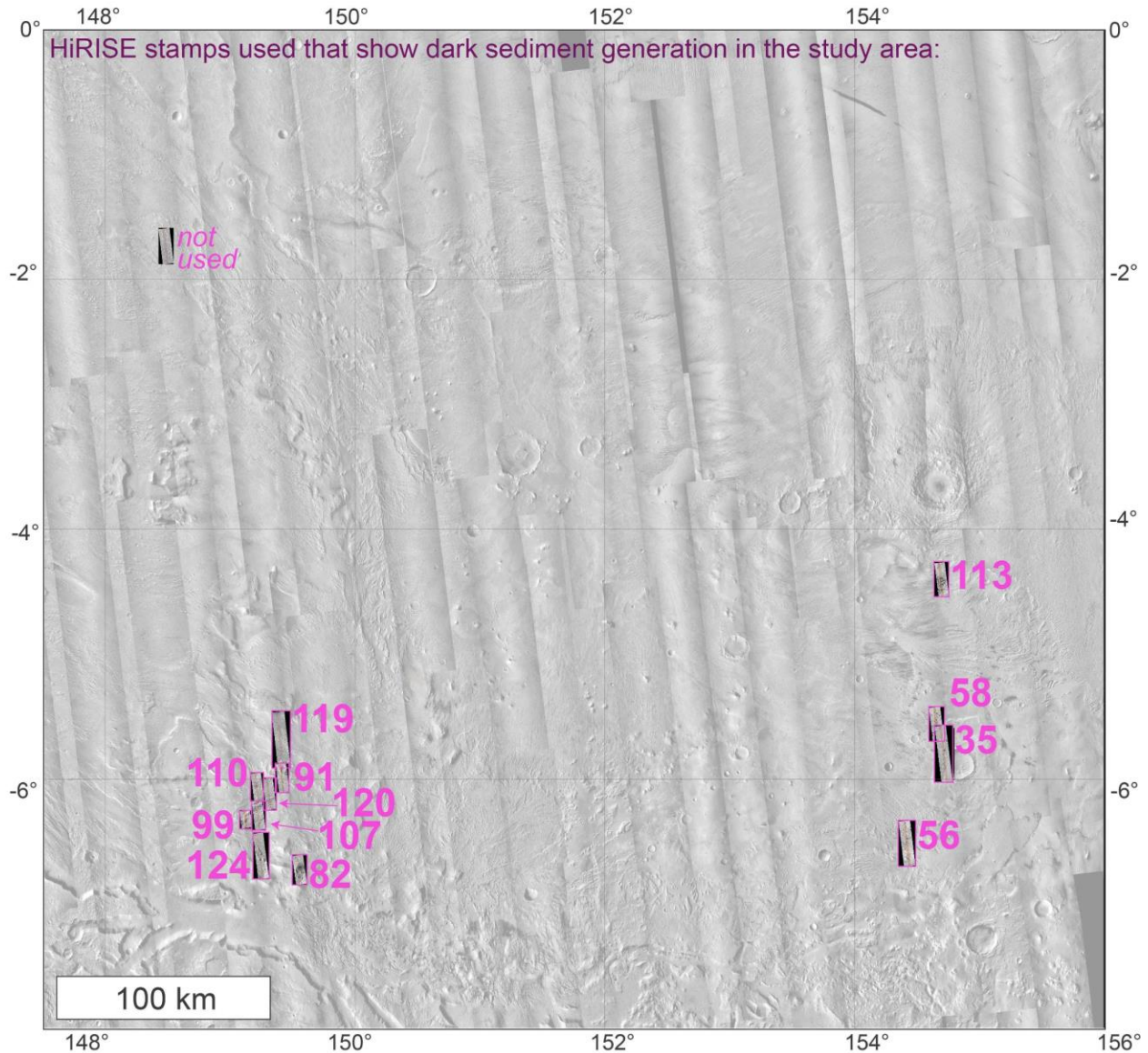
List of **all** HiRISE stamps in study area as of June 2018:

Number	HiRISE stamp				
1	ESP_014291_1770_	4	ESP_016190_1785_	8	ESP_016480_1750_
2	ESP_015913_1740_	5	ESP_016269_1750_	9	ESP_016546_1735_
3	ESP_016058_1740_	6	ESP_016348_1750_	10	ESP_016981_1745_
		7	ESP_016414_1775_	11	ESP_017047_1770_

12	ESP_017126_1755_	55	ESP_022862_1740_	98	ESP_033464_1720_
13	ESP_017324_1795_	56	ESP_023429_1735_	99	ESP_033820_1735_
14	ESP_017337_1770_	57	ESP_023706_1725_	100	ESP_033833_1800_
15	ESP_017548_1740_	58	ESP_023785_1745_	101	ESP_034044_1740_
16	ESP_017680_1775_	59	ESP_024062_1725_	102	ESP_034176_1735_
17	ESP_017693_1795_	60	ESP_024484_1750_	103	ESP_034189_1740_
18	ESP_017759_1770_	61	ESP_024497_1745_	104	ESP_034321_1780_
19	ESP_017825_1760_	62	ESP_024695_1745_	105	ESP_034545_1740_
20	ESP_018102_1775_	63	ESP_024985_1750_	106	ESP_034822_1790_
21	ESP_018115_1755_	64	ESP_025117_1725_	107	ESP_035099_1735_
22	ESP_018181_1730_	65	ESP_025196_1800_	108	ESP_035112_1765_
23	ESP_018392_1740_	66	ESP_025262_1745_	109	ESP_035244_1725_
24	ESP_018458_1760_	67	ESP_025407_1745_	110	ESP_035310_1740_
25	ESP_018603_1755_	68	ESP_025618_1750_	111	ESP_035389_1740_
26	ESP_018814_1740_	69	ESP_025829_1745_	112	ESP_035455_1780_
27	ESP_018893_1730_	70	ESP_026106_1780_	113	ESP_035468_1755_
28	ESP_018959_1730_	71	ESP_026119_1735_	114	ESP_035600_1765_
29	ESP_018972_1755_	72	ESP_026462_1740_	115	ESP_035666_1725_
30	ESP_019025_1730_	73	ESP_026818_1740_	116	ESP_035679_1800_
31	ESP_019038_1740_	74	ESP_026897_1755_	117	ESP_035890_1755_
32	ESP_019104_1740_	75	ESP_027095_1800_	118	ESP_036167_1730_
33	ESP_019249_1745_	76	ESP_027596_1745_	119	ESP_036233_1740_
34	ESP_019328_1750_	77	ESP_027807_1765_	120	ESP_036299_1740_
35	ESP_019394_1745_	78	ESP_028229_1785_	121	ESP_036312_1740_
36	ESP_019592_1755_	79	ESP_028295_1795_	122	ESP_036378_1740_
37	ESP_019605_1755_	80	ESP_028361_1785_	123	ESP_036444_1795_
38	ESP_019803_1765_	81	ESP_028374_1785_	124	ESP_036510_1735_
39	ESP_019882_1740_	82	ESP_028572_1775_	125	ESP_036523_1750_
40	ESP_019961_1750_	83	ESP_028717_1795_	126	ESP_036589_1725_
41	ESP_020304_1730_	84	ESP_028796_1760_	127	ESP_036655_1735_
42	ESP_020383_1740_	85	ESP_029284_1785_	128	ESP_036668_1750_
43	ESP_020515_1775_	86	ESP_029495_1760_	129	ESP_036721_1800_
44	ESP_020528_1750_	87	ESP_030062_1790_	130	ESP_036734_1760_
45	ESP_020594_1735_	88	ESP_030853_1770_	131	ESP_036800_1780_
46	ESP_020673_1750_	89	ESP_031064_1760_	132	ESP_036879_1740_
47	ESP_020739_1735_	90	ESP_031209_1740_	133	ESP_036945_1760_
48	ESP_020805_1740_	91	ESP_031908_1740_	134	ESP_037024_1750_
49	ESP_021728_1740_	92	ESP_031921_1750_	135	ESP_037143_1725_
50	ESP_022071_1725_	93	ESP_032620_1780_	136	ESP_037156_1800_
51	ESP_022084_1740_	94	ESP_032910_1795_	137	ESP_037301_1740_
52	ESP_022229_1745_	95	ESP_033187_1780_	138	ESP_037380_1790_
53	ESP_022361_1740_	96	ESP_033266_1765_	139	ESP_037512_1725_
54	ESP_022572_1725_	97	ESP_033411_1795_	140	ESP_037578_1765_

141	ESP_037789_1725_	184	ESP_049446_1800_	227	PSP_007975_1755_
142	ESP_037855_1730_	185	ESP_050303_1745_	228	PSP_008173_1745_
143	ESP_038066_1725_	186	ESP_050356_1735_	229	PSP_008621_1750_
144	ESP_038343_1785_	187	ESP_050725_1745_	230	PSP_008687_1780_
145	ESP_038963_1740_	188	ESP_051213_1735_	231	PSP_008766_1795_
146	ESP_039174_1730_	189	ESP_051780_1725_	232	PSP_008832_1770_
147	ESP_039240_1730_	190	ESP_052004_1750_	233	PSP_009254_1725_
148	ESP_039319_1765_	191	ESP_052637_1740_	234	PSP_009399_1760_
149	ESP_039385_1760_	192	ESP_052650_1750_	235	PSP_009478_1770_
150	ESP_039596_1720_	193	ESP_052703_1785_	236	PSP_009623_1755_
151	ESP_039675_1760_	194	ESP_052848_1785_	237	PSP_009966_1735_
152	ESP_039820_1750_	195	ESP_053072_1745_	238	PSP_010111_1735_
153	ESP_040097_1760_	196	ESP_053138_1750_	239	PSP_010322_1740_
154	ESP_040440_1740_	197	ESP_053639_1760_	240	PSP_010467_1750_
155	ESP_040809_1795_	198	ESP_053705_1800_	241	PSP_010533_1755_
156	ESP_041086_1720_	199	ESP_053837_1760_		
157	ESP_041864_1745_	200	ESP_054140_1735_		
158	ESP_041943_1745_	201	ESP_054404_1765_		
159	ESP_042800_1780_	202	ESP_054562_1750_		
160	ESP_043209_1775_	203	ESP_054694_1745_		
161	ESP_044000_1750_	204	ESP_054760_1770_		
162	ESP_044132_1750_	205	ESP_054826_1775_		
163	ESP_044686_1760_	206	ESP_055116_1735_		
164	ESP_045121_1740_	207	ESP_055195_1735_		
165	ESP_045253_1770_	208	PSP_001448_1735_		
166	ESP_045398_1755_	209	PSP_002002_1735_		
167	ESP_046031_1730_	210	PSP_002279_1735_		
168	ESP_046044_1750_	211	PSP_002424_1765_		
169	ESP_046097_1740_	212	PSP_003149_1740_		
170	ESP_046321_1760_	213	PSP_003980_1720_		
171	ESP_046664_1740_	214	PSP_004125_1720_		
172	ESP_047231_1745_	215	PSP_005826_1780_		
173	ESP_047587_1765_	216	PSP_006683_1740_		
174	ESP_047811_1785_	217	PSP_006749_1780_		
175	ESP_047877_1775_	218	PSP_006815_1780_		
176	ESP_048233_1770_	219	PSP_006894_1740_		
177	ESP_048246_1750_	220	PSP_006973_1740_		
178	ESP_048299_1740_	221	PSP_007395_1775_		
179	ESP_048457_1765_	222	PSP_007474_1745_		
180	ESP_048668_1735_	223	PSP_007606_1785_		
181	ESP_048747_1750_	224	PSP_007619_1755_		
182	ESP_048800_1745_	225	PSP_007764_1795_		
183	ESP_048813_1735_	226	PSP_007830_1755_		

Appendix III: SPSS Hierarchical Cluster input, to determine spatial groups of scour marks

The attribute table as described in Section 4.5 was first exported to MS Excel (.xlsx) via the 'Table to Excel' tool in the ArcMap toolbox (Path: ArcToolbox → Conversion → Excel → Table to Excel…). These data were then imported into IBM SPSS Statistics 25 as input for the SPSS Hierarchical Cluster tool.

The 'Hierarchical Cluster' tool in SPSS Statistics 25 identified spatial groupings of scour marks in Aeolis Dorsa using options highlighted in the associated screenshot (below). A step-by-step setup for the cluster analysis that grouped scour marks is shown, beginning with selecting the appropriate tool, then choosing the appropriate variable input and case label. All options selected are shown in the Statistics, Plots, and Method windows below.

Screenshots of steps used to create dendrogram in [methods figure X]:

Dendrogram using Average Linkage (Between Groups)

Rescaled Distance Cluster Combine
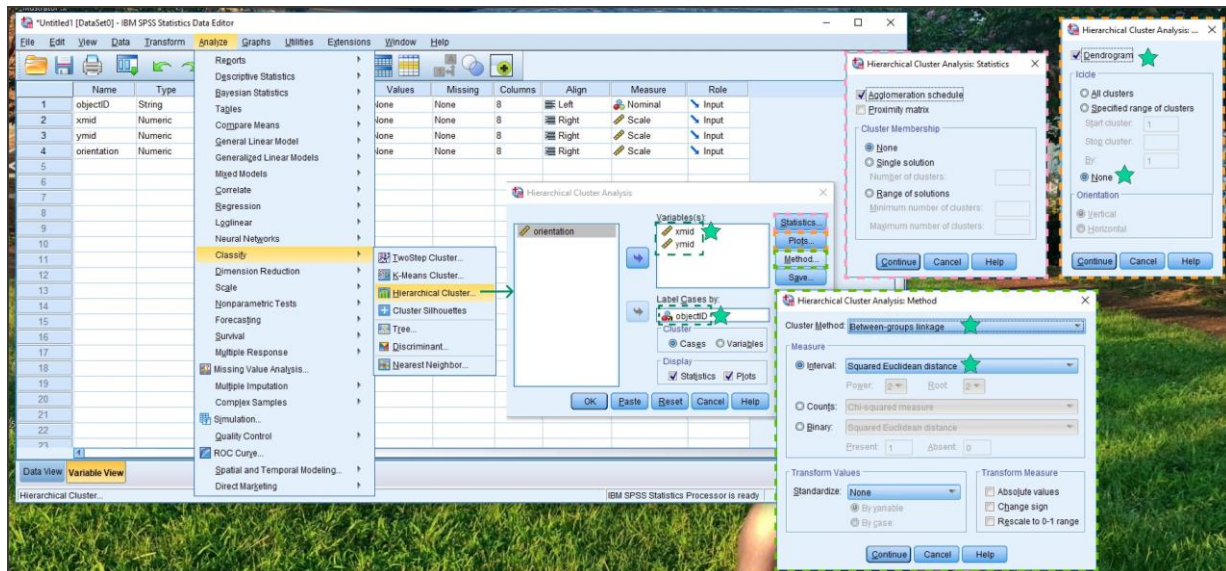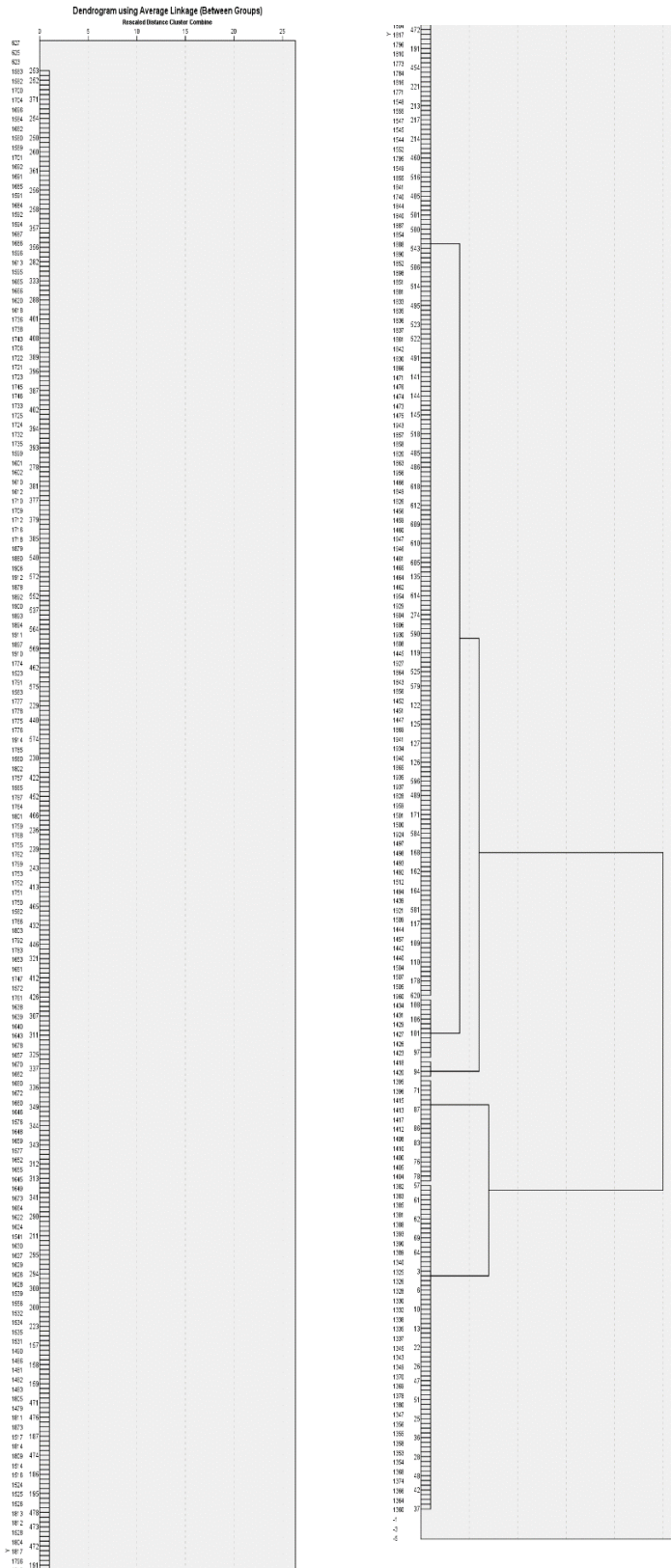
Appendix V: Scour mark data output table

The following table displays all relevant data collected on individual scour marks in Aeolis Dorsa. Scour mark unique IDs, latitude, longitude, and azimuthal orientation. These four data columns were collected in ArcMap (see Methods). The column labeled 'Compass direction' contains single hemispheres or quadrants within which lie inferred transport wind direction of scour marks.

Explanation - Scour mark data	
• **Scour mark ID**	"OBJECTID" from ArcMap
• **Latitude**	ymid' from ArcMap table
• **Longitude**	'xmid' from ArcMap table
• **Azimuthal orientation**	here, values are determined via: =IF(X2<0,X2+360,X2) where [X2] = the ArcMap derived orientation, which operates an absolute scale with *due N* = 0, NW values are negative and NE values are positive.
• **Compass direction**	Entered manually by A. Boyd as single compass directions, from looking at each scour mark in ArcMap and identifying a hemisphere in which a particular scour mark falls
• **Inferred wind direction (unformatted)**	Inferred wind direction, based on manually-entered hemisphere in compass direction; one of two formulas used, depending on hemisphere of inferred wind direction: =[X2]-90 or =[X2]+90
• **Azimuthal inferred wind direction**	here, values are determined via: =IF(X2<0,X2+360,X2) where [X2] = the ArcMap derived orientation, which operates an absolute scale with due N = 0, NW values are negative and NE values are positive.
Top row:	
• **Region**	See methods Fig XX, where each region is outlined
• **Average inferred winds**	Determined via: =AVERAGE(X#:X##) where X# and X## are the start- and end-cells for inferred winds in each region

Region:	NE Zephyria Planum	N. Aeolis Dorsa	Southern Aeolis Dorsa	Central Zeph. Planum	E. Aeolis Planum
Average inferred winds (°):	282.3186	65.65438672	161.2071181	160.5921005	138.0765377

Scour unique ID	Latitude	Longitude	Azimuthal orientation (°)	Compass direction	Inferred winds (unformatted)	Azimuthal inferred wind direction (°)
1381	-1.3858241	155.3391204	337.0700	w	247.0700	247.0700
1366	-1.3550247	155.3095529	339.2300	N	249.2300	249.2300
1364	-1.3731294	155.3212299	340.5600	N W	250.5600	250.5600
1353	-1.3646127	155.3113205	342.7600	n	252.7600	252.7600
1373	-1.3520787	155.2915017	346.7595	n	256.7595	256.7595
1363	-1.3453081	155.3020539	348.0239	n	258.0239	258.0239
1357	-1.2343979	155.3468336	353.6598	n	263.6598	263.6598
1332	-1.2182215	155.3169983	355.2364	n	265.2364	265.2364
1388	-1.1614471	155.2211322	356.3478	n	266.3478	266.3478
1374	-1.1743952	155.2453293	356.6335	n	266.6335	266.6335
1375	-1.1823763	155.2527212	357.6141	N W	267.6141	267.6141
1389	-1.3054027	155.2300099	2.1211	W N	-87.8789	272.1211
1351	-1.2859589	155.2265283	3.1798	W N	-86.8202	273.1798
1334	-1.2382760	155.1007272	3.3665	N W	-86.6335	273.3665
1345	-1.2202248	155.0592685	14.0362	N	-75.9638	284.0362
1365	-1.2017987	155.0422886	14.0363	N W	-75.9637	284.0363
1392	-1.1862865	155.0379499	15.9454	N W	-74.0546	285.9454
1329	-1.1227914	154.9050569	17.4472	N W	-72.5528	287.4472
1358	-1.1730454	154.9937593	17.6501	N W	-72.3499	287.6501
1367	-1.0952058	154.8684404	17.8189	N	-72.1811	287.8189
1352	-1.0577108	154.7862192	19.4400	N	-70.5600	289.4400
1346	-1.0321392	154.7580444	19.4400	nw	-70.5600	289.4400
1378	-1.0433877	154.7822554	19.5367	nw	-70.4633	289.5367
1383	-1.0119669	154.7434213	20.5561	nw	-69.4439	290.5561
1335	-1.0467516	154.7500097	20.7723	nw	-69.2277	290.7723
1379	-0.8660471	154.5162767	21.8014	nw	-68.1986	291.8014
1327	-0.8420503	154.5350242	23.1986	nw	-66.8014	293.1986
1356	-0.8049303	154.4176113	23.1986	nw	-66.8014	293.1986
1324	-0.7877361	154.3797413	23.9625	nw	-66.0375	293.9625
1328	-0.7772375	154.3877760	26.5650	nw	-63.4350	296.5650
1348	-0.8437644	154.4623374	26.5651	nw	-63.4349	296.5651
1354	-0.7503161	154.3271948	26.5651	N W	-63.4349	296.5651
1377	-0.7474237	154.3215169	27.4076	N W	-62.5924	297.4076
1333	-0.1399313	152.8205752	28.2173	W	-61.7827	298.2173
1338	-0.1338250	152.8188612	32.1957	nw	-57.8043	302.1957
1336	-0.1441093	152.8221286	33.6901	N W	-56.3099	303.6901
1330	-0.1309968	152.7066333	34.5085	N	-55.4915	304.5085
1382	-0.1672598	152.4727395	36.2538	N W	-53.7462	306.2538
1386	-0.1512012	152.4760605	36.3843	N W	-53.6157	306.3843
1325	-0.1007865	152.5710835	36.8699	N W	-53.1301	306.8699
1387	-0.1103210	152.5715121	37.4053	W	-52.5947	307.4053
1326	-0.1000000	152.5048781	39.5597	W	-50.4403	309.5597
1361	-0.0970370	152.5702265	41.4237	nw	-48.5763	311.4237
1369	-0.0676303	152.4967899	43.3904	nw	-46.6096	313.3904
1331	-0.1154310	152.3510093	46.0809	N W	-43.9191	316.0809
1339	-0.1134491	152.3491346	46.9749	N	-43.0251	316.9749
1341	-0.1119493	152.3622043	49.0856	N	-40.9144	319.0856
1390	-0.1268938	152.3532590	49.7636	nw	-40.2364	319.7636
1340	-0.1434880	152.4098229	50.3893	nw	-39.6107	320.3893
1385	-0.1492194	152.4111085	50.9645	W	-39.0355	320.9645
1368	-0.2054511	152.2234728	52.1250	N W	-37.8750	322.1250
1391	-0.2029872	152.2229372	53.1301	N W	-36.8699	323.1301
1376	-0.2216811	152.2055288	54.4623	N W	-35.5377	324.4623
1355	-0.2185744	152.2049396	55.4375	N W	-34.5625	325.4375
1393	-0.1935599	152.2224551	56.3099	N	-33.6901	326.3099
1359	-3.4410596	152.4479685	56.3099	W	-33.6901	326.3099
1380	-3.4342525	152.4428353	56.6593		-33.3407	326.6593
1350	-3.4180716	152.4429469	57.1714	W	-32.8286	327.1714
1384	-3.4017680	152.5120448	59.9314	N	-30.0686	329.9314
1349	-6.9911726	150.3718456	60.5725	N W	-29.4275	330.5725
1337	-7.4708943	150.7642977	63.4350		-26.5650	333.4350
1323	-7.2612571	150.8531296	77.0054	N	-12.9946	347.0054
1360	-7.3801296	150.8512548	80.9097	W	-9.0903	350.9097
1394	-7.3783888	150.8484427	83.2902	W	-6.7098	353.2902
1347	-7.1947437	150.9510585	85.2363	W	-4.7637	355.2363
1370	-7.4562311	150.8959007	90.0000	N	0.0000	0.0000
1343	-7.7139288	150.9374799	91.3972	W	1.3972	1.3972
1344	-7.6383630	151.0399752	92.3373	N	2.3373	2.3373

Scour unique ID	Latitude	Longitude	Azimuthal orientation (°)	Compass direction	*Inferred winds (unformatted)*	Azimuthal inferred wind direction (°)
1371	-7.5805136	151.0264502	92.6026	N	*2.6026*	2.6026
1395	-7.4694347	151.0404439	326.3099	E	*56.3099*	56.30994636
1396	-7.3660155	151.1554062	327.5288	E	*57.5288*	57.52882363
1397	-7.1949312	151.1526610	333.4349	E	*63.4349*	63.43491273
1398	-5.3995793	150.6574412	338.1986	E	*68.1986*	68.19860918
1399	-5.4214574	150.6559944	349.9920	N	*79.9920*	79.99203837
1400	-5.4019287	150.6931547	350.7890	N	*80.7890*	80.78896896
1401	-5.4256979	150.6456610	352.8750	E N	*82.8750*	82.87496052
1403	-5.4250283	150.7079295	0.0000	E N	*90*	90
1404	-5.4302508	150.6380281	3.6914	E S	*93.6914*	93.69140749
1405	-5.3761509	150.6782013	7.5947	E	*97.5947*	97.59468671
1406	-5.4052765	150.6569095	10.9541	E	*100.9541*	100.954069
1407	-5.3770883	150.6196154	17.1028	E	*107.1028*	107.1027729
1408	-5.3744770	150.6188789	55.4915	E	*145.4915*	145.4914531
1409	-5.4294474	150.5923645	90.0000	N E	*0*	0
1410	-5.4025313	150.5639085	109.4400	N E	*19.4400*	19.44004871
1411	-5.3873994	150.5680598	113.1986	N E	*23.1986*	23.19859829
1412	-5.3921532	150.5638416	116.5651	N	*26.5651*	26.56508727
1413	-5.3959027	150.5596234	120.9637	N E	*30.9637*	30.96371673
1414	-5.4015270	150.5681937	123.6901	E	*33.6901*	33.69008488
1415	-5.4100973	150.5586191	142.4314	E	*52.4314*	52.43143145
1416	-5.4102312	150.5410098	153.4349	E	*63.4349*	63.43493593
1417	-5.4039374	150.5309665	160.7100	E	*70.7100*	70.70995579
1418	-5.3326969	150.5701354	81.4692	S	*171.4692*	171.469228
1419	-5.3667102	150.6397689	69.4439	s	*159.4439*	159.4439405
1420	-5.3331656	150.5665867	55.4915	s	*145.4915*	145.491477
1421	-5.3275413	150.5702693	75.9638	s	*165.9638*	165.9637565
1422	-5.3232562	150.5660511	108.4350	S	*198.4350*	198.4349669
1423	-5.3247962	150.5558739	358.4518	E	*448.4518*	448.4518455
1424	-5.3131459	150.5729475	0.0000	e	*90.0000*	90
1425	-5.3029687	150.5647120	37.5686	S E	*127.5686*	127.5686081
1426	-5.2996209	150.5676580	25.2011	S E	*115.2011*	115.2011257
1427	-5.2954697	150.5558069	110.0561	S W	*200.0561*	200.0560983
1428	-5.2994870	150.5758266	25.7100	se	*115.7100*	115.7099771
1429	-5.2935280	150.5418133	18.4349	se	*108.4349*	108.4349488
1430	-5.2780167	150.6064252	72.8973	S	*162.8973*	162.8972515
1431	-5.2731066	150.6064252	53.7462	S	*143.7462*	143.7461769
1432	-5.2565910	150.6318682	15.9454	e	*105.9454*	105.9454163
1433	-5.2555197	150.6234765	20.5560	E	*110.5560*	110.556032
1434	-5.2625723	150.6263332	78.6901	S	*168.6901*	168.6900883
1435	-5.2604297	150.6115138	51.5130	nw	*-38.4870*	321.5129517
1466	-5.2279757	150.6874322	0.0000	e	*90.0000*	90
1470	-5.3627435	150.6795583	0.0000	e	*90.0000*	90
1471	-5.3447459	150.7325869	0.0000	e	*90.0000*	90
1601	-5.1293776	150.4442806	0.0000	e	*90.0000*	90
1692	-5.1313777	150.2759946	0.0000	e	*90.0000*	90
1928	-5.4273487	150.5958829	0.0000	e	*90.0000*	90
1941	-5.4048673	150.5497167	2.8624	s	*92.8624*	92.86240523
1489	-5.2403598	150.5408411	2.8624	s	*92.8624*	92.86240739
1461	-5.2328367	150.6897176	3.5763	e	*93.5763*	93.57632876
1851	-5.3016027	150.4464075	3.8141	s	*93.8141*	93.81406845
1467	-5.3017338	150.7296409	4.7636	e	*94.7636*	94.76363173
1850	-5.3009890	150.4142689	5.1944	s	*95.1944*	95.19441707
1458	-5.2092907	150.7101836	5.1944	e	*95.1944*	95.19441707
1841	-5.2601462	150.4140457	6.0090	s	*96.0090*	96.00899409
1791	-5.3365869	150.4691277	6.3402	s	*96.3402*	96.34019703
1910	-5.3175743	150.5633365	6.3402	s	*96.3402*	96.34021815
1700	-5.1756798	150.3035021	7.1250	s	*97.1250*	97.12504966
1923	-5.2277146	150.6913942	7.3860	s	*97.3860*	97.38604724
1936	-5.3861310	150.5358513	8.1301	s	*98.1301*	98.13010235
1538	-5.1118227	150.4266100	8.9726	s	*98.9726*	98.97260467
1492	-5.2000259	150.4985253	9.4623	s	*99.4623*	99.4623027
1632	-5.0459092	150.4026272	9.8658	s	*99.8658*	99.86580098
1865	-5.2574680	150.4130972	10.0080	s	*100.0080*	100.0079798
1594	-5.0396128	150.5821640	10.3048	s	*100.3048*	100.3048349
1560	-4.8874664	150.3188008	10.6196	s	*100.6196*	100.6196267
1483	-5.2160952	150.5474830	11.3099	s	*101.3099*	101.3099325
1438	-5.2626616	150.6199055	11.5346	e	*101.5346*	101.5346258
1940	-5.4024123	150.5380553	11.7683	e	*101.7683*	101.7682615
1759	-5.1558722	150.5013551	11.8887	s	*101.8887*	101.888658
1455	-5.1772861	150.6962569	12.0947	e	*102.0947*	102.094736

Scour unique ID	Latitude	Longitude	Azimuthal orientation (°)	Compass direction	Inferred winds (unformatted)	Azimuthal inferred wind direction (°)
1778	-5.2174399	150.5520537	12.8043	s	*102.8043*	102.8042661
1460	-5.2156515	150.7195574	12.9946	e	*102.9946*	102.9946452
1937	-5.3779847	150.5379716	13.7362	e	*103.7362*	103.7362409
1680	-5.0175313	150.1999668	14.0362	s	*104.0362*	104.0362435
1806	-5.3121482	150.5129834	14.0362	s	*104.0362*	104.0362435
1801	-5.3811792	150.4274145	14.0363	s	*104.0363*	104.0362562
1515	-5.1660364	150.4951612	14.4703	s	*104.4703*	104.4702932
1436	-5.2507882	150.6187450	14.7435	e	*104.7435*	104.7435471
1777	-5.1947643	150.5265214	14.9314	s	*104.9314*	104.9313776
1934	-5.4049398	150.5337924	15.4221	e	*105.4221*	105.4221398
1648	-4.9775701	150.3338150	15.5241	s	*105.5241*	105.5240893
1921	-5.2786844	150.5540576	15.7086	s	*105.7086*	105.7086198
1710	-5.1531159	150.4218457	15.9454	s	*105.9454*	105.9453959
1444	-5.1880064	150.6138684	16.6992	e	*106.6992*	106.6992475
1664	-4.9873545	150.3112109	17.3540	s	*107.3540*	107.3540208
1640	-5.0659422	150.4084300	18.4349	s	*108.4349*	108.4349127
1926	-5.3866635	150.7493127	19.2307	s	*109.2307*	109.2306669
1527	-5.1816147	150.4263757	19.4400	s e	*109.4400*	109.4400487
1636	-5.0570684	150.3983867	19.4401	s	*109.4401*	109.4400582
1781	-5.2254745	150.4948292	19.6538	s	*109.6538*	109.6538437
1939	-5.4065691	150.5386411	19.7989	s	*109.7989*	109.7988984
1787	-5.3459830	150.5824831	20.5560	s	*110.5560*	110.5560452
1633	-5.0643442	150.4351229	20.5561	s	*110.5561*	110.5560526
1437	-5.2473958	150.6187450	20.5561	e	*110.5561*	110.5560541
1493	-5.1688515	150.5676768	20.5561	e s	*110.5561*	110.5560551
1642	-5.0777264	150.4285613	21.0374	s	*111.0374*	111.0374496
1621	-5.0782274	150.4377063	21.0375	s	*111.0375*	111.037511
1439	-5.2104364	150.5756257	21.4130	e	*111.4130*	111.4129801
1960	-5.8296384	150.6982627	21.8014	e	*111.8014*	111.8014199
1869	-5.2479269	150.3926758	21.8014	s	*111.8014*	111.8014214
1947	-5.3144776	150.5610767	22.2490	e	*112.2490*	112.2490237
1755	-5.1984446	150.4648645	22.3801	s	*112.3801*	112.3801351
1742	-5.1810362	150.4201718	22.3802	s	*112.3802*	112.380153
1530	-5.1466193	150.4163770	22.6199	s	*112.6199*	112.6198569
1800	-5.3325696	150.4299588	22.6199	e	*112.6199*	112.6198778
1443	-5.1760102	150.6195596	23.1986	e	*113.1986*	113.1985698
1587	-5.0775207	150.5432451	23.1986	s	*113.1986*	113.1985781
1898	-5.4049398	150.5337924	23.1986	s	*113.1986*	113.1985905
1685	-5.1371805	150.2788960	23.1986	s	*113.1986*	113.1986092
1500	-5.1691729	150.5119699	23.6294	s	*113.6294*	113.6293976
1610	-5.0883831	150.3935910	23.9625	S	*113.9625*	113.9624964
1720	-5.1650562	150.4080640	24.2278	s	*114.2278*	114.2277615
1938	-5.3777058	150.5403429	24.3046	s	*114.3046*	114.3045702
1622	-5.0816366	150.3997258	24.4439	s	*114.4439*	114.4438895
1609	-5.0672252	150.3832798	24.6236	s	*114.6236*	114.6235803
1957	-5.2786844	150.5540576	24.7752	e	*114.7752*	114.7751659
1516	-5.1374688	150.5279246	25.2011	s	*115.2011*	115.2011058
1796	-5.3221245	150.4628339	25.5600	s	*115.5600*	115.5599652
1497	-5.1904379	150.5229506	26.5650	e	*116.5650*	116.5650151
1654	-4.9088293	150.2852322	26.5650	s	*116.5650*	116.5650191
1454	-5.1879989	150.6911683	26.5650	e	*116.5650*	116.5650223
1634	-5.0626034	150.4433807	26.5650	s	*116.5650*	116.5650241
1586	-5.0733360	150.5482109	26.5650	s	*116.5650*	116.5650331
1726	-5.1539528	150.4051068	26.5651	s	*116.5651*	116.5650512
1582	-4.8811607	150.4534356	26.5651	s	*116.5651*	116.5650666
1722	-5.1521673	150.4099053	26.5651	s	*116.5651*	116.5650669
1567	-4.7611887	150.1804041	27.5528	s	*117.5528*	117.5527971
1943	-5.3413992	150.5459225	27.7586	e	*117.7586*	117.7585782
1795	-5.3337078	150.4578792	28.0725	s	*118.0725*	118.0724869
1953	-5.3337830	150.5781225	28.3007	e	*118.3007*	118.3007041
1756	-5.1661945	150.4501343	28.3007	s	*118.3007*	118.3007319
1842	-5.2646657	150.4368663	28.3008	s	*118.3008*	118.3007525
1597	-5.1044702	150.4613765	28.6105	s	*118.6105*	118.6104551
1746	-5.1531940	150.4939343	29.0546	e	*119.0546*	119.0546041
1510	-5.1504581	150.5264070	29.3577	s	*119.3577*	119.3577482
1588	-5.0588290	150.5697706	29.7449	s	*119.7449*	119.7448535
1733	-5.1728677	150.4579458	30.4655	s	*120.4655*	120.4655293
1744	-5.1588852	150.4518082	30.4656	s	*120.4656*	120.4655672
1547	-5.0505027	150.3301162	30.9638	s	*120.9638*	120.9637565
1849	-5.3068476	150.3944055	30.9638	s	*120.9638*	120.9637618
1802	-5.3316322	150.4822509	30.9638	s	*120.9638*	120.9637947

Scour unique ID	Latitude	Longitude	Azimuthal orientation (°)	Compass direction	Inferred winds (unformatted)	Azimuthal inferred wind direction (°)
1697	-5.1546447	150.2240484	31.6075	s	121.6075	121.607493
1537	-5.1407719	150.4353745	32.0054	s	122.0054	122.0053866
1853	-5.2836922	150.4451242	32.4712	s	122.4712	122.4711636
1446	-5.1572627	150.6265899	32.4712	e	122.4712	122.4711796
1482	-5.2239156	150.5857815	32.4712	s e	122.4712	122.4711987
1512	-5.1694734	150.5009640	32.4712	s	122.4712	122.4712135
1935	-5.3811093	150.5324478	33.2317	e	123.2317	123.2317385
1915	-5.3176022	150.5714827	33.6900	s	123.6900	123.6900425
1807	-5.3158977	150.4554688	33.6900	s	123.6900	123.6900467
1590	-5.0239006	150.5834183	33.6901	s	123.6901	123.6900536
1686	-5.1323262	150.2834713	33.6901	s	123.6901	123.6900953
1949	-5.3242698	150.5693346	34.1145	e	124.1145	124.1144729
1799	-5.3047831	150.4590844	34.3803	s	124.3803	124.3803349
1924	-5.8296384	150.6982627	34.5085	s	124.5085	124.508523
1951	-5.3176022	150.5714827	34.6951	e	124.6951	124.6951085
1536	-5.1229350	150.4174305	35.1342	s	125.1342	125.1342129
1644	-5.0406331	150.4023148	35.3112	s	125.3112	125.3112297
1603	-5.1051308	150.4245690	36.0274	s	126.0274	126.0273539
1585	-5.0284089	150.5036856	36.2538	s	126.2538	126.2538409
1602	-5.0974533	150.4325590	36.8699	s	126.8699	126.8698745
1839	-5.3157749	150.4140457	36.8699	s	126.8699	126.8698784
1507	-5.1212656	150.4927508	36.8699	s	126.8699	126.8698832
1477	-5.2209695	150.5412696	36.8699	s	126.8699	126.8698976
1568	-5.4762553	150.5348026	36.8699	s	126.8699	126.8699121
1684	-5.1273046	150.2765526	37.4054	s	127.4054	127.405359
1946	-5.3175743	150.5633365	38.2338	e	128.2338	128.2338252
1757	-5.1929208	150.4251376	38.6598	s	128.6598	128.659803
1734	-5.1767176	150.4752983	38.6598	s	128.6598	128.6598083
1754	-5.1375711	150.4442199	38.6598	s	128.6598	128.6598083
1825	-5.3177166	150.4637154	38.6598	s	128.6598	128.6598149
1687	-5.1655807	150.3031673	38.6598	s	128.6598	128.6598347
1641	-5.0521494	150.3960656	38.9275	s	128.9275	128.9275397
1569	-5.4675064	150.5874741	39.0939	s	129.0939	129.0938691
1573	-4.8882446	150.1489361	39.0939	s	129.0939	129.0938716
1785	-5.2756352	150.5581113	39.2894	s	129.2894	129.2893983
1596	-5.0610653	150.5641664	39.2894	s	129.2894	129.289414
1472	-5.3528341	150.7309264	39.5597	e	129.5597	129.5596576
1766	-5.1637394	150.3984671	39.8056	s	129.8056	129.8055711
1521	-5.1449231	150.5010086	40.1009	s e	130.1009	130.1009163
1566	-4.7714328	150.1935943	40.1009	s	130.1009	130.1009479
1681	-5.0203211	150.2003574	40.2364	s	130.2364	130.2363844
1614	-5.1063766	150.4282399	40.6013	e	130.6013	130.6013031
1945	-5.3161794	150.5545207	40.8554	e	130.8554	130.8553726
1658	-5.0052093	150.2379617	41.1859	s	131.1859	131.1859108
1613	-5.0810492	150.4107672	41.1859	e	131.1859	131.1859316
1699	-5.1465542	150.3035579	41.1860	s	131.1860	131.1859827
1619	-5.0858882	150.4121907	41.6335	s	131.6335	131.6335443
1848	-5.3293892	150.4050068	41.6335	s	131.6335	131.6335443
1679	-4.9550285	150.1909836	41.8202	s	131.8202	131.8201566
1955	-5.3075310	150.5906320	41.8202	e	131.8202	131.8201699
1765	-5.1561512	150.4099611	41.9872	s	131.9872	131.9871646
1481	-5.2186127	150.5436800	41.9872	se	131.9872	131.9872005
1860	-5.2371024	150.4088567	41.9872	s	131.9872	131.9872077
1727	-5.1649446	150.4030982	41.9872	s	131.9872	131.9872125
1511	-5.1599658	150.5281478	41.9872	s	131.9872	131.9872175
1760	-5.1679241	150.4853416	42.1376	s	132.1376	132.1375926
1571	-5.4511158	150.5875634	42.2737	s	132.2737	132.2736931
1790	-5.3413407	150.4694624	42.2737	s	132.2737	132.2737282
1891	-5.4195484	150.6015183	42.5104	s	132.5104	132.5104079
1558	-4.9167929	150.2804354	42.7094	s	132.7094	132.7093796
1650	-4.9290944	150.2775993	42.7094	s	132.7094	132.7093957
1893	-5.4698653	150.5649161	42.7094	s	132.7094	132.7094232
1553	-5.0371786	150.3503367	42.7094	s	132.7094	132.7094246
1528	-5.1508599	150.4327141	43.0251	s e	133.0251	133.0250703
1811	-5.3509153	150.4446220	43.0251	s	133.0251	133.0250763
1749	-5.1863369	150.4384729	43.0251	s	133.0251	133.0250948
1661	-5.0201626	150.3068811	43.3634	s	133.3634	133.3634159
1959	-5.2277146	150.6913942	43.3635	e	133.3635	133.363471
1563	-4.7885064	150.2452168	43.7270	s	133.7270	133.7269646
1942	-5.3203362	150.5374136	44.1449	e	134.1449	134.1448764
1814	-5.3034440	150.4555357	45.0000	s	135.0000	134.9999549

Scour unique ID	Latitude	Longitude	Azimuthal orientation (°)	Compass direction	Inferred winds (unformatted)	Azimuthal inferred wind direction (°)
1476	-5.1791787	150.6845933	45.0000	s	135.0000	134.9999662
1719	-5.1688504	150.4062785	45.0000	s	135.0000	134.9999691
1838	-5.1812728	150.6970214	45.0000	s	135.0000	134.9999788
1450	-5.1534128	150.6216798	45.0000	e se	135.0000	135
1671	-5.0505027	150.3301162	45.0000	s	135.0000	135
1764	-5.1609496	150.4341766	45.0000	s	135.0000	135
1782	-5.2302060	150.5520537	45.0000	s	135.0000	135
1828	-5.3917358	150.4843042	45.0000	s	135.0000	135
1456	-5.1682471	150.6933778	45.0000	e	135.0000	135
1631	-4.9266840	150.4211069	45.0000	s	135.0000	135
1803	-5.3615612	150.4997263	45.0000	s	135.0000	135
1831	-5.3945256	150.5156616	45.0000	s	135.0000	135
1718	-5.1699105	150.4091241	45.0000	s	135.0000	135.0000394
1958	-5.2931914	150.5564289	46.0051	e	136.0051	136.005086
1695	-5.1290342	150.2692433	46.4688	s	136.4688	136.4687794
1703	-5.1806122	150.3155094	46.8476	s	136.8476	136.8475833
1918	-5.3114367	150.5805775	46.9749	s	136.9749	136.9749052
1705	-5.1951750	150.3223165	47.2906	s	137.2906	137.2906204
1552	-4.9733702	150.3279737	47.2906	s	137.2906	137.2906204
1877	-5.2122932	150.4023687	47.4895	s	137.4895	137.489517
1498	-5.1482828	150.5734081	47.4896	s	137.4896	137.4895502
1784	-5.3064347	150.5310614	47.4896	s	137.4896	137.4895529
1870	-5.2304738	150.4380939	47.4896	e	137.4896	137.4895562
1551	-4.9800657	150.3315892	47.7263	s	137.7263	137.7263208
1912	-5.3097628	150.5638108	47.7263	s	137.7263	137.7263257
1738	-5.1955990	150.4581131	48.0128	s	138.0128	138.0127779
1599	-5.1171471	150.4488336	48.0128	s	138.0128	138.0127835
1786	-5.2485853	150.5532013	48.0128	s	138.0128	138.0127875
1797	-5.3219237	150.4563392	48.0128	s	138.0128	138.0127899
1917	-5.3337830	150.5781225	48.0128	s	138.0128	138.0128354
1562	-4.8515114	150.3747754	48.1798	s	138.1798	138.1798434
1859	-5.2398364	150.4052857	48.5763	s	138.5763	138.5763377
1884	-5.3839779	150.6212272	48.8140	s	138.8140	138.814048
1663	-5.0427935	150.3268338	48.8141	s	138.8141	138.8140557
1952	-5.3471741	150.5834231	48.8141	e	138.8141	138.8140748
1783	-5.2598449	150.5874061	48.8141	s	138.8141	138.8140787
1581	-4.8782147	150.4549756	48.8141	s	138.8141	138.8140892
1815	-5.3898610	150.4270574	48.8141	s	138.8141	138.8140892
1589	-5.0562066	150.6019426	48.8141	s	138.8141	138.8141132
1872	-5.2301926	150.4206252	48.8141	s	138.8141	138.8141362
1751	-5.1811478	150.4087336	49.0856	s	139.0856	139.0856168
1524	-5.1854088	150.4450786	49.0856	s e	139.0856	139.085642
1752	-5.1592200	150.4967241	49.3987	s	139.3987	139.3987054
1776	-5.2022633	150.5219685	49.3987	s	139.3987	139.3987054
1649	-4.9902023	150.3312707	49.3987	s	139.3987	139.3987245
1724	-5.1531717	150.3898745	49.6354	s	139.6354	139.6354421
1706	-5.1374818	150.2934141	49.9698	s	139.9698	139.969761
1531	-5.1584035	150.4045036	50.1944	e	140.1944	140.194419
1871	-5.1889615	150.4382055	50.1944	s	140.1944	140.194436
1792	-5.3778983	150.4794388	50.1945	s	140.1945	140.1944715
1748	-5.1873412	150.4982306	50.5275	s	140.5275	140.5275455
1907	-5.3413992	150.5459225	50.5275	s	140.5275	140.5275455
1829	-5.3941908	150.5128160	50.7106	s	140.7106	140.7105905
1914	-5.3129711	150.5633644	50.7106	s	140.7106	140.7106146
1899	-5.3811093	150.5324478	50.7106	e	140.7106	140.7106403
1883	-5.3660673	150.4932643	50.7106	s	140.7106	140.7106403
1832	-5.4092558	150.5552769	50.8263	s	140.8263	140.8263432
1522	-5.2014335	150.4394989	51.0090	s	141.0090	141.0090171
1830	-5.3464851	150.4679559	51.3402	s	141.3402	141.3401785
1496	-5.1622095	150.5675696	51.3402	e	141.3402	141.3401829
1520	-5.1168465	150.5556888	51.3402	s e	141.3402	141.3401954
1570	-5.4903605	150.5873848	51.3402	s	141.3402	141.340197
1655	-4.9620811	150.3161209	51.3402	s	141.3402	141.3402035
1677	-4.8936192	150.1518147	51.3402	s	141.3402	141.3402182
1819	-5.3344555	150.4863687	51.3402	s	141.3402	141.3402182
1834	-5.2131882	150.5353242	51.3402	s	141.3402	141.3402182
1583	-4.9935922	150.4694268	51.3402	s	141.3402	141.3402182
1708	-5.1326387	150.2647907	51.3402	s	141.3402	141.3402182
1844	-5.3189553	150.4493089	51.6325	s	141.6325	141.6325177
1736	-5.1312438	150.4874061	51.6325	s	141.6325	141.6325192
1639	-5.0712808	150.3995027	51.7098	s	141.7098	141.7098313

Scour unique ID	Latitude	Longitude	Azimuthal orientation (°)	Compass direction	Inferred winds (unformatted)	Azimuthal inferred wind direction (°)
1780	-5.1718209	150.5082203	51.8427	s	141.8427	141.8427434
1779	-5.1568229	150.5308066	51.8428	s	141.8428	141.8427734
1623	-5.0720843	150.3966459	52.1250	s	142.1250	142.1249697
1880	-5.3881068	150.4220573	52.1250	s	142.1250	142.125023
1774	-5.1851852	150.5096799	52.1250	s	142.1250	142.1250297
1488	-5.2433058	150.5492507	52.4314	s w	142.4314	142.431408
1517	-5.1452802	150.5763557	52.5946	s	142.5946	142.5946276
1665	-5.0221713	150.3170137	52.5946	s	142.5946	142.594641
1721	-5.1545108	150.4145364	52.5947	s	142.5947	142.5946509
1798	-5.3296235	150.4554688	52.7093	s	142.7093	142.7093499
1696	-5.1398029	150.2898320	53.1301	s	143.1301	143.1300879
1576	-4.8877759	150.3057857	53.1301	s	143.1301	143.1301024
1672	-4.9125341	150.1463467	53.1301	s	143.1301	143.1301024
1840	-5.2667859	150.4033329	53.1301	s	143.1301	143.1301081
1769	-5.1964449	150.5725510	53.1301	s	143.1301	143.130111
1810	-5.3780992	150.4215894	53.1301	s	143.1301	143.1301216
1678	-4.9263493	150.1471837	53.1302	s	143.1302	143.130189
1897	-5.4443319	150.5872451	53.4711	s	143.4711	143.4711293
1747	-5.1536961	150.4412069	53.9726	s	143.9726	143.9726407
1526	-5.1773295	150.4512384	54.1623	s e	144.1623	144.1623287
1845	-5.3206292	150.4468539	54.1624	s	144.1624	144.1623514
1612	-5.0918201	150.3993491	54.4623	e	144.4623	144.4623027
1478	-5.2231657	150.5353775	54.4623	s	144.4623	144.4623149
1956	-5.2715704	150.5607252	54.4623	e	144.4623	144.4623158
1758	-5.2001743	150.4939343	54.4623	s	144.4623	144.4623222
1804	-5.3206515	150.4248702	54.4623	s	144.4623	144.4623405
1864	-5.2593651	150.4076850	54.6888	s	144.6888	144.6887936
1659	-5.0313218	150.3228611	54.7824	s	144.7824	144.782372
1740	-5.1944273	150.4438851	54.7824	s	144.7824	144.782441
1501	-5.1752256	150.5023284	55.0079	s	145.0079	145.0079391
1909	-5.3161794	150.5545207	55.3048	s	145.3048	145.3048421
1903	-5.4065691	150.5386411	55.3049	s	145.3049	145.3048603
1540	-5.0740710	150.4077844	55.9228	s	145.9228	145.9228117
1789	-5.3225040	150.5281153	56.3099	s	146.3099	146.3098992
1913	-5.3242698	150.5693346	56.3099	s	146.3099	146.3098992
1611	-5.0720013	150.3934570	56.3099	n	-33.6901	326.309914
1653	-4.9153463	150.2803668	56.3099	s	146.3099	146.3099151
1533	-5.1461283	150.4075836	56.3099	s	146.3099	146.3099325
1694	-5.1531940	150.3090817	56.3099	s	146.3099	146.3099325
1725	-5.1376603	150.4221804	56.3099	s	146.3099	146.3099436
1673	-4.9154913	150.1443939	56.8215	s	146.8215	146.8214906
1728	-5.1736488	150.4402026	57.0947	s	147.0947	147.0947338
1743	-5.1977193	150.4432156	57.2648	s	147.2648	147.2647696
1628	-5.0096730	150.4208391	57.2648	s	147.2648	147.2647737
1674	-4.9137616	150.1439475	57.3808	s	147.3808	147.3807618
1794	-5.3271462	150.4614278	57.5288	s	147.5288	147.528772
1889	-5.2952695	150.7344431	57.5288	s	147.5288	147.5288077
1944	-5.3410086	150.5479591	58.2405	e	148.2405	148.240483
1723	-5.1198056	150.4019822	58.2405	s	148.2405	148.2405015
1474	-5.2205839	150.7163034	58.3925	e	148.3925	148.3924768
1651	-4.9100345	150.2813488	58.3925	s	148.3925	148.3924784
1868	-5.2455834	150.3974743	58.5704	s	148.5704	148.570413
1888	-5.2018891	150.7189596	58.5704	s	148.5704	148.570413
1704	-5.1538858	150.2984916	58.5704	s	148.5704	148.5704149
1793	-5.3308957	150.4630347	58.5704	s	148.5704	148.570448
1508	-5.1449231	150.5222111	58.5705	s	148.5705	148.5704648
1556	-4.9828620	150.3212661	58.7816	s	148.7816	148.7816154
1577	-4.8890481	150.3104056	59.0362	s	149.0362	149.0362244
1775	-5.2118156	150.5400910	59.0362	s	149.0362	149.0362435
1863	-5.2599230	150.4228057	59.0362	e	149.0362	149.0362435
1627	-5.0030667	150.4159737	59.0363	s	149.0363	149.0362562
1857	-5.2417335	150.4005431	59.0363	s	149.0363	149.0362562
1753	-5.1817058	150.4934321	59.5344	s	149.5344	149.5344328
1905	-5.4048673	150.5497167	59.5344	s	149.5344	149.5344328
1894	-5.4660879	150.5987481	59.7435	s	149.7435	149.7435314
1656	-4.9670001	150.3260750	60.0184	s	150.0184	150.0183879
1846	-5.3109765	150.4493647	60.2551	s	150.2551	150.2550854
1578	-4.8712379	150.3181055	60.2551	s	150.2551	150.2550921
1580	-4.8660556	150.4360540	60.2551	s	150.2551	150.255102
1835	-5.2265235	150.5441400	60.2552	s	150.2552	150.255152
1717	-5.1421240	150.4055532	60.6422	s	150.6422	150.6422233

Scour unique ID	Latitude	Longitude	Azimuthal orientation (°)	Compass direction	Inferred winds (unformatted)	Azimuthal inferred wind direction (°)
1534	-5.1587159	150.4145469	60.6423	s	150.6423	150.6422518
1875	-5.2491633	150.4057611	60.6423	s	150.6423	150.6422876
1881	-5.4124339	150.5522966	60.9454	s	150.9454	150.9453755
1816	-5.3705779	150.5177596	60.9454	s	150.9454	150.9453857
1961	-5.5018518	150.5408127	60.9454	e	150.9454	150.9453857
1662	-4.9953891	150.3020157	61.5571	s	151.5571	151.5570815
1823	-5.3273694	150.4836347	61.6993	s	151.6993	151.6992691
1600	-5.1212983	150.4507976	61.6993	s	151.6993	151.6992707
1643	-5.0461234	150.3305833	61.9275	s	151.9275	151.9275056
1900	-5.3861310	150.5358513	62.1027	s	152.1027	152.1027079
1763	-5.1406956	150.4415975	62.1027	s	152.1027	152.1027079
1852	-5.2964695	150.4443430	62.1027	s	152.1027	152.1027153
1729	-5.1490427	150.4596754	62.2415	s	152.2415	152.2414763
1519	-5.1131417	150.4900725	63.4349	s e	153.4349	153.4349488
1645	-5.0340715	150.3897718	63.4349	s	153.4349	153.4349488
1670	-5.0968845	150.2618871	63.4349	s	153.4349	153.4349488
1773	-5.2304582	150.5437156	63.4350	s	153.4350	153.4349597
1858	-5.2353169	150.3971953	63.4350	s	153.4350	153.4349612
1595	-5.0612617	150.6051966	63.4350	s	153.4350	153.4349649
1545	-5.0229171	150.3457391	63.4350	s	153.4350	153.4349685
1762	-5.1997893	150.4702767	63.4350	s	153.4350	153.4349736
1666	-5.0471590	150.3069704	63.4350	s	153.4350	153.4349921
1657	-4.9654824	150.3236646	64.1790	s	154.1790	154.1789861
1862	-5.2684040	150.4411069	64.4401	s	154.4401	154.4400508
1574	-4.8626007	150.1476640	64.6538	s	154.6538	154.6538064
1906	-5.3203362	150.5374136	64.7989	s	154.7989	154.7988567
1873	-5.2286750	150.4012974	64.8852	s	154.8852	154.8851547
1637	-5.0998038	150.3948158	64.9831	s	154.9831	154.9830552
1532	-5.1636260	150.4263757	64.9831	s	154.9831	154.9830802
1902	-5.3777058	150.5403429	64.9831	s	154.9831	154.9830844
1772	-5.1917134	150.5462152	64.9831	s	154.9831	154.9830955
1878	-5.1944831	150.4375426	65.2248	s	155.2248	155.2248468
1904	-5.4024123	150.5380553	65.2249	e	155.2249	155.224889
1950	-5.3129711	150.5633644	65.4328	e	155.4328	155.4328287
1503	-5.1308744	150.5479651	65.5560	s	155.5560	155.5560421
1559	-4.8925550	150.3254293	65.6954	s	155.6954	155.6954461
1480	-5.2314681	150.5593743	65.7723	s e	155.7723	155.7722536
1901	-5.3779847	150.5379716	65.7723	e	155.7723	155.7722547
1572	-4.7775808	150.1943988	65.7723	s	155.7723	155.7722678
1523	-5.1769278	150.4266882	65.7723	s e	155.7723	155.7722678
1919	-5.3075310	150.5906320	66.0375	s	156.0375	156.0374932
1854	-5.2787821	150.4455705	66.0375	s	156.0375	156.0375222
1564	-4.7931933	150.2468907	66.0375	s	156.0375	156.0375222
1837	-5.2513527	150.6451421	66.0375	s	156.0375	156.0375222
1683	-5.1349486	150.2707498	66.2505	s	156.2505	156.2504823
1487	-5.1957408	150.4714218	66.3706	s e	156.3706	156.3706024
1892	-5.4273487	150.5958829	66.3706	s	156.3706	156.3706024
1843	-5.2591419	150.4384844	66.3706	s	156.3706	156.3706069
1635	-5.0764855	150.3921822	66.3706	s	156.3706	156.3706365
1805	-5.2934677	150.4520541	66.8014	s	156.8014	156.8013908
1768	-5.2018013	150.4882765	66.8014	s	156.8014	156.8014005
1676	-4.9498617	150.1862968	66.8014	s	156.8014	156.8014033
1833	-5.3269007	150.4866476	66.8014	s	156.8014	156.8014033
1948	-5.3097628	150.5638108	66.8014	e	156.8014	156.8014095
1820	-5.3018148	150.5712904	66.8014	s	156.8014	156.8014235
1711	-5.1749321	150.4113002	67.3801	s	157.3801	157.3801094
1565	-4.7749815	150.1904474	67.5206	s	157.5206	157.5205689
1646	-5.0110031	150.3578743	67.8906	s	157.8906	157.8905562
1702	-5.3068453	150.3742627	68.1986	s	158.1986	158.1985532
1826	-5.3321678	150.5135414	68.1986	s	158.1986	158.1985905
1767	-5.1481723	150.4625768	68.6294	s	158.6294	158.6293777
1630	-4.9155694	150.4245440	68.7495	s	158.7495	158.7494945
1788	-5.3807997	150.5455237	68.9625	s	158.9625	158.9624666
1691	-5.1353392	150.2755482	68.9625	s	158.9625	158.9624778
1911	-5.3144776	150.5610767	69.1455	s	159.1455	159.1455462
1836	-5.2062137	150.5411270	69.2277	s	159.2277	159.2277348
1513	-5.1334068	150.5021691	69.4439	e	159.4439	159.4439259
1809	-5.2884460	150.5559688	69.7751	s	159.7751	159.7751326
1896	-5.4691723	150.5527587	69.7751	s	159.7751	159.7751406
1808	-5.3842591	150.4927629	69.7752	s	159.7752	159.7751577
1712	-5.1634381	150.4287644	70.0169	s	160.0169	160.0168808

Scour unique ID	Latitude	Longitude	Azimuthal orientation (°)	Compass direction	Inferred winds (unformatted)	Azimuthal inferred wind direction (°)
1629	-4.9255235	150.4191429	70.0169	s	160.0169	160.0168935
1592	-5.0670756	150.5969209	70.2844	s	160.2844	160.2843779
1693	-5.1404725	150.2936820	70.7099	s	160.7099	160.7099345
1739	-5.1977751	150.4306057	71.5650	s	161.5650	161.5650295
1707	-5.1234323	150.2703146	71.5651	e	161.5651	161.5650512
1668	-5.0912603	150.2709484	71.5651	s	161.5651	161.5650512
1882	-5.3880510	150.5572625	71.5651	s	161.5651	161.5650512
1473	-5.3771523	150.7059119	71.5651	e	161.5651	161.5650728
1575	-4.8773978	150.1494048	72.2553	s	162.2553	162.2553183
1771	-5.2100145	150.5004178	72.2553	s	162.2553	162.2553284
1689	-5.1557048	150.2817416	72.3499	s	162.3499	162.3498941
1660	-5.0272153	150.3203614	72.4745	s	162.4745	162.4744698
1652	-4.9273536	150.2702342	72.6460	s	162.6460	162.6459561
1479	-5.2353248	150.5588387	72.8972	s	162.8972	162.8972388
1682	-5.1264676	150.2571913	73.3007	s	163.3007	163.3007309
1669	-5.0980004	150.2713948	73.4956	s	163.4956	163.4956468
1861	-5.2888812	150.4544421	74.0546	s	164.0546	164.0545878
1813	-5.3463847	150.4446443	74.0546	s	164.0546	164.0546041
1561	-4.8885377	150.3149843	74.3578	s	164.3578	164.3577664
1548	-5.0080084	150.3119936	74.3578	s	164.3578	164.3577664
1579	-4.8700729	150.4339115	74.7449	s	164.7449	164.7448713
1543	-5.0402585	150.4061105	74.7449	s	164.7449	164.7448757
1812	-5.2883790	150.4412742	75.0686	s	165.0686	165.0685963
1688	-5.1570439	150.2993732	75.2032	s	165.2032	165.2032345
1916	-5.3471741	150.5834231	75.2564	s	165.2564	165.2564259
1770	-5.2010871	150.5755863	75.2564	s	165.2564	165.2564259
1866	-5.2459740	150.4384286	75.3791	s	165.3791	165.3791168
1514	-5.1436733	150.5598400	75.9637	e	165.9637	165.96373
1625	-5.0590860	150.4441396	75.9637	s	165.9637	165.9637311
1922	-5.2931914	150.5564289	75.9637	s	165.9637	165.9637395
1895	-5.4736137	150.5911151	75.9637	s	165.9637	165.9637438
1584	-4.9910255	150.4716587	75.9638	s	165.9638	165.9637565
1855	-5.2579144	150.4166124	75.9638	s	165.9638	165.9637565
1690	-5.1645206	150.2982015	76.4295	s	166.4295	166.4295498
1741	-5.1860021	150.4289318	77.0054	s	167.0054	167.0053759
1709	-5.1176295	150.4256398	77.0054	s	167.0054	167.0053832
1616	-5.1025199	150.4147953	77.4711	s	167.4711	167.4711328
1817	-5.3416532	150.5407699	77.4712	s	167.4712	167.4711987
1618	-5.0781884	150.4322103	77.4712	s	167.4712	167.4712263
1557	-4.9340674	150.3330623	77.9053	s	167.9053	167.9052693
1529	-5.1702323	150.4144576	78.6901	s	168.6901	168.6900536
1491	-5.2224158	150.5484472	79.9920	s	169.9920	169.9919936
1518	-5.1631796	150.5252464	80.1342	s	170.1342	170.1341748
1554	-4.9814048	150.3074853	80.2724	s	170.2724	170.2724103
1505	-5.1029139	150.5506969	80.2724	s e	170.2724	170.2724386
1874	-5.2247916	150.4024134	80.3401	s	170.3401	170.3401039
1715	-5.1440769	150.4363527	80.5377	s	170.5377	170.5376661
1908	-5.3410086	150.5479591	80.8698	s	170.8698	170.8698218
1494	-5.1561568	150.5664448	81.0274	s	171.0274	171.0273909
1541	-5.0705000	150.4033207	81.2539	s	171.2539	171.2538534
1598	-5.1250032	150.4479855	81.2539	s	171.2539	171.2538544
1593	-5.0692071	150.5861635	81.4693	s	171.4693	171.4692503
1620	-5.0843817	150.4345873	81.8699	s	171.8699	171.8699121
1525	-5.1920597	150.4307947	81.8699	s e	171.8699	171.8699157
1886	-5.0792567	150.6240058	82.0928	s	172.0928	172.092834
1818	-5.3246912	150.5213528	82.2348	s	172.2348	172.2348252
1745	-5.1511295	150.4494089	82.8750	s	172.8750	172.8749837
1954	-5.3114367	150.5805775	83.2110	e	173.2110	173.2110206
1847	-5.3057874	150.4483046	83.2901	s	173.2901	173.2901312
1732	-5.1451370	150.4129183	83.4181	s	173.4181	173.4180844
1495	-5.1510682	150.5615169	84.5597	s	174.5597	174.5596777
1550	-4.9881896	150.3375259	84.6441	s	174.6441	174.6441498
1624	-5.0559614	150.4056626	84.8056	s	174.8056	174.8055711
1675	-4.8991989	150.1214059	85.0302	s	175.0302	175.0302349
1441	-5.1890107	150.6088356	85.2364	s	175.2364	175.2363683
1591	-5.0479376	150.6094751	85.6012	s	175.6012	175.6012479
1535	-5.1162930	150.4224655	85.6013	s	175.6013	175.6013026
1502	-5.1818141	150.5147553	85.9143	s	175.9143	175.9143283
1638	-5.0768158	150.3798624	86.0548	e	176.0548	176.0547984
1504	-5.1316779	150.5541250	87.3974	e	177.3974	177.3974415
1486	-5.2149703	150.5264323	87.7094	s	177.7094	177.7093886

113

Scour unique ID	Latitude	Longitude	Azimuthal orientation (°)	Compass direction	Inferred winds (unformatted)	Azimuthal inferred wind direction (°)
1647	-5.0004242	150.3516698	87.7094	s	177.7094	177.7094228
1713	-5.1509398	150.4246355	90.0000	s	180.0000	180
1714	-5.1450812	150.4299361	90.0000	s	180.0000	180
1716	-5.1410639	150.4075061	90.0000	s	180.0000	180
1925	-5.5018518	150.5408127	90.0000	s	180.0000	180
1606	-5.0948643	150.4367995	94.3987	s	184.3987	184.3986799
1475	-5.2070857	150.7201600	94.9698	s	184.9698	184.9697631
1555	-4.9919168	150.3431725	95.9061	s	185.9061	185.9061309
1735	-5.1708590	150.4953850	98.1301	s	188.1301	188.1301081
1485	-5.1878668	150.5139518	99.4623	s	189.4623	189.4623222
1499	-5.1442655	150.5648379	99.4623	s	189.4623	189.4623339
1879	-5.1922959	150.4660656	102.1714	s	192.1714	192.171449
1546	-5.0444321	150.3295806	103.5704	s	193.5704	193.5704149
1539	-5.1096466	150.4173479	104.6209	s	194.6209	194.620882
1490	-5.2118100	150.5193082	105.0685	s	195.0685	195.0684965
1667	-5.0439452	150.3147372	105.6422	s	195.6422	195.6422336
1626	-5.0525244	150.4204374	106.3895	s	196.3895	196.3895072
1544	-5.0176500	150.3474353	107.2415	s	197.2415	197.2414547
1701	-5.2056646	150.2502726	107.5256	s	197.5256	197.525582
1506	-5.0955756	150.5476973	109.1790	s	199.1790	199.1790065
1927	-5.4195484	150.6015183	109.1790	s	199.1790	199.1790197
1549	-4.9897073	150.3340443	111.4477	s	201.4477	201.4477483
1542	-5.0930417	150.4132524	113.6294	s	203.6294	203.6293836
1484	-5.2017400	150.5300211	121.6075	s	211.6075	211.607532
1932	-5.4691723	150.5527587	140.7106	e	50.7106	50.71061815
1929	-5.4698653	150.5649161	141.8428	e	51.8428	51.84277341
1930	-5.4660879	150.5987481	142.4314	e	52.4314	52.43139187
1604	-5.0997298	150.4341213	151.6992	e	61.6992	61.69923678
1931	-5.4736137	150.5911151	160.1046	e	70.1046	70.10457153
1607	-5.0859370	150.4064464	160.5600	e	70.5600	70.55997017
1856	-5.2514420	150.3952982	161.5651	e	71.5651	71.56506471
1453	-5.1694523	150.6845397	161.5651	e	71.5651	71.56508727
1887	-5.2107607	150.7252925	167.4712	e	77.4712	77.4711821
1442	-5.1855290	150.6218695	168.1113	e	78.1113	78.11134675
1737	-5.1827101	150.4977842	175.7108	e	85.7108	85.71084506
1615	-5.0795409	150.4070820	198.4350	s	108.4350	108.4349633
1761	-5.1959896	150.4539284	211.5043	s	121.5043	121.5042589
1750	-5.1816500	150.4307172	255.2564	s	165.2564	165.2564259
1447	-5.1510135	150.6293239	319.7636	ne	49.7636	49.76363173
1933	-5.4443319	150.5872451	334.6326	e	64.6326	64.63258542
1890	-5.3866635	150.7493127	336.5713	e	66.5713	66.57132097
1459	-5.2123707	150.7309398	342.8973	e	72.8973	72.89725152
1920	-5.2715704	150.5607252	344.7449	e	74.7449	74.7448813
1608	-5.0875350	150.3913145	345.9638	e	75.9638	75.96375653
1451	-5.1808645	150.6213451	345.9638	e ne	75.9638	75.96378484
1885	-5.3766686	150.6647481	347.1250	e	77.1250	77.12499306
1464	-5.2375794	150.6858119	347.9053	e	77.9053	77.90526405
1457	-5.1763487	150.6797190	350.5377	e	80.5377	80.5376973
1876	-5.2168462	150.4092428	351.5730	e	81.5730	81.57302633
1445	-5.1621728	150.6289891	352.4054	e	82.4054	82.40536924
1462	-5.2696621	150.6716955	352.8750	e	82.8750	82.87499476
1440	-5.1728522	150.6051753	353.2902	e	83.2902	83.29017305
1465	-5.2483837	150.6822900	355.2364	e and w	85.2364	85.23636827
1468	-5.3280338	150.7036622	355.6013	e	85.6013	85.60130314
1452	-5.1457687	150.6309978	355.9144	e	85.9144	85.91439055
1509	-5.1584928	150.5205595	356.1859	e	86.1859	86.18593315

VITA

Ariana Sterling Boyd was born in Boston on August 23, 1992, to parents Jon ("Wes") and Theonia Boyd, the second of four children (Naomi, Anaïs, and Emerson). She grew up in Northampton, Massachusetts, moving to Needham, Mass., at 11. She was fortunate to also grow up with her late grandmother Frida H. Boyd, who she considers her third parent.

Ariana earned her high school diploma, *cum laude*, from St. Paul's School (SPS) in Concord, New Hampshire. She earned a B.A. with honors in Geology (and a minor in Religious Studies—a nod to her interest in the history of religion) from Colby College in Waterville, Maine, in May 2014. She served as a research assistant to Walter "Bill" Sullivan, a structural geologist, for her junior and senior years at Colby, eventually applying to graduate school for geology. At the University of Tennessee, Ariana's research took an interplanetary turn when she began her thesis research in Martian aeolian geomorphology. She considers this thesis, her first planetary science work, a testament to what she has learned about Mars, academia, and herself.

Ariana has missed her fellow Earthlings. She looks forward to attending Vanderbilt Law School as a member of the J.D. Class of 2021.